



SESAME

Research and Innovation Action (RIA)

This project has received funding from the Euratom research and training programme 2014-2018 under grant agreement No 654935.

Start date : 2015-04-01 Duration : 48 Months
<http://sesame-h2020.eu/>



CIRCLE experiment: CFD model validation

Authors : Mr. Vincent MOREAU (CRS4), K. Zwijssen NRG, S. Lampis CRS4

SESAME - Contract Number: 654935

thermal hydraulics Simulations and Experiments for the Safety Assessment of Metal cooled reactors

Document title	CIRCLE experiment: CFD model validation
Number of pages	70
Author(s)	Mr. Vincent MOREAU, K. Zwijsen NRG, S. Lampis CRS4
Document type	Deliverable
Work Package	WP3
Issued by	CRS4
Document number	D3.4
Date of completion	2018-08-10 11:35:47
Dissemination level	Public

Summary

This document describes the post-test CFD modeling of the CIRCE experimental pool-type loop working with LBE, in configuration ICE and a combined analysis of the numerical results and the experimental results from the ENEA data-base. This document comes as a complement to the deliverable D3.2 "CIRCE experiments: pre-test, data-set and analysis" by ENEA with pre-test contributions from CRS4 and NRG. The initial discrepancies between the numerical and experimental results are analyzed and corrective actions are taken to improve the numerical modeling. Additional information is also extracted from the database, allowing a better understanding of the CIRCE behavior. The upgraded models are then operated and show a better agreement with the experiment.

Approval

Date	By
2018-08-10 11:44:31	Mr. Vincent MOREAU (CRS4)
2018-08-10 22:58:00	Dr. Mariano TARANTINO (ENEA)

Table of contents

1	General introduction	3
2	NRG part, summary	4
3	Introduction	5
4	Initial Model Description	6
4.1	Full test-facility geometry	6
4.2	Fuel Pin Simulator	7
4.2.1	FPS Geometry	8
4.2.2	Porous Medium Approach	8
4.2.3	Heat Source Model	10
4.3	Argon Injection	10
4.4	Cover Gas & Free Surface	10
4.5	Heat Exchanger	11
4.5.1	HX Geometry	11
4.5.2	Porous Medium Model for the HX	11
4.5.3	Heat Sink Model	12
4.6	Decay Heat Removal System	12
4.7	Conjugate Heat Transfer	13
5	Model Modifications	15
6	Mesh Generation	17
7	Numerical Settings	19
7.1	Simulation Settings	19
7.2	Material Properties	19
8	Description of SESAME WP3 Test 2	21
9	Results	22
9.1	Steady State Results	22
9.2	Transient Results	25
10	Conclusions of NRG part	29
11	Introduction of CRS4 part	30
12	The experimental deviation from steady-state	32
13	Multi-scale analysis of the ICE heat exchanger	35
13.1	Geometry	35
13.2	Setting and instrumentation	36
13.3	Results and analysis	37
14	More on the FPS heat balance	43

15	Flow conveyor and riser.....	47
16	Updated numerical model.....	50
1.4	Main changes	50
1.5	FPS heat source radial restriction	50
1.6	Conveyor/Riser thermal resistance	51
1.7	Gas separator bypass	52
1.8	SGE cooling parameter change	52
1.9	Pulsed body force	53
1.10	Main result, discussion	54
17	Steady-State model	58
18	Conclusion	63
19	Acronyms and definitions.....	64
20	Annexes	65
1.11	Annex 1 – Mass transfer.....	65
1.12	Annex 2: SG 2-region model.....	66
1.12.1	Shape, size and porosity	66
1.12.2	Hydraulic resistance	67
1.12.3	Bottom grid	67
21	General conclusion	69
22	References.....	70

1 General introduction

In the SESAME deliverable D3.2 "CIRCE experiments: pre-Test, data-set and analysis" by ENEA with contributions from CRS4 and NRG for the pre-test part, it could be observed that a quite large discrepancy existed between the experimental and the numerical results. The work presented here is an attempt to understand and when possible correct this discrepancy. It has been performed in parallel and in collaboration between CRS4 and NRG with support from ENEA whose data-base results has been extensively exploited. The two institutions have mainly worked in complementary direction. From one side, NRG has refined its numerical model to better capture the transient phenomena. Therefore, the effort has been put on the improvement of the hydraulic resistances and on a better representation of the DHR behavior. Instead CRS4 has focused its analysis on the steady-state configuration, investigating on the HX thermal representation and exploiting the data-base to aggregate relevant data and improve the understanding of the CIRCE experimental behavior.

Improved CFD models have been built and operated. Results and confront with former numerical and experimental data are presented, starting from the work performed by NRG, followed by the work performed by CRS4.

2 NRG part, summary

The aim of this report is to update on the work done on modelling CIRCE-ICE since the last deliverable, D3.2. In this report, results of an additional test (transient test 2) simulated using the initial model, presented in that deliverable, are shown. Based on those results, the model has been modified. Results using the improved model for the same test are also shown. Overall, an improvement in results is observed when compared with the experiment.

3 Introduction

As part of Work Package 3 (WP3) of the Horizon 2020 project called SESAME [1], short for thermal hydraulics Simulations and Experiments for the Safety Assessment of MEtal cooled reactors, NRG is, among others, responsible for making a CFD thermal-hydraulics model of the CIRCE test facility in its Integral Circulation Experiments (ICE, [2], [3]) configuration. CIRCE (CIRColazione Eutettico, [4], [5]) is a heavy liquid-metal pool-type facility used to mimic accident scenarios possibly occurring inside a nuclear reactor and is operated by ENEA, the Italian National Agency for New Technologies, Energy and Sustainable Economic Development.

ENEA performed several accident scenario experiments with CIRCE-ICE as part of SESAME WP3. Some of these experiments are to be modelled by NRG using the CFD code ANSYS Fluent [6]. A previous report [7] gives a detailed description of CIRCE-ICE and the meshing and modelling strategy used by NRG to come to a numerical model of CIRCE-ICE, referred to from now on by “initial model”. That report also contains some results obtained with the initial model, most noteworthy simulation results of the Protected Loss Of Heat sink and Loss Of Flow (PLOH + LOF) transient test 1.

Following that report, an additional transient test, test 2, has also been simulated using the initial model. Transient test 2 is very similar to transient test 1, though it's quite a bit shorter, ~20hrs for test 1 and ~6hrs for test 2, and the nominal power is 600kW in test 2 compared to 800kW for test 1. A comparison of the simulation results with the experiments showed some shortcomings of the initial numerical model, viz., overestimation of the temperature gradient in the Fuel Pin Simulator (FPS), continuous temperature decrease throughout the whole transient and underestimation of the upper pool temperature during nominal operations. This has led to improvements made to the initial model to come to a new model, henceforth referenced by “improved model”.

This report consists of seven chapters. Chapter 2 contains a description of the initial model. Modifications made to the initial model to arrive to an improved numerical model are discussed in Chapter 3. The mesh used during the simulations of both models is described in Chapter 4, while Chapter 5 highlights the used numerical settings in both models, such as simulation settings and material properties. In Chapter 6, the PLOH+LOF transient test 2 is described. Simulation results of test 2 obtained using both the initial CFD model as well as those coming from the improved model are shown and discussed in Chapter 7. Finally, some conclusions are given in Chapter 8.

4 Initial Model Description

The CIRCE facility and the ICE test section have been described extensively in previous reports [2]-[5]. It will be repeated here only briefly, focusing on geometry simplifications used in the model.

4.1 Full test-facility geometry.

The CIRCE facility, including the ICE test section, is depicted in Figure 1. It consists of an inner loop and a main pool. The LBE enters the inner loop through a feeding conduit, after which it flows through a flow meter before entering the FPS. The FPS is a mechanical structure representing the heat source of the system. After exiting the FPS, the LBE passes through the fitting volume and flows inside the riser. Inside the riser there is a nozzle installed to allow argon injection, which forces the flow. The LBE subsequently enters the separator. It is open from the top and allows for the separation of the argon, which flows into the cover gas through the free surface, and the LBE, which flows downward into the heat exchanger. Here it gets cooled and eventually re-enters the main pool. Finally, a Decay Heat Removal (DHR) system is installed that serves as heat exchanger in accident scenarios in which the primary heat exchanger stops working.

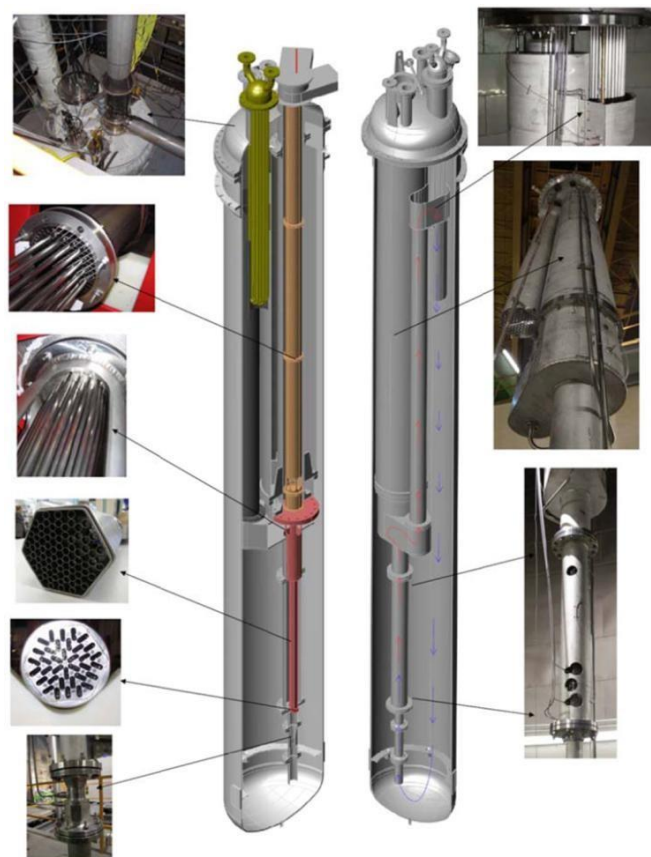


Figure 1: CIRCE-ICE test facility [3].

Figure 2 shows the CAD geometry used for the simulations presented in this report, along with arrows indicating how various parts of the actual test facility are represented. One of the major simplifications made is modelling the test section between the feeding conduit and the fitting volume, which also

includes the flow meter, FPS, the upstream and downstream mixing zones and the release pipe, as one long cylinder with a constant radius. Furthermore, no bolts, flanges, etc. are included in the CAD geometry, and almost all walls have zero thickness, the exception being the heat exchanger wall. Also, the top lid is not included in the geometry. As a matter of fact, the CAD geometry only extends up till the free surface, so no cover gas is present in the model. In the sections below, several parts will be discussed in detail.

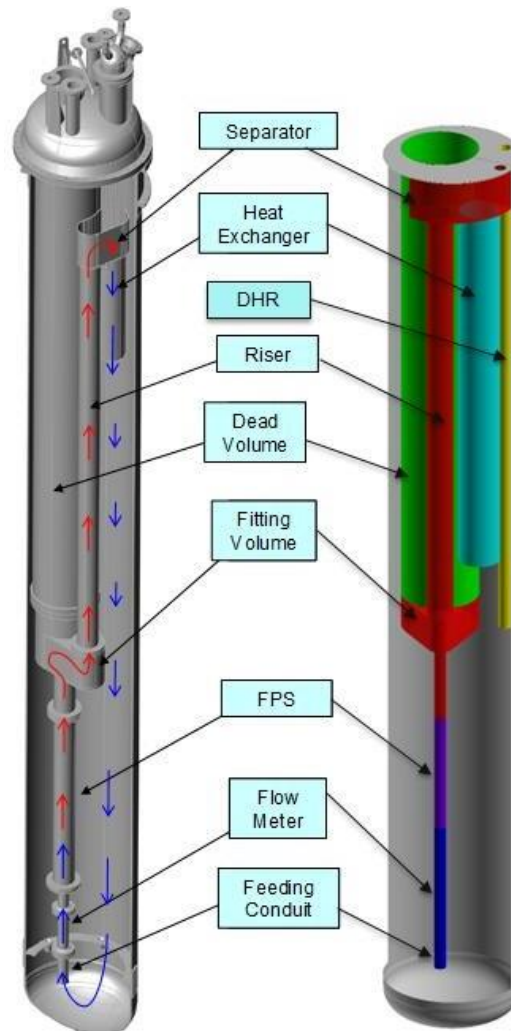


Figure 2: CAD geometry alongside test-facility.

4.2 Fuel Pin Simulator

This section discusses the implementation of the heat source in the CFD model. First, geometry simplifications will be discussed, followed by how the electrical pins that make up the heat source are represented. Finally, the heat input model is described.

4.2.1 FPS Geometry

As mentioned before, the part of the inner loop from the feeding conduit till the fitting volume has been modelled as a single cylinder. This cylinder has a radius of 102,3mm, equal to the radius of the feeding conduit of the test facility. 37 electrical pins serve as heat source of the system, with an active length of 1m. These pins extend all the way through the mixing zones, release pipe (a cylindrical pipe after the FPS) and the fitting volume into the dead volume, where they are attached to electrical wires. A schematic of a cross-cut through the FPS is shown in Figure 3. As can be seen in the figure, the pins are actually located in a hexagonal tube, while the model contains a cylindrical tube. The difference in flow resistance between the two shapes has to be accounted for. Furthermore, the pins aren't physically included in the CAD geometry. Their influence on the flow will be modelled as a porous medium, which will be discussed in more detail in the next section. Modelling of the heat input is discussed in section 2.2.3.

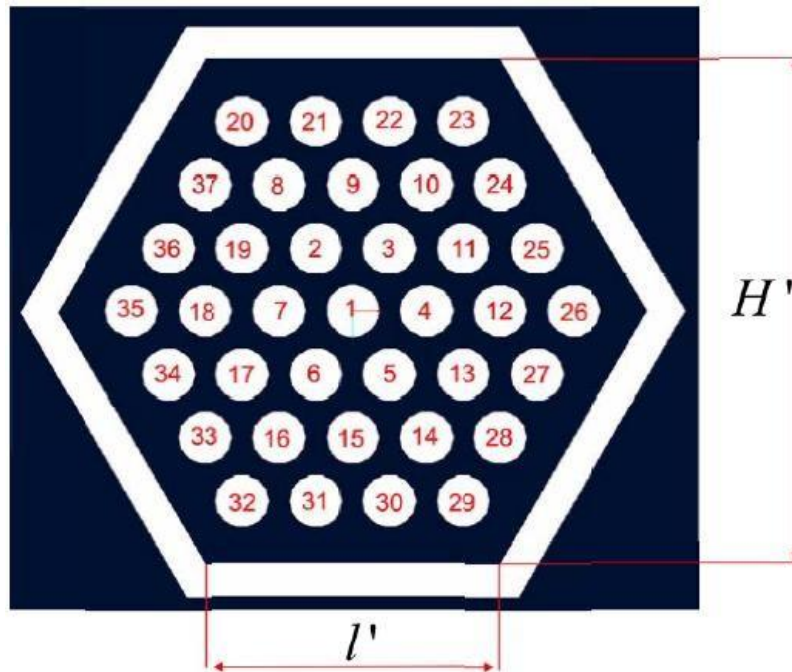


Figure 3: Schematic of the FPS cross section ($l' = 55.4\text{mm}$, $H' = 96\text{mm}$).

4.2.2 Porous Medium Approach

Since the electrical pins aren't physically present in the model, their flow resistance will be modelled by means of a porous medium zone. Porous media are modelled by the addition of a momentum source term to the standard fluid flow equations. The source term is composed of two parts: a viscous loss term (Darcy, the first term on the right-hand side of the following equation), and an inertial loss term (the second term on the right-hand side of the following equation):

$$S_i = - \sum_{j=1}^3 D_{ij} \mu v_j + \sum_{j=1}^3 C_{ij} \frac{1}{2} \rho v v_j$$

where S_i is the source term for the i -th (x , y or z) momentum equation, v is the magnitude of the velocity and D and C are prescribed matrices. This momentum sink contributes to the pressure gradient in the porous cell, creating a pressure drop that is proportional to the fluid velocity (or velocity squared) in

the cell. For the case of simple homogeneous porous media, which is applicable here, the source term reads:

$$S_i = -\frac{\mu}{\alpha} v_i + C_2 \frac{1}{2} \rho v v_i = \nabla p_{porous} = \frac{\Delta p_{porous}}{L_{ref}}$$

where α is the permeability (with dimensions m^2) and C_2 is the inertial resistance factor (dimensions $1/m$), i.e., D and C are diagonal matrices with $1/\alpha$ and C_2 , respectively, on the diagonals (and zero for the other elements). Note that here $\alpha = m^2$ and $C_2 = \frac{1}{m}$, which can easily be verified when realizing that S_i is the change of momentum with time, i.e., $S_i = \frac{\partial \rho u_i}{\partial t} = \frac{kg}{m^2 s^2}$ and $p = Pa = \frac{N}{m^2} = \frac{kg}{m \cdot s^2}$.

In the current simulation, the viscous losses are neglected and thus only the inertial resistance term is considered. If the pressure losses Δp_{porous} over the reference length L_{ref} are known, the inertial resistance factor at a particular flow rate can be determined by:

$$C_2 = \frac{\Delta p_{porous}}{L_{ref} \frac{\rho}{2} u^2}$$

In the above equation, the superficial velocity u^2 needs to be considered, which is the velocity of the fluid if the medium was fully open. It is related to the physical velocity by:

$$v_{superficial} = \gamma v_{physical}$$

where γ is the porosity of the medium defined as the ratio of the volume occupied by the fluid to the total volume. To determine the inertial resistance factor, the total pressure loss needs to be known. Since the model uses a uniform cylinder to represent the inlet and heating part of the inner loop, all pressure losses over the separate parts contained in this uniform cylinder and not directly resolved need to be accounted for. These pressure losses are due to: 1. Venturi-Boccaglio flow meter, 2. heat source, 3. inlet hexagonal wrapper, 4. lower grid assembly, and 5. spacer grids (three in total).

The method used to determine the pressure losses over these various part is similar to the one outlined in [4], i.e., local pressure drop coefficients are determined for each part, which are subsequently combined into an effective pressure drop coefficient. The total pressure drop based on a particular mass flow rate \dot{m} can then be determined using:

$$\Delta p_{fric} = \frac{1}{2} \frac{\dot{m}^2}{\rho_{eff} A_{eff}^2} K_{eff}$$

Table 1 summarizes the contributions to the effective pressure drop coefficients of the various parts for a mass flow rate of 65kg/s. To come to these values, a porosity

$$\gamma = \frac{flow\ volume}{actual\ volume} = \frac{0.5H'l' - 37\pi r_{pin}^2}{\pi r_{FPS}^2} = 0.733$$

was used, as well as a reference temperature of 350°C, which is needed to determine material properties. For a mass flow rate of 65kg/s, the total pressure drop $\Delta p_{fric} \approx 40kPa$. The inertial resistance factor in axial direction $C_2 \approx 9.1/m$. This value was obtained using a reference length $L_{ref} = 1.45m$ longer than just the active part of the Fuel Pin Simulator, reason being that the pins also obstruct the flow in the downstream mixing zone similar to inside the FPS. Beyond the DMZ, the LBE flows into the

Release Pipe, which has a larger diameter. There, the flow area taking into account the pins is similar than the flow area in the model without the pins.

As for the inertial resistance factors in the two directions perpendicular to the axial directions, in a Cartesian coordinate frame, they were set at a factor of 1000 larger than the one in axial direction. The reason for such large resistance factors is that, in reality, the flow is blocked in radial direction due to the pins.

Relevant part	Local pressure drop coefficient [-]
Flow Meter	1.593
Heat Source	1.578
Inlet Hexagonal Wrapper	0.19
Lower Grid Assembly	2.277
Spacer Grids (3x)	1.431
Total	7.068

Table 1: Local pressure drop coefficients in various parts of the FPS cylinder.

4.2.3 Heat Source Model

The power input of the test facility is modelled using a Volumetric Heat Source (VHS) with units W/m^3 :

$$Q_{FPS} = \frac{P_{FPS}}{V_{FPS}},$$

Where P_{FPS} is the power supplied to the electric pins in the FPS and V_{FPS} is the volume of the FPS in the model. This kind of model allows for a very accurate control over the amount of heat added to the system, and the CFD model automatically adds the right amount of heat to a particular cell based on its volumetric size. Since the velocity of the LBE inside the FPS is nearly uniform, it results in a nearly linear temperature profile.

4.3 Argon Injection

To avoid the computational cost of a two-phase flow approach, the argon injection to force the flow, which basically is a mock-up of a pump, is not included explicitly, but accounted for through a Volumetric Momentum Source (VMS, $[N/m^3]$) in the riser, much like what was used to model the heat input in the FPS. Such a model adds a source term to the momentum equations. However, there isn't a clear one-on-one relation between the desired mass flow rate and the value to be used for the VMS due to the presence of buoyancy. Hence, trial-and-error is used to come to the correct input value based on a targeted mass flow rate. E.g., for $P_{FPS} = 600kW$ and a desired $m = 65 kg/s$, a value of $VMS_{Riser} = 12.250 N/m^3$ is needed. This is valid for LBE temperatures in the 300 - 400°C range.

4.4 Cover Gas & Free Surface

The same assumption made for the argon injection is used in terms of the cover gas in the CFD model. Thus the CAD geometry only extends up till the free surface. This free surface is modelled as an impenetrable wall with free-slip condition and is maintained at a fixed height. The fixed height assumption

is very reasonable for Steady-State simulations, however, it is expected to change during transient runs. To estimate this change in height, let's assume a decrease in overall average temperature of 300°C, which is quite reasonable for a switch from forced convection to natural convection. This temperature decrease results in a density increase of about 0.4% (see section 4.2). On a total vessel height of about 7.5m, that's a drop in free surface of 3cm. The aforementioned assumption is hence reasonable.

4.5 Heat Exchanger

In this section, the modelling of the heat exchanger (HX) will be discussed in detail.

4.5.1 HX Geometry

The primary heat exchanger in the CIRCE-ICE test facility is a low-pressure boiling water shell heat exchanger consisting of 91 bayonet tubes, as shown in Figure 4. More details can be found in [2] and [3]. Since the main interest is the heat being removed by the heat exchanger and the resulting temperature profile, and not so much the flow field inside the heat exchanger, the tubes are not explicitly included in the geometry. To compensate for the friction losses due to the bayonet tubes, the heat exchanger will be modelled as a porous medium as discussed in the next section.



Figure 4: View of the ICE HX installed into the test section.

4.5.2 Porous Medium Model for the HX

An identical porous medium model as used for the FPS will be used for the HX. Thus the main task is to estimate the pressure losses due to the bayonet tubes at a particular mass flow rate and subsequently determine the inertial resistance factor. The pressure loss due to friction can be estimated using the following equation:

$$\Delta p_{fric} = \frac{1}{2} \frac{m^2}{\rho_{HX} A_{HX}^2} K_{HX} = \frac{1}{2} \frac{m^2}{\rho_{HX} A_{HX}^2} f_{HX} \frac{L_{HX}}{D_{r,HX}},$$

here, $L_{HX} = 3205\text{mm}$ is the length of the heat exchanger, $D_{h,HX} = 22\text{mm}$ its hydraulic diameter and f_{HX} the Darcy-Weisback factor. To determine the latter, the Churchill Correlation [8] has been adopted. This correlation applies to a wide range of Reynolds number, spanning the laminar, transition and turbulent regimes:

$$f = 8 \frac{8}{Re}^{12} + \frac{1}{A+B}^{12}, \quad A = 2.457 \ln \frac{1}{7 Re^{0.9+0.27 \varepsilon D_h}^{16}}, \quad B = \frac{37530}{Re}^{16},$$

where ε is the average roughness of the components, assumed to be zero here. Table 2 summarizes the relevant parameters, assuming an average temperature of 350°C and a mass flow rate of 65 kg/s :

Parameter	Model input
f_{HX}	0.026 [-]
Δp_{fric}	371 [Pa]
$C_{2,HX} - \text{axial}$	4.76 [1/m]
$C_{2,HX} - \text{transversal}$	4760 [1/m]
γ_{HX}	0.499

Table 2: HX porous medium input parameters for a mass flow rate of 65 kg/s.

4.5.3 Heat Sink Model.

Consistent with the FPS, Volumetric Heat Source is used. However, this time it's negative, as it's supposed to be a sink, and it won't have a constant value. Instead, the following model is used:

$$Q_{HX} = \frac{\rho c_p}{\tau} T_0 - T,$$

here, ρ is the density of the LBE, c_p the specific heat, T the actual, current, temperature of the LBE, T_0 a target temperature and τ is a relaxation time. Such a model introduces two additional degrees of freedom, T_0 and τ , which allows for a better control over the temperature in the simulation. Thus, if for example the temperature suddenly rises, the heat removed through such a model will also increase, thereby suppressing fluctuations. The target temperature T_0 is somewhat representative of the water/steam temperature on the secondary side of the heat exchanger, while τ is similar to a residence time of the LBE inside the heat exchanger. These parameters are tuned such to get the desired heat removed by the heat exchanger for a particular test.

4.6 Decay Heat Removal System

In case of accident scenarios in which the primary heat exchanger is no longer operational, the DHR serves as the heat sink of the system. It consists of a single bayonet tube, with LBE flowing in through slots from the top and leaving at the bottom, and cold air coming in from the top, flowing downwards before turning around and getting heated while flowing upwards and finally leaving at the top. A schematic is shown in Figure 5. The air component of the DHR will not be included in the CFD model; only the LBE part. Therefore, only the annular cylinder through with the LBE flows is incorporated in the model, while the air side is represented as an empty cylinder. Also, the slots have been replaced by a simple opening at the top.

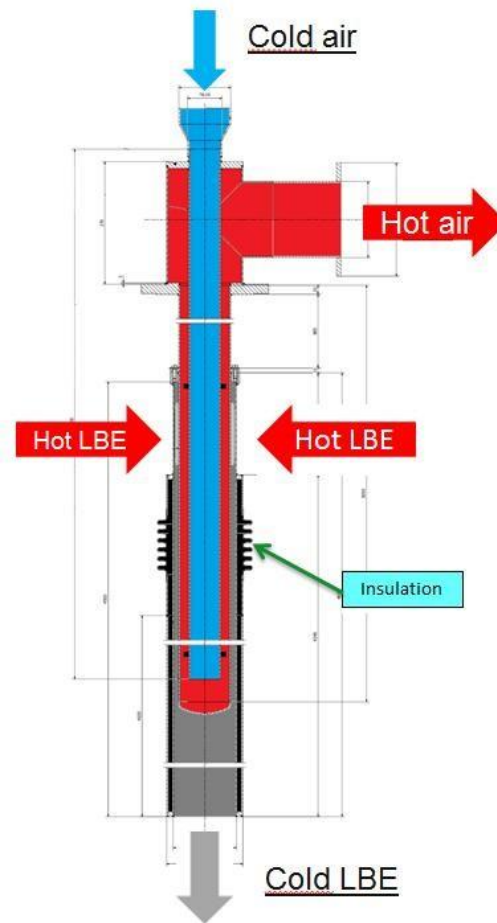


Figure 5: Schematic of the DHR.

Regarding the heat being removed from the system, this is modelled as a Volumetric Heat Sink. Similar to the FPS, it assumes a constant value, though since it is a sink it is negative:

$$Q_{DHR} = -\frac{P_{DHR}}{V_{DHR}}$$

4.7 Conjugate Heat Transfer

One of the more important phenomena taking place during the operation of the test facility is Conjugate Heat Transfer (CHT). This contributes to the heat balance of the system in two ways: 1) heat transfer from the hot inner loop to the colder main pool through the inner structures, e.g., through the fitting volume walls, and 2) heat transferred from the main pool to the environment through the vessel walls, and, to a lesser degree, through the dead volume walls. In order to get an accurate model, and to get a proper stratification in the pool, CHT should not be neglected.

In the current model, in which almost all the walls have zero physical thickness, the Shell Conduction option of Fluent [6] is used. This option allows to create additional layers of cells in walls, in which, during the simulation, the heat equation in the following form is solved:

$$\frac{\partial T}{\partial t} = \frac{k}{\rho c_p} \frac{\partial^2 T}{\partial x^2} + \frac{\partial^2 T}{\partial y^2} + \frac{\partial^2 T}{\partial z^2} ,$$

where T is the temperature, k the thermal conductivity of the material, ρ its density and c_p its specific heat. This Shell Conduction option requires the specification of the thickness of the layer as well as the material, and takes into account heat transfer through the walls, as well as in-wall heat transfer and

thermal inertia of the walls. The latter is important during transient runs, when heat contained in the walls slows down the cooling of the system. Finally, it allows for the creation of multiple layers. For example, around the riser of the test facility, an additional cylinder is placed that contains air. This means there are three layers of material needed to represent the CHT from the riser to the main pool: 1) the riser tube itself, 2) the layer of air, and 3) the cylinder in which the air is contained.

5 Model Modifications

The initial model discussed in the previous chapter was used in [7] to perform transient test 1. This report presents results using the same model, but then for transient test 2. Transient test 2 (see Chapter 6 for details) is very similar to transient test 1, though it's quite a bit shorter, ~20hrs for test 1 and ~6hrs for test 2, and the nominal power is 600kW in test 2 compared to 800kW for test 1. Results of the simulation using this initial model are presented in Chapter 7.

As it turns out, results for this test showed similar inconsistencies when compared with the experiment as were previously found and reported for test 1, namely:

- Too low temperatures in the upper part of the main pool during the steady state.
- Continuous cooling throughout the whole transient part of the test.
- Too big of a difference between FPS inlet and outlet temperatures during the whole test.

Furthermore, for test 2 it was found that the final mass flow rate was lower than the experiment. To overcome these differences, the following modifications were made to the initial model to arrive to the improved model.

- Heat transfer from the riser to the surrounding main pool was increased by reducing the thickness of the air layer between the two concentric cylinders comprising the riser. This additional heat transfer reflects the radiative heat transfer contribution, which becomes significant at such high temperatures. Initially, only heat conduction by the air was taken into account.
- The thickness of the insulation material around the main vessel was changed from 20mm to 70mm, with the exception being at the level of the separator and above, where it's set to a thickness of 5mm. This matches much better the reality, where there's a thick, old, layer of insulation around the whole vessel up till the separator. From there upwards, some metal clamps are present to support the facility. These clamps act as thermal bridges, removing quite some heat through conduction.
- Actual power supplied to the LBE was decreased to compensate for loss due to Joule heating in the dead volume [9]. It is reduced from 600kW to 550kW for the steady state and from 30kW to 26kW for the transient. It's not precisely known how much heat is lost due to Joule heating, but reducing the power input results in a better agreement between simulation and experiment for the FPS inlet and outlet temperatures.
- Friction factors inside the FPS were reduced from 9.639 m^{-1} to 5.5 m^{-1} to better match actual velocities. The initial values were obtained using the nominal mass flow rate of 65kg/s, while in the transient it is significantly lower. .
- A heat sink model similar to the one used for the main heat exchanger was used for the DHR, to better represent the secondary side. The initial model still uses a constant volumetric heat sink, with values of 26kW and 20kW, representing the drop in air flow rate during the transient.

6 Mesh Generation

To create the mesh used for both models, the mesh generation software GAMBIT [10] is used. This software is quite flexible in its use and allows for a large control over the cell sizes and cell growth. The whole geometry is subdivided into various volumes such that most of the computational domain contains hexahedral cells using the Cooper Scheme. Only two parts have tetrahedral cells, viz. a part of the Main Pool just above the fitting volume and in the very bottom of the main vessel. However, in both these parts the LBE is rather stagnant, so it is expected to not adversely affect the numerical simulations.

Boundary layers are used in the Fuel Pin Simulator, the riser and the heat exchanger, where the first layer thickness was chosen such that $y^+ > 30$ everywhere in the inner loop. Figures 6 and 7 illustrate what the mesh looks like at two different levels of the geometry. As can be seen, smaller cells are used in the inner loop, where velocities and gradients are larger. In the more stagnant main pool, cells are grown to larger sizes. A summary of the mesh statistics is introduced in Table 3.

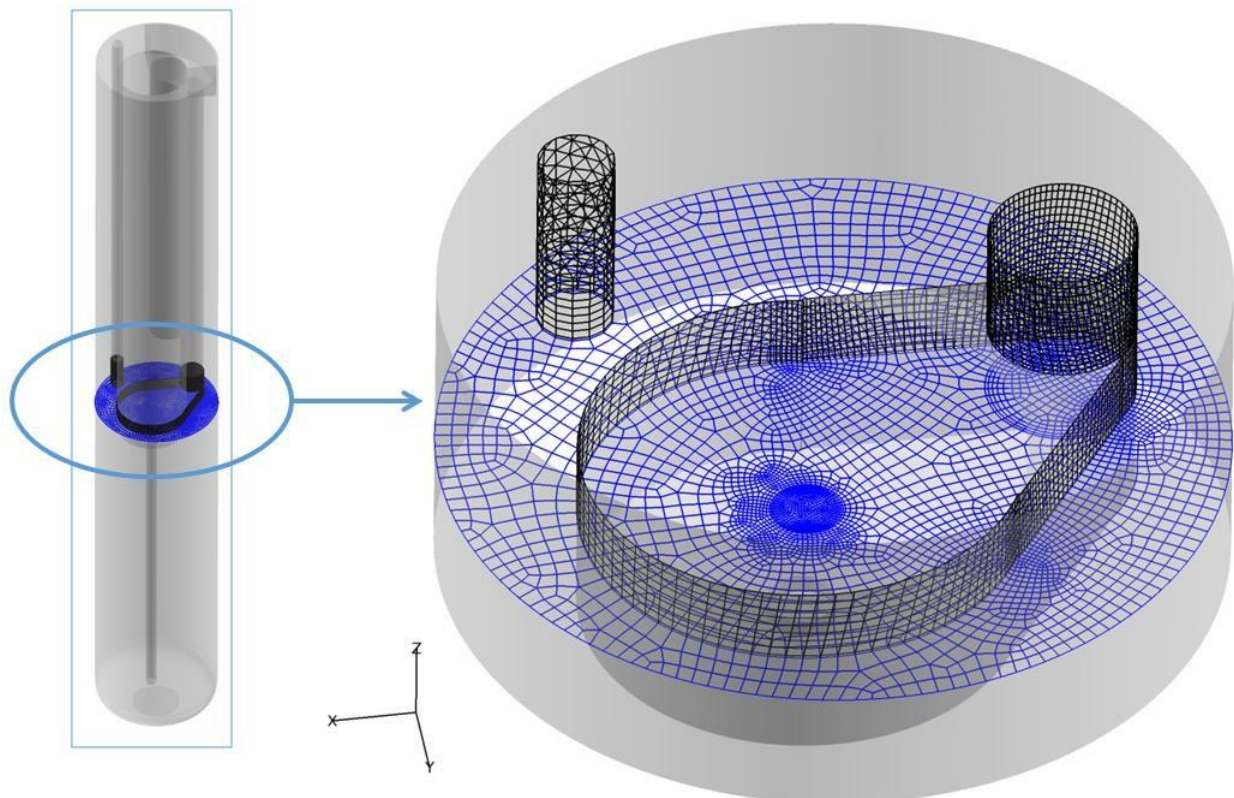


Figure 6: Cross-cut through Fitting Volume showing the mesh. Also shown are various wall meshes.

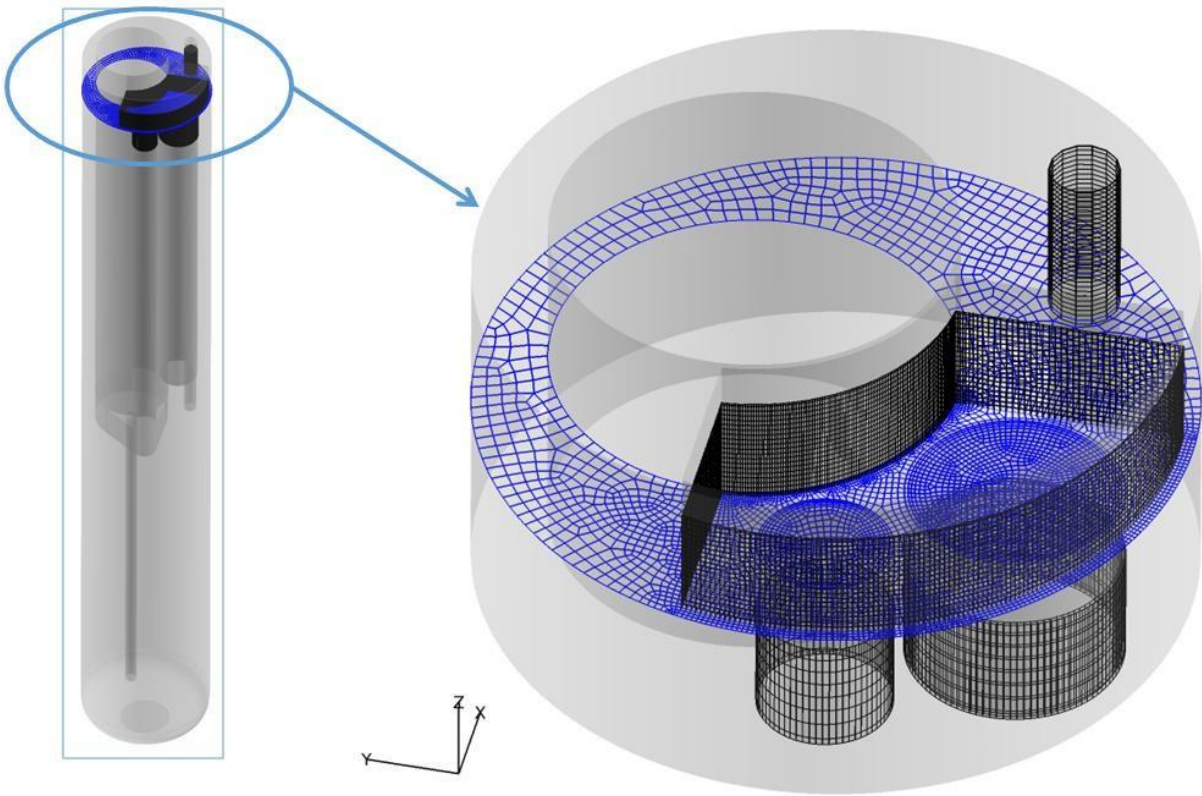


Figure 7: Cross-cut through the Separator showing the mesh. Also shown are various wall meshes.

Mesh parameter/statistic	Value
Number of volumes	40
Total number of cells	2.285.220
Total number of tetrahedral cells	238.222
Total number of tetrahedral cells	2.046.998
Maximum skewness	0.94
Number of cells with skewness > 0.9	4
Largest aspect ratio	61

Table 3: Various mesh statistics.

7 Numerical Settings

In this section, the numerical settings used for both models are discussed. First, the most relevant simulation settings are presented along with boundary and initial conditions. Following, the material properties are given.

7.1 Simulation Settings

To obtain the flow and temperature fields, the Navier-Stokes and energy equations are solved numerically in the RANS context. The corresponding settings are summarized in Table 4.

Settings	
CFD code	ANSYS Fluent 17.2
Turbulence model	Realizable κ - ϵ model
Wall treatment option	Enhanced Wall Treatment
Liquid metal heat transfer	Turbulent Prandtl number = 2.0 [11]
Velocity-pressure coupling	SIMPLE algorithm
Gradient discretization	Least squares cell based
Spatial discretization	2 nd order
Linear system iterative method	Gauss-Seidel
Boundary conditions - flow	No-slip (except for free surface)
Boundary conditions - temperature	Conjugate Heat Transfer

Table 4: Relevant simulation settings.

Regarding the initial conditions used to get to a steady-state flow, the flow field starts from rest. The temperature in the main pool is initialized at a reasonable low temperature, while the inner loop has a corresponding high temperature. Inside the FPS and HX, the temperature varies linearly between these two temperature. This initial temperature field gives faster convergence than initializing at one fixed temperature.

7.2 Material Properties

The following temperature dependent equations for the density ρ_{LBE} [$kg\ m^3$], dynamic viscosity μ_{LBE} $Pa \cdot s$, thermal conductivity k_{LBE} $W\ mK$ and specific heat c_{pLBE} $J\ kgK$ of Lead-Bismuth Eutectic, taken from the LBE handbook [12] are, are implemented in the CFD code:

$$\begin{aligned}\rho_{LBE} &= 11065 - 1.293T, \\ \mu_{LBE} &= 4.94 \cdot 10^{-4} e^{754.1 T}, \\ k_{LBE} &= 3.284 + 1.617 \cdot 10^{-2}T - 2.305 \cdot 10^{-6}T^2, \\ c_{pLBE} &= 164.8 - 3.94 \cdot 10^{-2}T + 1.25 \cdot 10^{-5}T^2 - 4.56 \cdot 10^{-5} T^2,\end{aligned}$$

here, temperatures are always in Kelvin. Material properties are also needed for the walls. These are made either of Stainless Steel grade AISI 304 or AISI 316L. Their properties are quite similar, and therefore it was chosen to use the properties of SS AISI 316L for all walls. These are given by [13]:

$$\rho_{SS} = 8110.5 - 0.44476T$$

$$k_{SS} = 10.145 + 0.01253T + 2.1927 \cdot 10^{-6}T^2$$

$$c_{pSS} = 306.682 + 0.74277T - 7.5148 \cdot 10^{-4}T^2 + 3.10023 \cdot 10^{-7}T^3$$

Furthermore, material properties of ceramic fibre, air and argon gas are needed. The former is used as an insulator to prevent heat losses to the environment. Air is used to minimize heat transfer from the inner loop to the main pool and argon is the cover gas. Values of the properties for these materials are summarized in Table 5. Piecewise-linear indicates that values for these properties are specified at particular temperatures, as provided by the references, and linear interpolation is used to obtain values at intermediate temperatures.

	Density [$kg\ m^3$]	Thermal conductivity $W\ mK$	Specific heat $J\ kgK$
Air [14]	0.566	Piecewise-linear	Piecewise-linear
Ceramic fibre [manufacturer]	130.0	Piecewise-linear	1130.0
Argon [Fluent database]	1.6228	520.64	0.0158

Table 5: Material properties for various materials.

Densities of all these materials are kept constant, with values corresponding to a temperature of 350°C. The reason for this is that we don't take into account thermal expansion of any wall or insulation material. This also applies to the steel walls. Argon properties are kept constant since it's being re-circulated and maintained at a nearly fixed temperature.

8 Description of SESAME WP3 Test 2

A thorough overview of SESAME WP3 Test 2 can be seen in Table 6. It consists of an initial ramp-up to a steady-state flow with a total heat input of about 600kW and an LBE mass flow rate $m = 60 - 70 \text{ kg/s}$. Furthermore, heat is removed by the main heat exchanger at a rate of 500 kJ per second. After having reached steady-state and running in steady-state, a Protected Loss Of Heat and Loss Of Flow (PLOH + LOW) accident scenario is mimicked. During such an accident scenario, the pumps stop working and the fuel operates at a decay heat, which is about 3-5% of its nominal power. Furthermore, the main heat exchanger is isolated from the system and the DHR serves as the heat sink of the system. In practise, the system goes from forced convection mode into natural convection at a much lower power.

Nominal Steady State	PLOH+LOF Transient
FPS nominal power $\approx 600\text{kW}$	Core "scram" at about 30 kW (decay power)
LBE = 60 – kg/s (by gas lift)	LBE circulation through natural convection.
Argon mass flow rate $\approx 2.7 \text{ NI/s}$	No forced circulation
Average velocity into the HS $\approx 1\text{m/s}$	Natural circulation due to decay heat.
Pool LBE initial temperature $\approx 280^\circ\text{C}$	Pool temperature to be determined.
Vessel heating system: not active	Vessel heating system: not active
HX water flow rate $\approx 0.6 \text{ kg/s}$	Isolation of the feed water
HX inlet water at room temperature	Isolation of the feed water.
HX thermal power removed $\approx 500\text{kW}$	Isolation of the main HX (not operational)
DHR: not active	DHR:active

Table 6: Description of accident scenario Test 2.

The time evolution of the experiment is described in Table 7. The total test consists of about 6hrs, of which the approximately first 2.25 hours are used to reach a steady-state and the second half of the experiment is allocated to the transient.

FULL POWER RUN	
Event	Time
Power ramp (0-600kW)	0.24h → 0.28h
Full power (600kW)	0.28h → 2.28h
Water injection (main HX)	0.35h → 2.28h
Argon injection	0.16h → 2.28h
TRANSITION	
Event	Time
Power Ramp (600-30 kW)	2.25h → 2.28h
Air injection (DHR)	2.28 h → 4.9 h (0.325 kg/s) 4.9 h → 6.15 h (0.22 kg/s)

Table 7: Time evolution of SESAME WP3 Test 2.

9 Results

In this chapter, results of the simulations using both the initial as the improved model will be compared to the experiment as well as to each other. First, results for the steady state part of the test are shown, followed by those of the transient.

9.1 Steady State Results

Before performing the transient part of the test, the proper steady-state flow has to be reached. In the experiment the LBE initially is at rest with a temperature of about 280°C. It is subsequently forced to flow by means of argon injection, resulting in a mass flow rate of around 65 kg/s. The nominal heat input by the FPS is about 600kW. This part of the experiment lasts for ~2.3hrs before the transient starts. We want to reproduce the flow and temperature conditions of the LBE before the transient is started.

In the simulations the flow is started from rest. The initial pool and inner loop temperatures are 280°C and 340°C, respectively, with a linear variation between these two temperatures inside the FPS and HX. This way of initializing the temperature is done to reach convergence faster. The Volumetric Momentum Source (VMS) inside the riser is tuned in order to get the proper mass flow rate. Table 8 gives an overview of some relevant values of the simulations, for both the initial as the improved model, once it reaches a steady-state condition, along with experimental values right before the transient starts.

As can be seen, there's some discrepancy between the power input in the simulations and in the experiment. A lower heat input in the model was used because some of the power supplied to the electrical cables in the experiment is lost due to Joule heating inside the Dead Volume [9]. This means less power is available for heating of the LBE, with an estimated loss of about 3-5%. Heat removed by the heat exchanger in the model is very close to what is removed in the experiment. Also, the mass flow rate inside the inner loop agrees very well due to the tuning of the VMS in the riser.

The inlet and outlet temperatures of the inner loop, i.e., $T_{in,FPS}$ and $T_{out,HX}$ agree very well, with the former being almost exactly equal to the experimental value, while the latter is off by ~5°C. This is very important because it means that LBE flows out of and into the main pool at approximately the correct temperatures. Other inner loop temperatures differ more, but are still reasonably close.

Comparing the values for the initial model with the improved model, one can see that reducing the power input has as effect that the outlet temperature of the FPS is closer to the experimental one. This results in other inner loop temperatures matching better the experimental values as well, justifying lowering the power input and suggesting that more than just 3-5% of heat is lost due to Joule heating, perhaps as much as 10%.

The inlet temperature of the heat exchanger still differs quite a bit. This could be due to the measurement taken in a cold spot, as it is rather odd that temperatures suddenly drop by 13°C when exiting the riser and entering the heat exchanger, especially considering they are both at comparative levels.

	Initial model	Improved model	Experiment
Thermal Power in the FPS	580kW	550kW	600kW
\dot{m} LBE in the FPS	65.2 kg/s	64.6 kg/s	~65 kg/s
\dot{m} LBE in the DHR	0.0 kg/s	0.0 kg/s	0.0 kg/s
$T_{inlet,av}$ FPS	275.8°C	276.1°C	276.0°C
FPS (Fitting Volume)	338.7°C	335.8°C	334.2°C
$T_{inlet,av}$ Riser	334.9°C	332.3°C	329.2°C

Riser	334.1°C	330.0°C	331.2°C
$T_{inlet,av}$ HX	332.9°C	328.8°C	317.7°C
HX	272.5°C	271.9°C	267.0°C
$T_{inlet,av}$ DHR	325.2°C	319.3°C	318.7°C
DHR	281.4°C	278.4°C	280.3°C
Q_{water} removed by the HX	510kW	510kW	500 kW

Table 8: Steady-state conditions comparison between simulation and experiment.

An important goal of the project is to reproduce the stratification of the Lead-Bismuth Eutectic inside the main pool. This stratification is caused by heat losses from the inner loop, through the structure walls, to the main pool. Figure 8 shows a comparison between the simulations and experiment of the stratification for the steady-state flow. Here, a depth of 0m corresponds to the bottom of the separator and a depth of 7m to a level slightly below the inlet of the inner loop. Overall, a good agreement is found in both models in the lower part of the vessel. The location of the steep temperature gradient around a depth of 4m, which corresponds to the fitting volume level, is properly captured. This steep temperature gradient is caused by large heat losses from the LBE inside the fitting volume, consisting of single-layered steel walls of about 10mm thick, to the main pool. In comparison, the FPS and riser are better insulated due to a double layer of steel with either air or stagnant LBE in between, resulting in much lower heat losses to the main pool.

The magnitude of the steep temperature gradient, as well as temperatures in the top of the pool, are better predicted by the modifications made to the initial model. This is mainly a result from the increased heat losses from the riser to the main pool, where the air layer thickness was decreased by a factor of 100, and the changes made to the thickness of the insulation material around the main vessel.

Some additional results of the improved model are shown in figures 9 and 10, with the former showing temperature and vertical velocity profiles on a vertical cut through the main heat exchanger, and the latter showing temperature distributions on various vertical cuts through the system. Figure 3 shows that there isn't much of a temperature variation on a horizontal plane; most differences occur vertically.

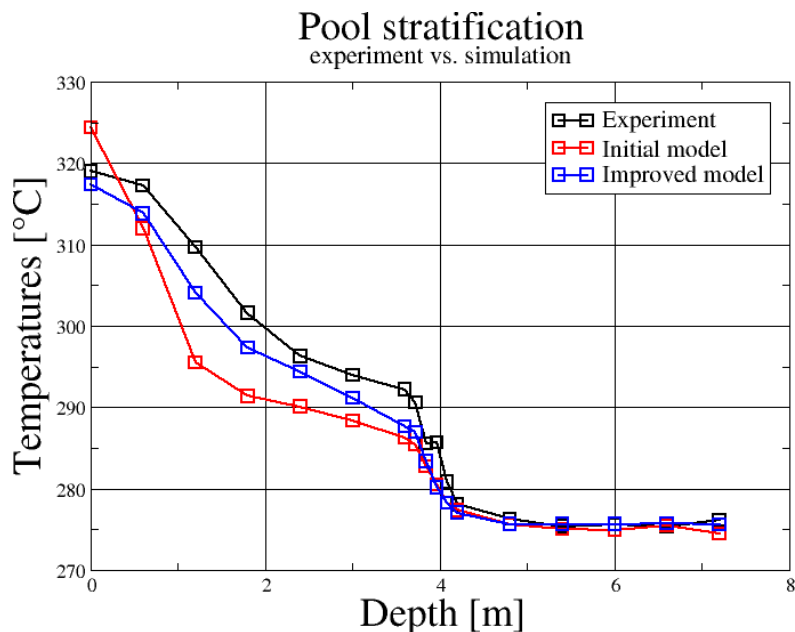


Figure 8: Stratification comparison inside the Main Pool.

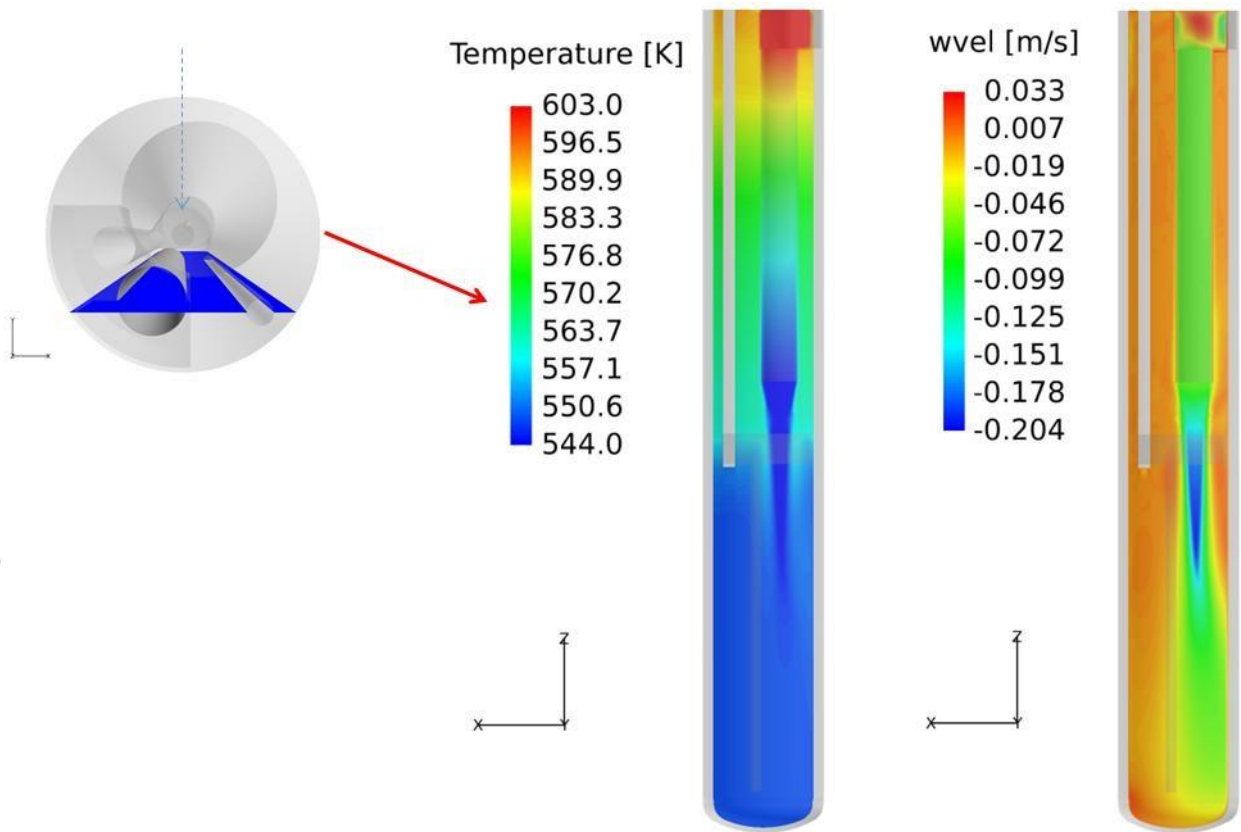


Figure 9: Temperature (middle) and vertical velocity (right) profiles on a vertical plane through the centre of the Heat Exchanger.

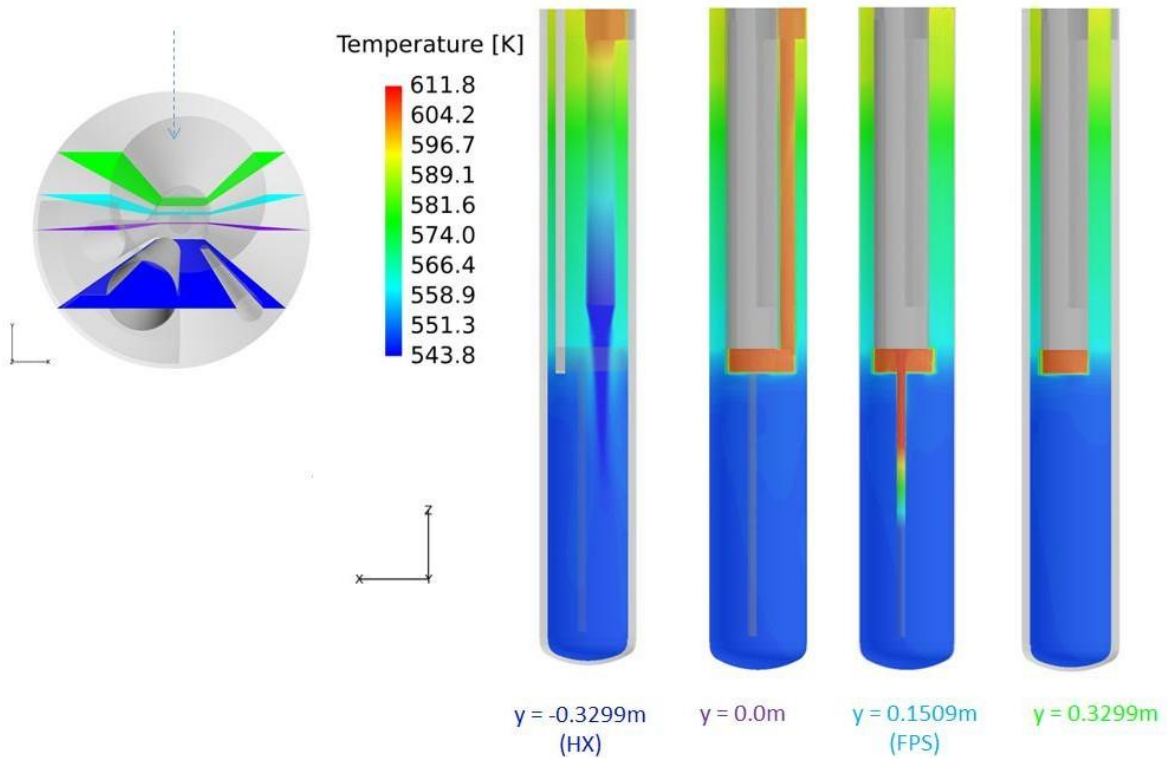


Figure 10: Vertical temperature profiles at, from left to right, $y = -0.1509\text{m}$ (Heat Exchanger), $y = 0.0\text{m}$ (centre Vessel), $y = 0.1509\text{m}$ (FPS) and $y = 0.3299\text{m}$.

9.2 Transient Results

As mentioned in Chapter 6, after approximately 2.28hrs of operating at 600kW, the FPS is switched to decay heat mode, with a power input of ~30kW. The flow is no longer driven by the argon, resulting in a transition from forced convection to natural convection. Furthermore, the decay heat is removed by the DHR, as the HX is no longer operational as well. Figure 11 shows the power added to the system by the FPS on the left and the heat removed by the DHR on the right as function of time for the experiment. As can be seen, the FPS delivers about 30kW in the decay heat mode, while the thermal power removed by the DHR initially is about 30kW when the transient sets in. It subsequently drops slowly to about 25.0 kw, with a rapid decrease to a value of 20.0 kW after almost five hours. It then remains constant till the end of the experiment.

To model the transition from forced to natural convection, both the initial and the improved model are divided into two parts. The first 2.28 hrs represent the steady-state, forced convection, flow. It starts from when the simulation has reached a steady-state, so it does **not** represent or include the spin up from rest to the steady-state condition. After 2.28hrs, the simulation switches to transient conditions. For the initial model, this means a volumetric heat source of 30kW in the FPS with initially a volumetric heat sink of 26.0kW in the DHR, which drops to 20.0kW after 4.94hrs. The riser and heat exchanger are turned off. An overview of the conditions used for the initial model is given in Table 9.

For the improved model, the steady-state part of the test is approached in a similar way, with the exception being the modifications made as outlined in Chapter 3. The biggest difference though takes place in modelling the transient part, as the improved model uses a volumetric heat sink model similar to the one used in the main heat exchanger. The parameters of this model, viz. T_0 and τ of $Q = \frac{\rho c_p}{\tau} (T_0 - T)$ were chosen such that the total heat removed by the DHR during the simulation is about equal to that removed during the experiment.

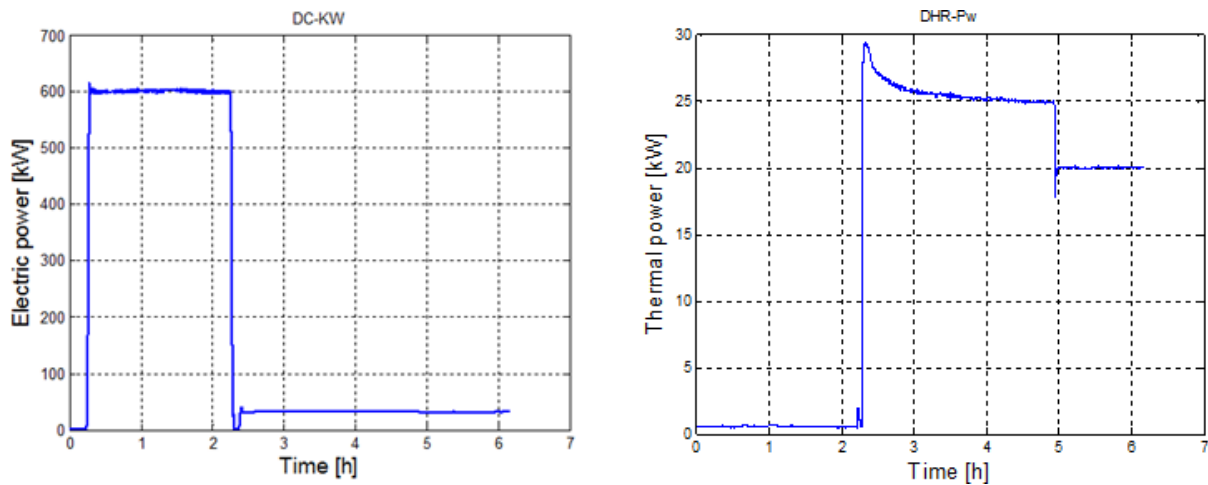


Figure 11: FPS input power and DHR heat removed as function of time for the experiment.

Event	Time
Full power: 600kW	0h-2.28h ≈ 800sec
Transient 1: FPS = 30kW, DHR = 26.0kW	2.28h – 4.94h = 17,800s
Transient 2: FPS = 30kW, DHR = 20.0kW	4.94h – 6.16h = 22,000s

Table 9: Simulation set-up of the steady-state and transient parts.

A comparison between the LBE mass flow rates in the inner loop for the experiment and numerical simulations is depicted in Figure 12. The general behaviour of the curve is well recovered in both

simulations, especially considering that, during the transient part, the LBE circulates through natural convection, i.e., it is no longer an input but a result of the simulation. The initial model though under predicts the final mass flow rate. This is corrected in the improved model by adjusting the friction factors, which in the initial model were based on the steady-state mass flow rate, resulting in too high friction factors and therefore in a too low mass flow rate.

Figures 13 shows the inlet and outlet temperatures of the FPS for both the experiment and the numerical simulations. The initial flat temperatures found in the CFD analyses (from $t = 0$ hrs to $t = 2.28$ hrs), are due to the fact that, as mentioned before, the simulation doesn't include the start up from rest but has constant conditions throughout the steady-state part. The temperature evolution during the PLOH+LOF accident scenario is quite different between the experiment and simulation using the initial model. For the outlet temperature of the FPS, it does recover an initial strong drop followed by a slight increase. However, the model then proceeds to cool for the rest of test, never reaching a steady temperature like is found in the experiment. This steady cooling is also found in the evolution of the inlet temperature.

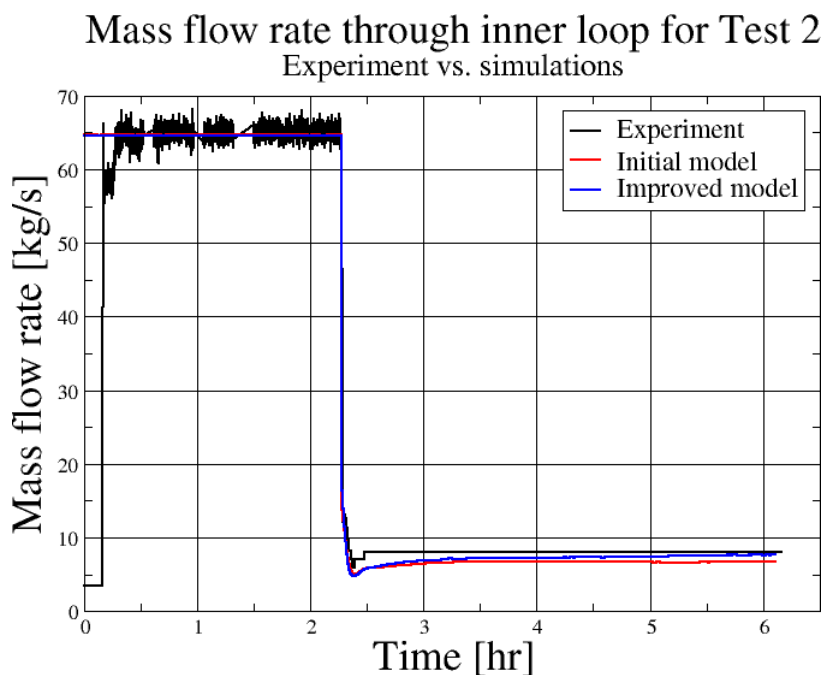


Figure 12: Mass flow rate through the inner loop as function of time.

With the improved model, both the inlet and outlet temperatures level off to a near constant value. The inlet temperature agrees nearly perfectly with that of the experiment, while the outlet temperature is a couple of degrees higher. This levelling off is a result of using a heat sink model with cooling rate dependent on the actual temperature, instead of a constant value.

Finally, the temperature difference between the inlet and outlet of the FPS is closer with the improved model than with the initial model, justifying using a lower power input in the former.

The change in time of the inlet and outlet temperatures of the heat exchanger during the experiment and simulations is shown in figure 14. For both models, the profiles of both temperatures agree reasonably with those of the experiment; the inlet temperature in both cases shows an initial strong drop followed by a slower decrease, while the outlet temperature initially increases and subsequently decreases. Consistent with what was observed for the FPS temperatures, they keep decreasing in the simulation using the initial model, while more of a levelling off is seen with the improved model. Also, the final temperatures using this improved model approaches well those of the experiment.

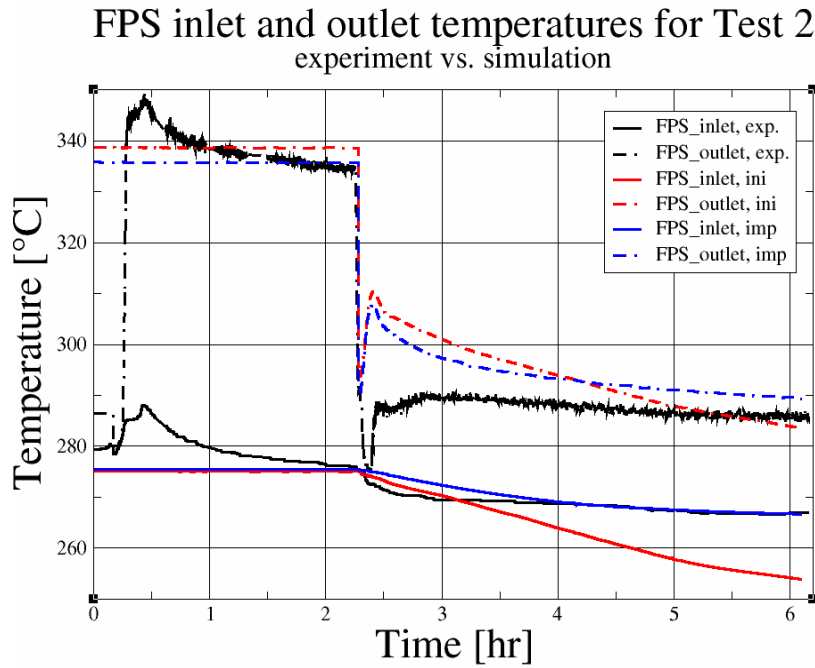


Figure 13: Comparison between inlet and outlet temperatures of the FPS between the experiment and simulation.

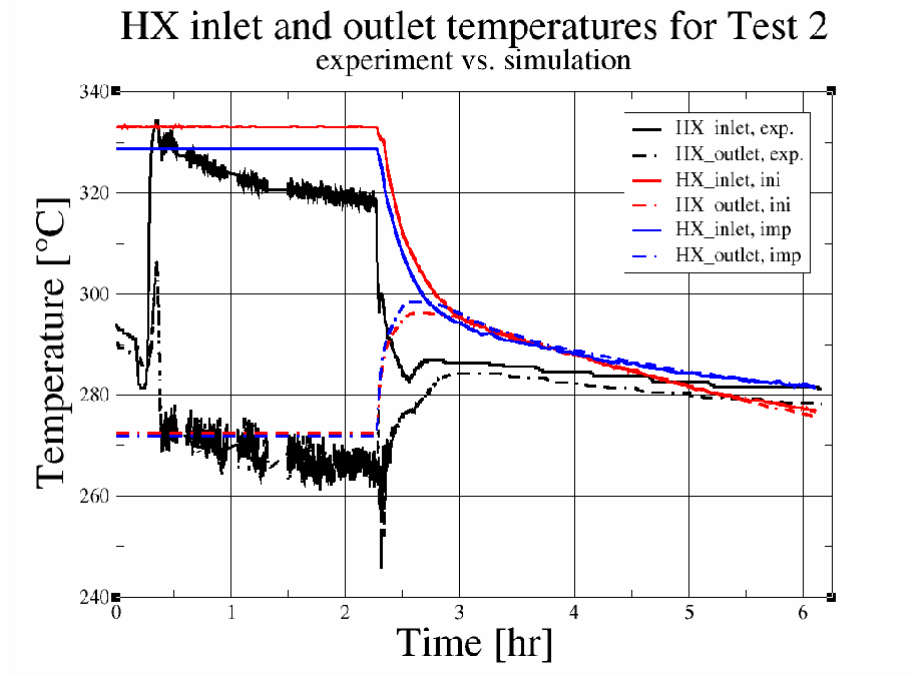


Figure 14: Comparison between inlet and outlet temperatures of the HX between the experiment and simulation.

Finally, a comparison of the stratification in the main pool between the experiment and numerical findings using the improved model is presented in figure 15. The best agreement between the two profiles is found at the end of the test, after 6.1hrs, when the stratification resolved by the simulation is nearly equal to that resulting from the experiment, with only a few degrees difference in the top part of the vessel. This indicates that during the transient part of the simulation, the total amount of heat removed by the DHR is very close to that of the experiment. This is a good result, as this was used, among others, as input to calculate the parameters of the DHR's heat sink model. At the other two instances, the temperature profiles in the main pool of the experiment are below those of the model, indicating that stronger cooling occurs in the experiment for the first part of the test than what is found in the simulation. At $t = 4.5$ hrs, the temperature in the bottom of the pool already agrees between the experiment and the simulation though, as well as the location of the stratification inside the pool. Only the temperature of the top part is lagging behind.

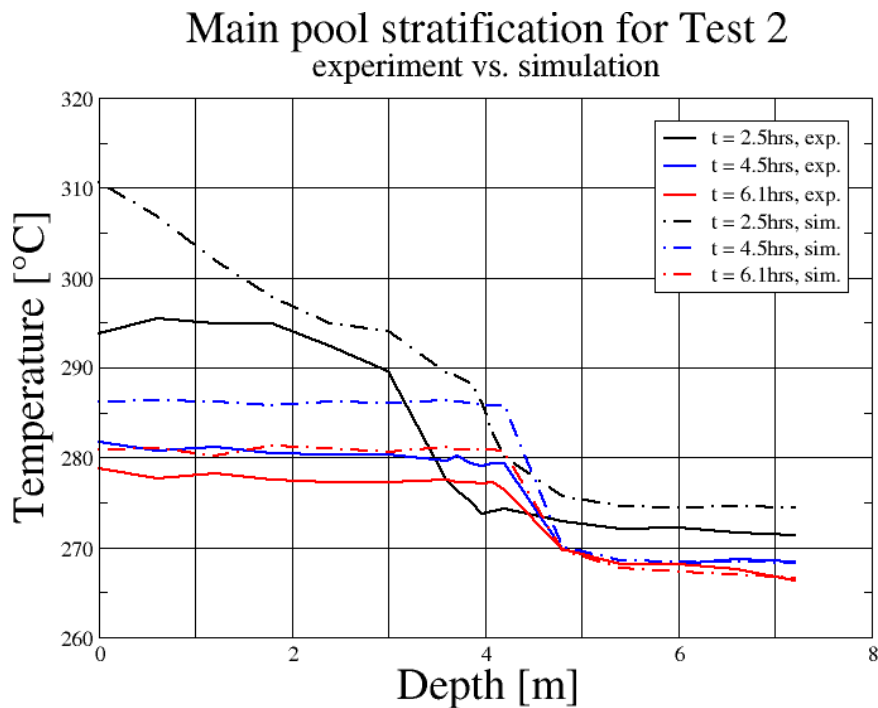


Figure 15: Comparison between the experiment and simulation of the stratification inside the main pool at three different times.

10 Conclusions of NRG part

In this report, an updated and improved version of the model discussed in SESAME deliverable D3.2, which has as purpose to numerically simulate transient experimental tests performed by ENEA with the heavy-liquid metal test facility CIRCE, is presented. Compared to that deliverable, the model has undergone some modifications, most noteworthy an improved model for the decay heat removal system and better representations of some of the heat losses in the system.

The improved model, as well as the initial model, have also been used to simulate transient test 2, which is a Protected Loss Of Heat sink and Loss Of Flow accident scenario. Results of both simulations are compared to each other as well as to the experimental test. Results using the improved model agree consistently much better with the experimental ones than the initial model does, in particular stratifications during the steady state part and transient part of the test match better, the mass flow rate of the model agrees better with the experiments and temperatures don't show a steady decrease any longer.

Overall, the model is clearly improved, giving satisfying result.

11 Introduction of CRS4 part

In the deliverable D3.2: “CIRCE experiment pre-test, data set and analysis”, the experimental data obtained in the frame of the EU project SESAME WP3 on the CIRCE large pool experimental facility of ENEA has been reported. Moreover, CFD models of CIRCE have been build, both by CRS4 and NRG, to help understand the effective behaviour of the experimental facility and highlight possible improvement. The more advanced models have been used to reproduce numerically parts of the experimental campaign.

A confront between the experimental data and the numerical results has already been performed, both for steady-state (CRS4 and NRG) and for a transient from forced flow to buoyancy driven flow condition (NRG). The numerical models are able to capture qualitatively the general behaviour of the flow velocity and temperature, both for the initial steady-state and the initial part of the transient, while the transient asymptotic behaviour showed some large discrepancies.

Quantitatively, even the initial steady-state was not satisfactorily reproduced numerically, mainly with regards to the thermal stratification in the upper 3m of the LBE plenum. Conversely, the lower 3m of the LBE plenum temperature was quite satisfactory. This is not so surprising for two reasons: (i) the models were calibrated to give the correct temperature at the Fuel Pin Simulator (FPS) inlet and (ii) the temperature field in the plenum lower half is driven by the turbulent diffusion of a convected flow and while in the upper part the LBE is mainly a stagnant pool much more sensitive to small errors in the evaluation of the conjugate heat transfer from the structures.

In the CRS4 model, the plenum vertical temperature profile is much less stiff than in the experiment, with a much lower top temperature in the plenum, indicating an apparent global flaw in the estimation of the heat transfer mechanism.

Conversely, in the NRG model, the top plenum stratification is stiffer and shorter than the experimental one. The pool temperature at the top of the riser is higher, however, it decreases much faster towards the bottom, showing here again but in a different way, an issue in the estimation of the heat transfer mechanism.

In a preliminary analysis, the main cause of discrepancy was attributed to a possible small leak at the top of the riser, at the interface with the flow separator or, with a similar effect, a non-negligible splashing of LBE at the separator free surface making droplets of LBE jump above the flow separator lateral wall. Both phenomena are not mutually exclusive and would give an added contribution.

This possible explanation would be convenient to justify the discrepancies of the CRS4 model but not of the NRG one. In any case, the possibility has been taken into account and counter measures have been taken to avoid any such leakage or splashing in the subsequent experimental campaigns, starting from the one foreseen in the MYRTE H2020 project, aimed at testing a different heat-exchanger.

The present document illustrates the attempt to understand and fill at least partially the gap between the experimental and the numerical results. The conviction behind this approach is that there are still relevant discrepancies between the experimental setting and the numerical setting. Only once these discrepancies have been removed, will it be possible to make an evaluation of the intrinsic defect of the turbulence models.

In this spirit, several complementary approach have been pursued. All are restricted to the steady-state reproducibility.

First, taking profit of the existing aggregation of results given in D3.2, we can look at the goodness of a pre-existing steady-state configuration of the experimental setup which we can confront with. We will show that there is some relevant deviations from this state and will try to quantify them.

Second, a separate set of simulation and analysis of the ICE heat exchanger is performed independently (in vitro), simulating several levels of approximation and evaluating their consequences. At this occasion, numerical thermo-couples (TCs) are positioned carefully in correspondence with the experimental ones to allow a point-wise comparison and to check the consistency between the TCs temperature mean and the flow temperature mean. An attempt to find an acceptable compromise allowing to capture what we consider the relevant flow features at an affordable computational cost is analysed.

Third, a variant of the CFD model will be used to evaluate qualitatively a series of possible cause of discrepancies. The conjugate heat transfer can be locally hindered by fooling due to the creation of some low

conductivity oxide layer on some wall. Splashing and bypass flows can be represented by localised mass-energy sink-source terms. The heat source distribution in the FPS is made uneven and keep some distance to the wall, making it much colder and transferring much less heat. A similar procedure is applied to the SGE. Forth, an entirely new CFD model is built, with several improved features, mainly with regards to the modularity of the different components. Most important is that the new model can (but is not forced to) simulate a controlled flow leak at the top of the riser. Another important feature is that the model can be run both in VoF and single phase configuration, with the intent to use it almost exclusively in single phase, allowing a much faster convergence toward a reasonable steady-state. The improvement of the model is explained and further simulation and analysis are performed, also taking into account the consideration arising from the second point.

12 The experimental deviation from steady-state

In the experimental campaign performed in the framework of the SESAME project and described in the D3.2, each test case starts with an attempt to reach a “hot” reasonably steady-state at different FPS powers and similar mass flow rates, starting from the LBE inventory in stagnant condition and kept warm by electrically heating the main vessel walls. This heating is shut down when starting the test.

The flow circulation is driven by injecting pressurized argon at the bottom of the riser. The LBE heating comes from the electrical power dissipating by Joule effect, mainly in the FPS but also to some extent all along the pins at the flow conveyor level and in the wires inside the Dead volume. Cooling is mainly achieved thanks to the ICE heat exchanger working with low pressure boiling water injected at constant flow rate. A secondary heat loss comes from CHT to the external vessel, to the vessel cover and to the dead volume. A tertiary heat loss comes the Argon heating.

The LBE mass flow rate is mainly controlled by the level of pressure maintained on top of the argon injection line. It is slightly dependent on the LBE temperature at a given Argon Normal litter flow rate. In effect, the gas lift depends primarily on the void fraction which increases with temperature. The effect is however seemingly quite irrelevant because the LBE mass flow rate at the FPS inlet settles very soon around a stable mean value, while the thermal field still develops for several hours. The pressure imposed to the Argon line to get approximately the desired flow rate comes from previous experience and calibration.

While the heating is controlled and is essentially constant, the cooling is only partially controlled. The ICE heat exchanger should cool better with hotter LBE, as we have a constant water flow rate and inlet temperature. The pressure drop is almost proportional to the (square of the) steam produced and flowing in the HX upper part. And indeed, the pressure drop show an increase of 0.5 bar from 2.4 to 2.9 bar-g during the [8 ; 10] h interval. A 20% increase should correspond to a 10% additional boiling and about the same increase of exchanged heat. But there is evidence from the plenum temperature evolution that the cooling remains globally rather constant, for yet non-obvious reason. In consequence, it is quite difficult to guess a priori at what temperature we can hope to reach an equilibrium between heating and cooling.

In Figure 8 left, we reproduce the thermal history of the vertical Line A TCs which is quite representative of the other lines. The position of the lines is indicated on the right, same figure. There are several features that are apparent in the figure. We discard the first hour as it deals with the transition from stagnant to forced convection flow with both FPS heating and ICE cooling. Looking at the four upper TCs, we see an almost constant temperature during the time interval [1; 5]h. After what, the temperatures steadily increase, initially with a slower slope, then from 8 to 10 h with a stronger slope, seemingly constant. The temperature of the other TCs, located below, show a different behavior, initially decreasing then apparently constant, but after a while increasing again, with an increasing slope that seems to remain constant during the last two hours from 8 to 10h.

Based on these considerations, it seems that the LBE is globally cooling during the interval [1; 5]h then starts heating, reaching a rather constant heating rate during the interval [8 ; 10]h. A possible explanation for the first phase is that additional cooling comes from heat exchange with the structures, mainly in the upper part, comprising the cover. Once the cover is heated, the additional cooling vanishes, and remains an imbalance between the FPS heating and the ICE cooling. For some reason, this imbalance does not significantly reduces while the LBE gets hotter, at least during the [8 ; 10]h interval.

A rough quantitative evaluation of the thermal imbalance during the interval [8 ; 10]h can be performed. The global thermal inertia of the CIRCE numerical model is 13.2 MJ/K. Observing a global temperature rise of 13 K (mean over A-line TCs), the corresponding heat content increase is 172 MJ, leading to a thermal imbalance about 24 kW.

Turning back to Figure 8, we can also see that the upper and lower TC temperatures show a very smooth time behavior. On the contrary, some of the intermediate TC temperatures exhibit a quite strong noisy signal. In Figure 9, we reproduce the TCs temperature on a vertical height basis, after 5.6h, extracted from a former test series with a very similar initialization. In fact, in Figure 10, we also reproduce results of the pre-test simulations of CRS4 and NRG aimed at reproducing a steady-state with a temperature field consistent with

the one of Figure 9. The noisy temperature signal of Figure 8 corresponds to the TCs located in the region of strong vertical gradient at about 4m depth.

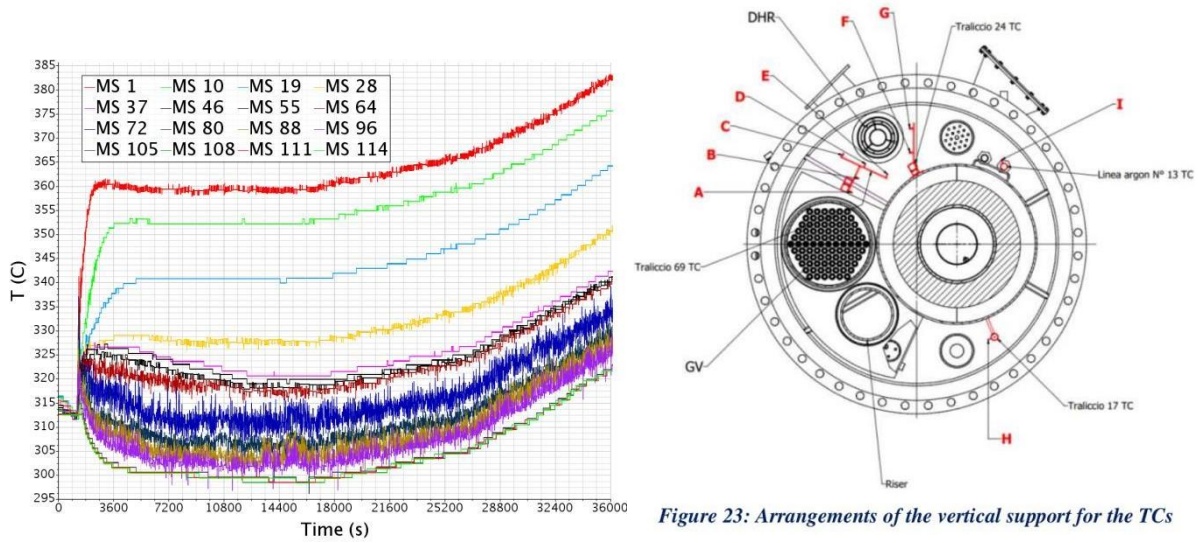


Figure 23: Arrangements of the vertical support for the TCs

Figure 8: left. Test 1 linea A history of the TCs temperatures as typical thermal transient behavior; right. position of the vertical lines of TCs.

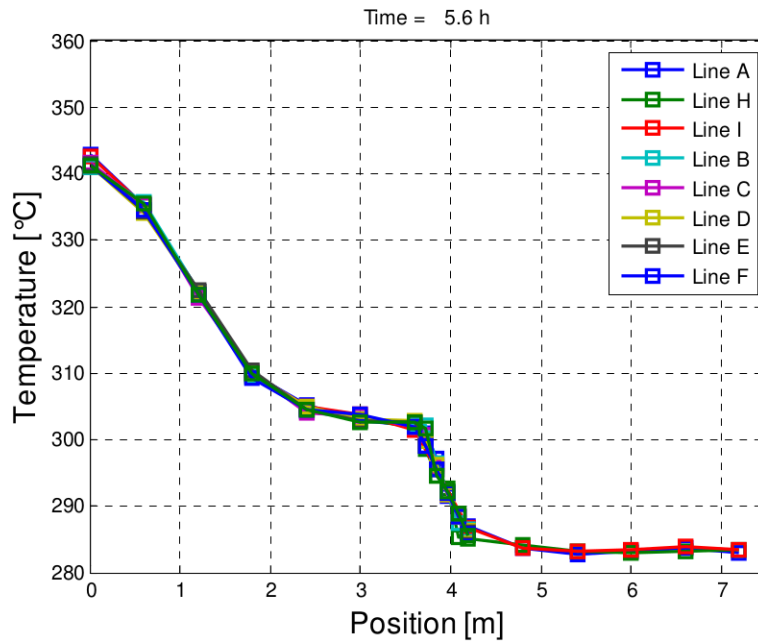


Figure 54: LBE temperature inside the pool at $t = 5.6$ h

Figure 9: reference experimental “steady-state” temperature used for numerical comparison.

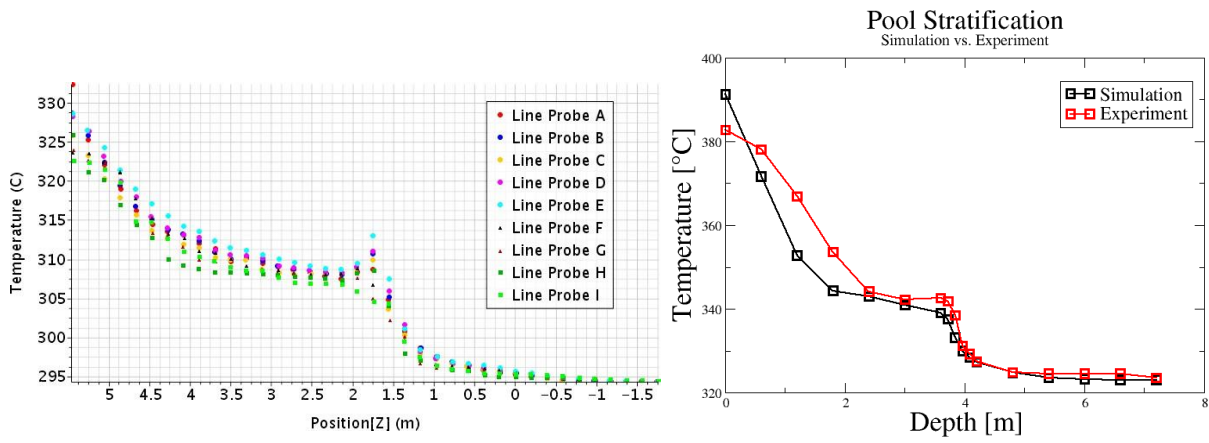


Figure 10: numerical steady-states obtained by CRS4 (left) and NRG (right)

13 Multi-scale analysis of the ICE heat exchanger

The objective of the analysis is to check the quality of the ICE HX numerical modeling of low level by performing an higher level of modeling and check the discrepancies. The ICE numerical HX is simulated inside a numerical domain with inlet and outlet extensions that are indicative of the CIRCE environment.

1.1 Geometry

The geometry used to make a more accurate model of the ICE HX is shown in Figure 11. As shown on the right side, we have made use of the symmetry and modeled only half HX. The LBE enters the domain rising vertically like in CIRCE and enters a flow separator region sized has a symmetrized version of the CIRCE separator. A numerical outlet region is added with the objective to get closer to the CIRCE configuration and to not arbitrarily constrain the shape of the outlet flow.

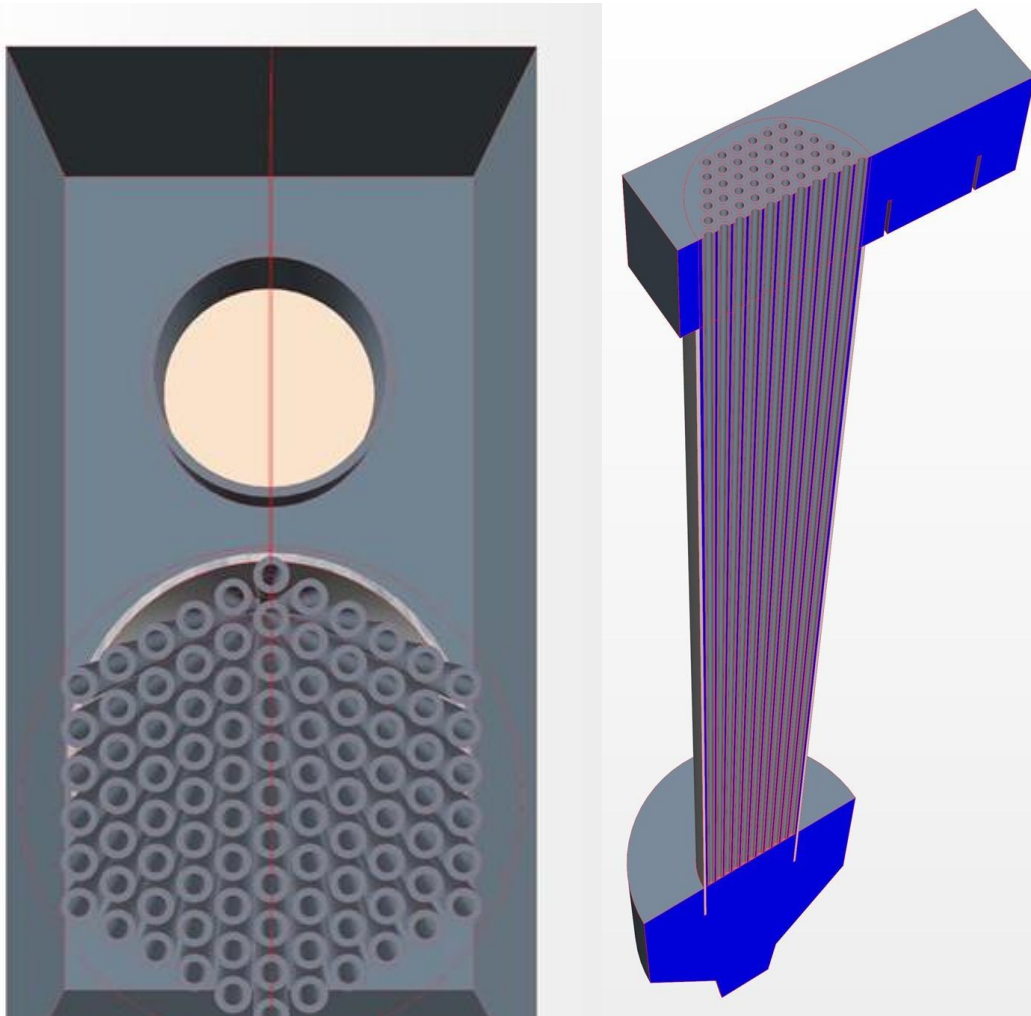


Figure 11: geometrical domain. Left. top view. Right. Top-side view.

1.2 Setting and instrumentation

The simulation is performed within the single phase steady-state framework. There is no Argon phase. The LBE is buoyant.

A vertical mass flow rate of 55 kg/s at 355 C is set in inlet. The external boundaries are adiabatic. The super-heated water is not simulated. Instead, a vertical profile of temperature is forced at the inner boundary of the HX tubes. The profile follows approximately the water profile taking into account a pressure dependent temperature of vaporisation and is fitted to be reasonably consistent with the heat exchanged along the vertical. This can be seen on Figure 12. A marginal variation of the vertical profile is also implemented on a ring basis.

The outlet grid of the HX, shown in Figure 13 is modelled with a homogeneous porous baffle considering it as an orifice for the setting of the inertial resistance coefficient (0.51 in the solver)..

Numerical thermo-couples have been positioned in coincidence with the CIRCE setting, both at the inlet and outlet of the HX. Their exact position is shown in the result section.

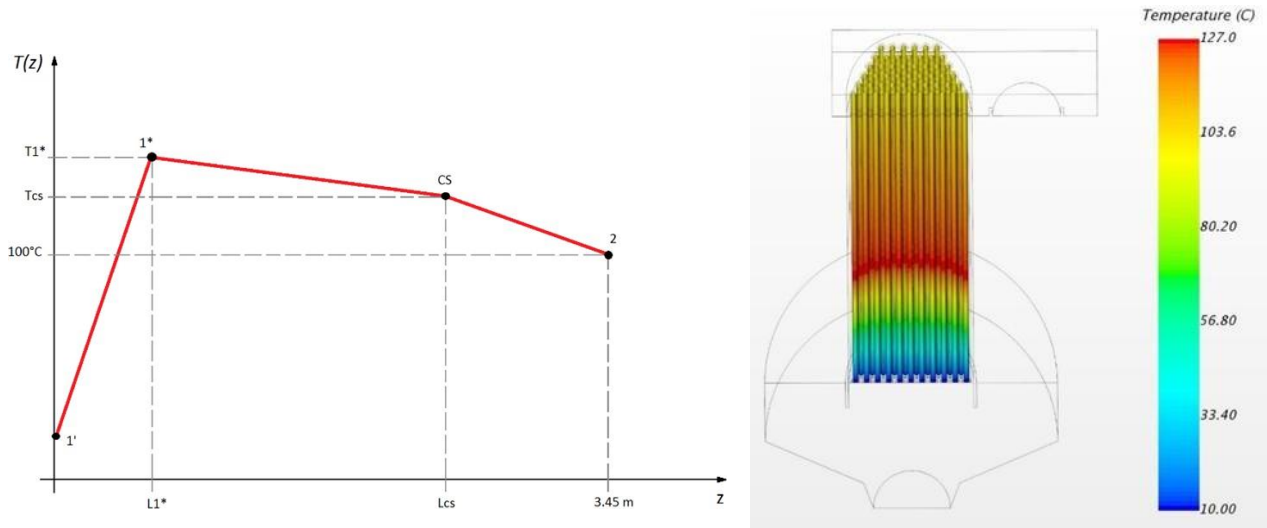


Figure 12: Temperature profile imposed at the internal wall of the HX tubes.

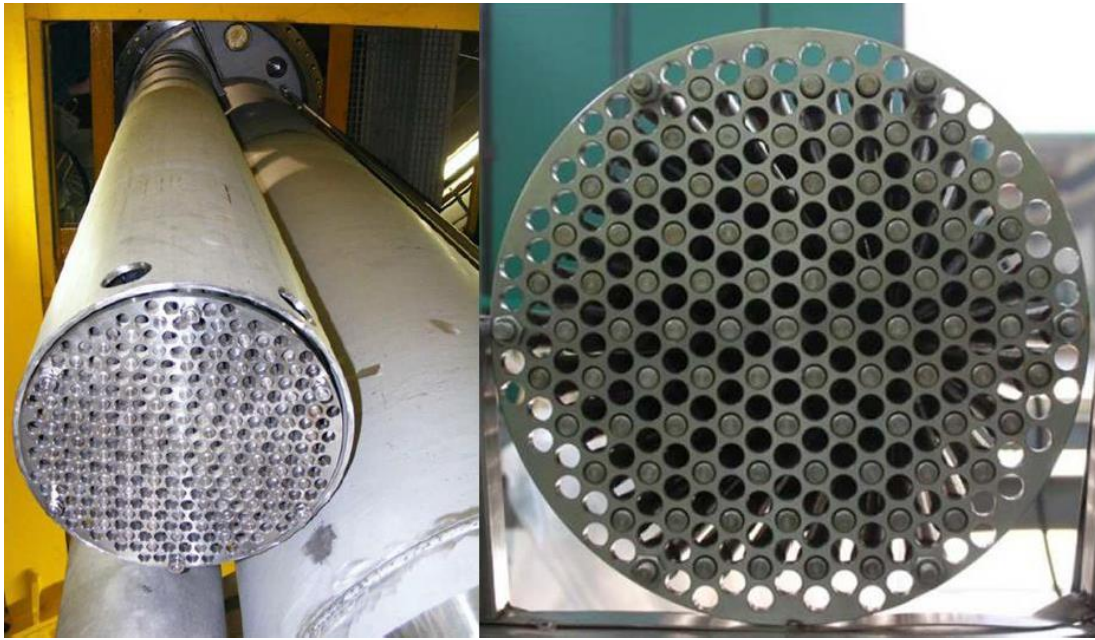


Figure 13: outlet grid of the CIRCE-ICE heat exchanger.

1.3 Results and analysis

The LBE temperature profile is shown in Figure 14 on several horizontal and one chosen vertical sections. The straightforward information readily available from these plots is the large temperature inhomogeneity within all horizontal sections. The LBE is much colder at the HX centre than at its periphery. This homogeneity can be better understood by looking also at vertical density and velocity profiles, given in Figure 15. In effect the vertical velocity (downward) profile indicates higher values near the centre and an almost stagnant region at the periphery. With good confidence, we can infer that we are in presence of a strong (and unexpected) buoyancy effect.

A direct consequence of the buoyancy driven temperature field perturbation is that the external wall temperature is much hotter than expected and in any case much hotter than the almost horizontally homogeneous profile obtained in the pre-test simulation. Because the thermal stratification in the upper part of the bulk seems largely controlled by the contact with the HX guide tube, we have another good candidate, besides the possible leak, to explain the upper plenum temperature profile discrepancy.

Other considerations regards the information coming from the TCs. The temperature field corresponding to the HX inlet TCs is shown on Figure 16 and to the HX outlet TCs on Figure 17. The HX inlet TCs show numerically a mean temperature of 354.5 C, only 0.5 K below the riser inlet temperature. This confirms that these TCs could be a good indicator of the flow entering the HX, even if they are located several cm below the top of the active part. However, being close to the wall, the effective temperatures could be altered by the presence of a colder LBE plenum on the other side of the wall.

With regards to the TCs located at the bottom of the HX, the situation is quite more complex. From one hand, we have measured the mean temperature on the 6 TCs, giving 256.5 C. From the other hand we have measured the flow averaged mean temperature on the HX section which is the only temperature relevant for the HX thermal worth, and it comes 262.3 C. The 6 K difference corresponds to an overestimation by about 42 kW of the HX power. While we do not pretend to have a large confidence in the simulation results in this particular region, we are instead quite confident to state that the temperature given by the mean on the TCs is very loosely representative on the mean flow averaged temperature.

With this consideration in mind, we look more carefully at all the temperature related to the SG in our experimental test case of reference (test 1). In Figure 18, we show the recorded temperatures at the three TCs located at the SG inlet. The three temperatures are quite homogeneous, oscillating in an interval about

5K and slowly evolving in time. There is an unknown event lasting about 1h during the interval [7 ; 8]h slightly lowering the TSG03 temperature and then rising again to become the hottest one. The reason is unknown but is consistent with a reorganisation of the flow in the upper part of the SG.

With regard to the SG exit, the temperature and location of the six TCs is given in Figure 19. We can see a consistent variability, the temperatures spanning a typically a range of 40K ([265 ; 305]K at time 5h). The TSG17 gives generally the hottest temperature and the TSG18 the lowest one with a typical difference about 25K. The temperature plot is however a little confusing, so we have added, in Figure 20, a plot of the TC temperatures with an incremental offset of 30K to separate the ranges and illustrate the differences in oscillation amplitude among the TCs. We also plot the values on a much smaller 5min interval where we can see occasional oscillation up to 30s in a few seconds, mainly on TSG18, but no apparent correlation between the TC temperatures variation. The global picture with offset puts in evidence a large and long thermal event during interval [1.5 ; 5]h involving in a strong correlated way TSG14, TSG15 and TSG16, while not influencing the three other TCs. A similar but smaller event seems to happen in the time laps [7.5 ; 9]h. There is also a sudden jump of temperature for TSG13 about time 8.30h

This suggests that the SG outlet flow is far from trivial and subject to bifurcations at all time and space available scales.

To complete the SG picture, we also plot the nine sub-channel TC temperatures captured slightly above the bottom grid. These are plotted in Figure 21 together with their relative position. The colours have been set to highlight the distance from the SG axis. Central TCs are plotted in green and intermediary in blue tones. We can see that all the temperatures are usually very stable, only slowly evolving on large time scales. However, there is a very high dispersion of the values, about 130K. The central TCs give similar temperatures about 190C. This is not seen at the SG outlet where the minimum registered temperature is above 260C. Two of the intermediary radius TCs show values about 225C and two TCs with the larger radius give about 270C. There are two TCs giving much higher value, (i) TSG04 with intermediary radius and temperature about 285C and (ii) TSG07 giving a very high unexpected value about 310C. We can note also three sudden temperature rises in the range 5-10K, (i) at TSG09 time 6h, (ii) at TSG06 time 8h30 and (iii) at TSG08 time 9h.

Turning back to the 310C measured on TSG07, and without any evidence that the TC is damaged, we can observe that this temperature is typical of the one present in the bulk around the SG outlet height. This suggests that a coherent flow is entering the SG from below, essentially avoiding the outlet TCs except marginally TSG13 a few degrees below (305C). This hypothesis is however quite inconsistent with the quite chaotic flow behaviour observed below the SGE lower grid, so that LBE coming from below is most probably recirculating below the SGE bottom grid.

If some hotter LBE enters the SG outlet from the bottom, this should lead to an overestimation of the SG outlet temperature and thus an underestimation of the SG power. Moreover, the low temperature flow around the three central SG TCs are not seen by the SG outlet TCs, also leading to SG power underestimation. In addition, there is still an unknown heat flux from the SG mantel not accounted for.

All in all, all what we can say is that we should be very cautious in interpreting the experimental SG outlet temperature and most of all, we have very strong uncertainties on the SG power which at this point can come only from global balance considerations. Nonetheless, we plot in Figure 22 the difference between the mean temperature in inlet and outlet of the SG, averaged on 60s for better readability.

To add to confusion, we plot in Figure 23, the water mass flow rate which look quite constant on short-time mean, and the water inlet pressure, increasing by 1.2 Bar in 10h from 1.7 Bar to 2.9 Bar. We expect the pressure increase to correspond to a heat exchange increase and a higher rate of vaporisation. And this would be consistent with the global increase of LBE temperature. However, there is no reduction in time of the LBE temperature increase, mainly in the last 4 hours. Another possible explanation would be a fouling of the SG on the water side. But the water inlet pressure and flow rate of the successive experimental test contradict this hypothesis. A more consistent but incomplete explanation would be that the SG tubes can work at different flow rates, still maintaining an equal pressure drop. This is because in first analysis the pressure drop is proportional both to the local water inlet mass flow rate and to the local outlet vapour flow rate. That is, a lower water mass flow rate can be compensated by a higher steam mass flow. Due to progressive fouling on the LBE side and/or to the LBE temperature increase, the dispersion between the single tube flow rate can increase and lead to a global higher pressure drop, apparently without increase of the global heat exchange..

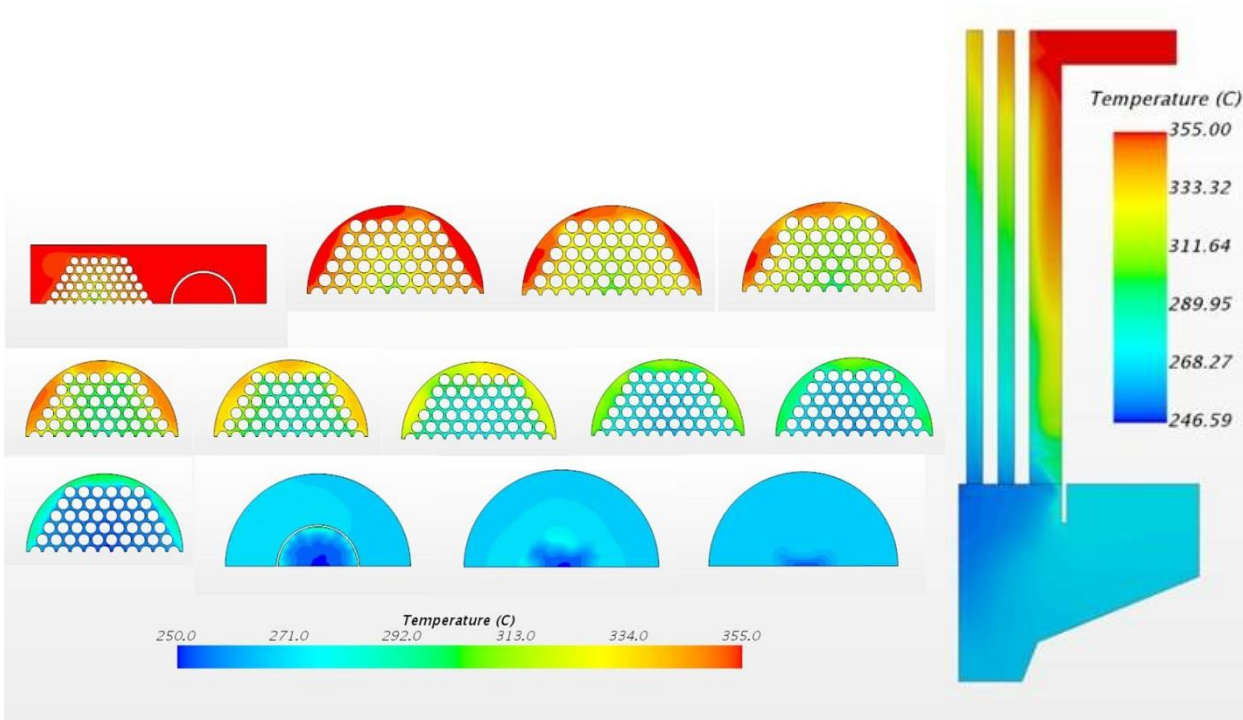


Figure 14: temperature profile. Right, series of horizontal section. Left, chosen vertical section.

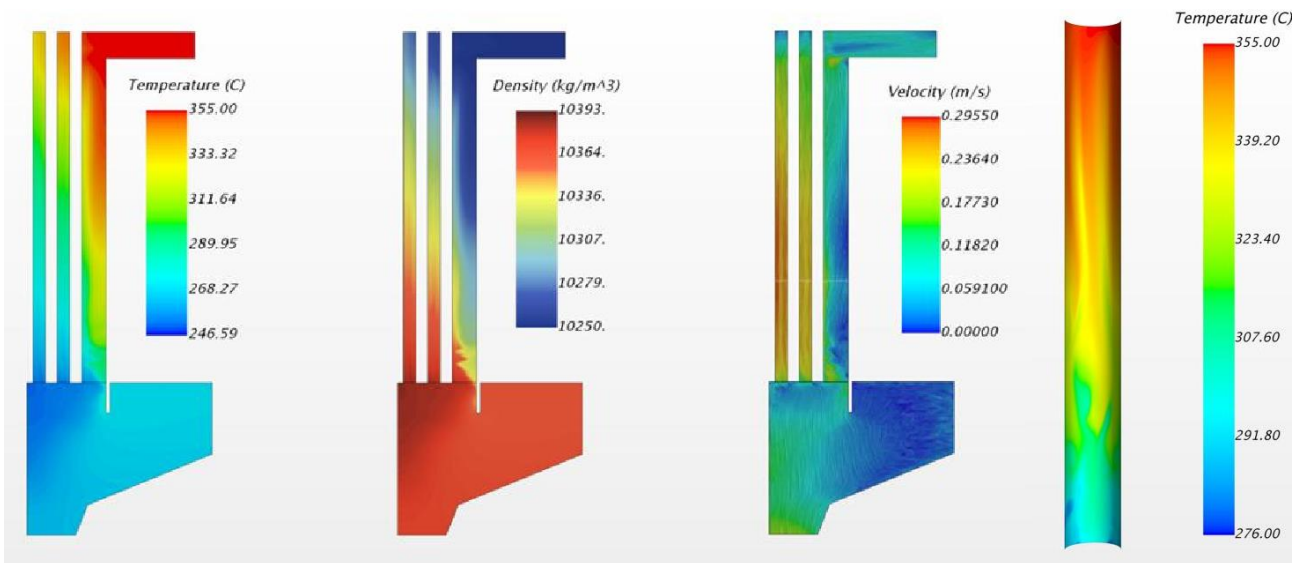


Figure 15: Chosen vertical sections. Left, temperature, density and velocity profiles. Right, HX wall.

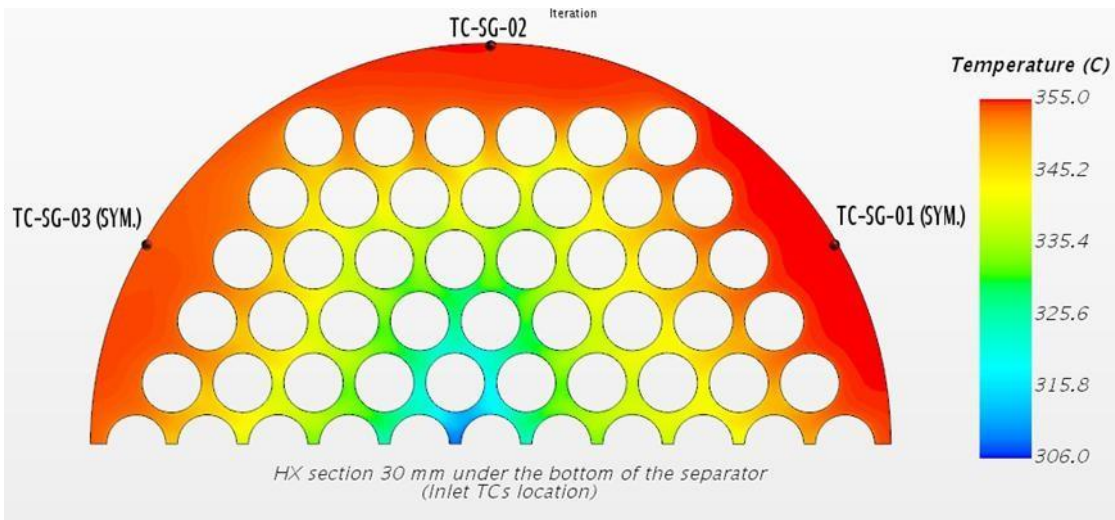


Figure 16: HX upper part. Horizontal section passing through the TCs. LBE temperature field.

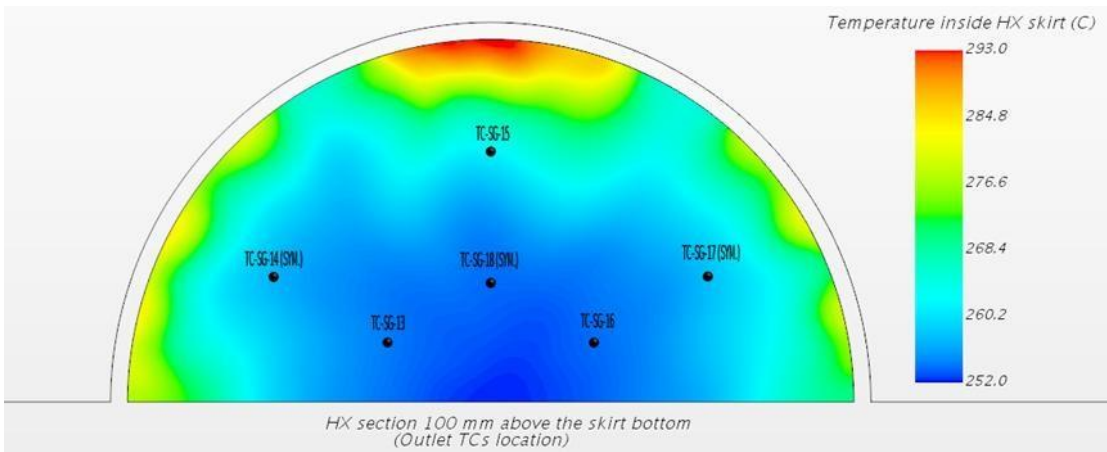


Figure 17: HX outlet section with the TCs location.

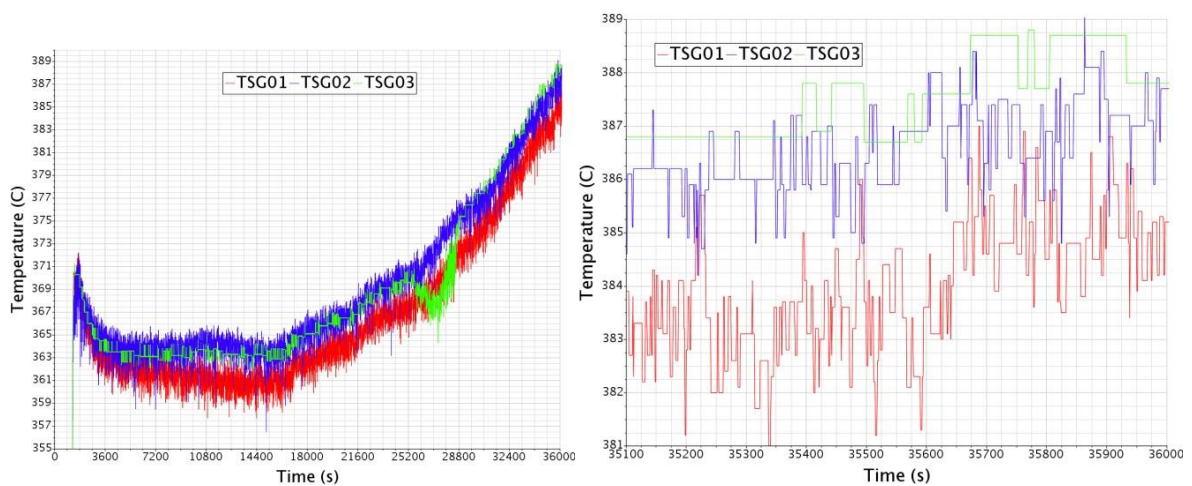


Figure 18: Test case 1. TC temperature at the SG inlet. Left: first 10h. Right range [9.45 : 10]h.

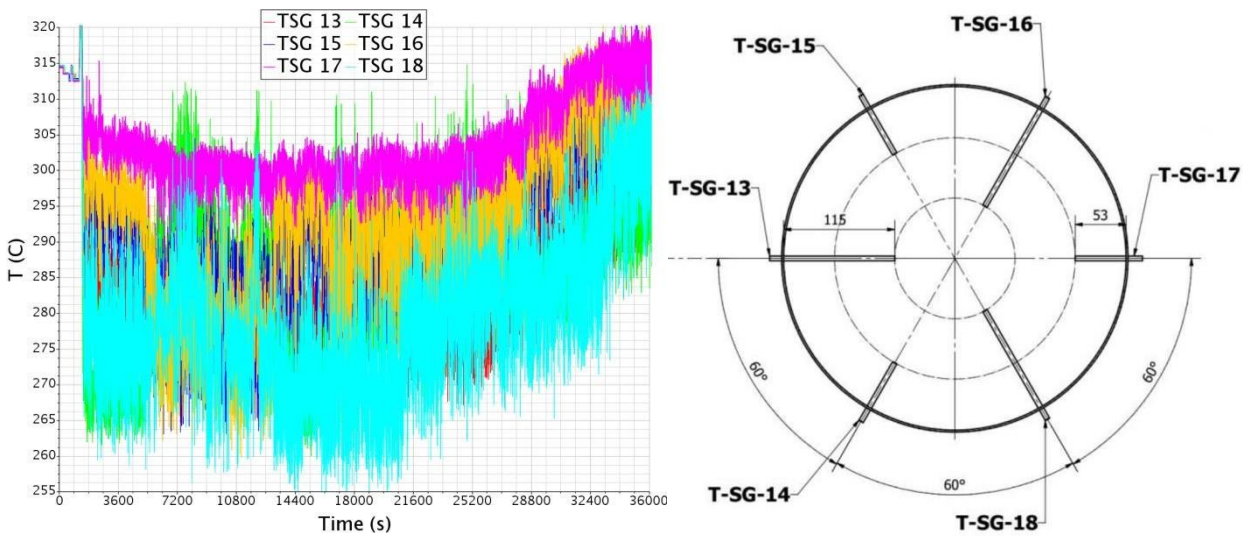


Figure 19: Test case 1. Left, temperature at the six SG outlet on a 10h time interval [0 : 10]h. Right: horizontal position of the TCs.

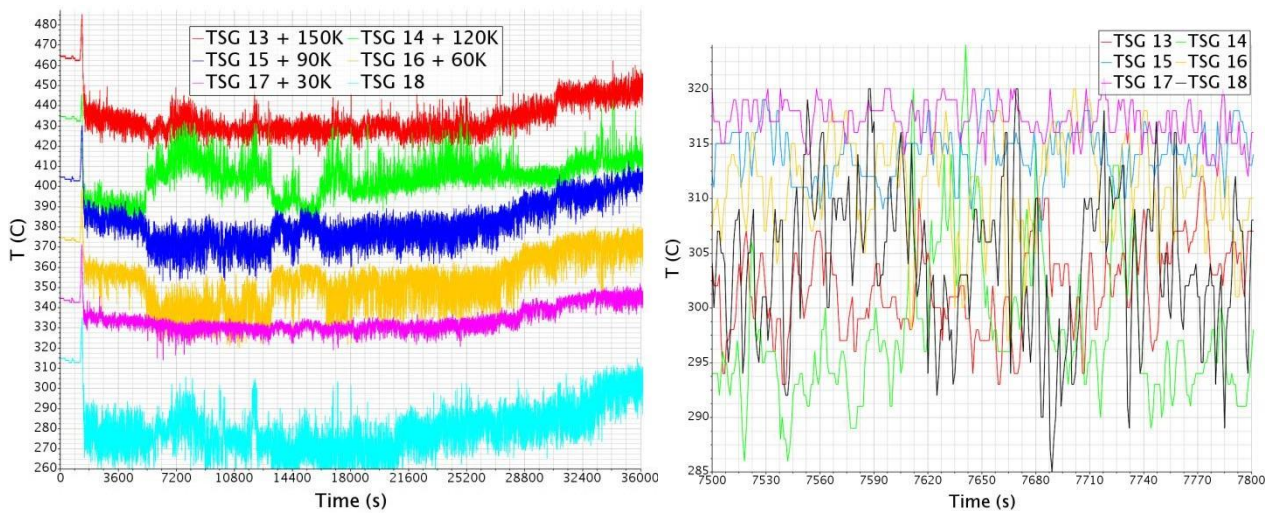


Figure 20: outlet TCs temperature. Left, with incremental offset of 30K. Right, on a 5min interval.

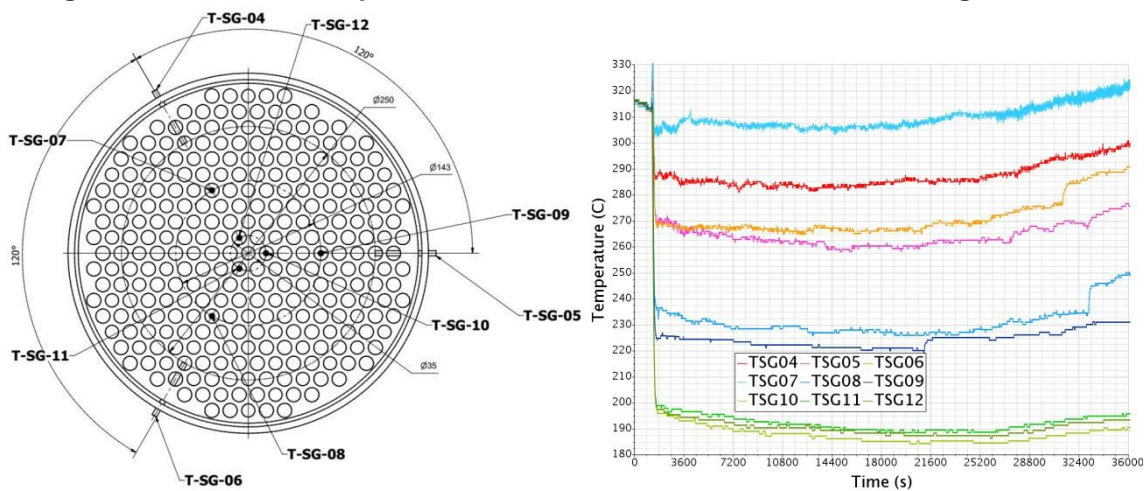


Figure 21: Test case1. Left, position of the TCs above the SG bottom grid. Right, temperatures.

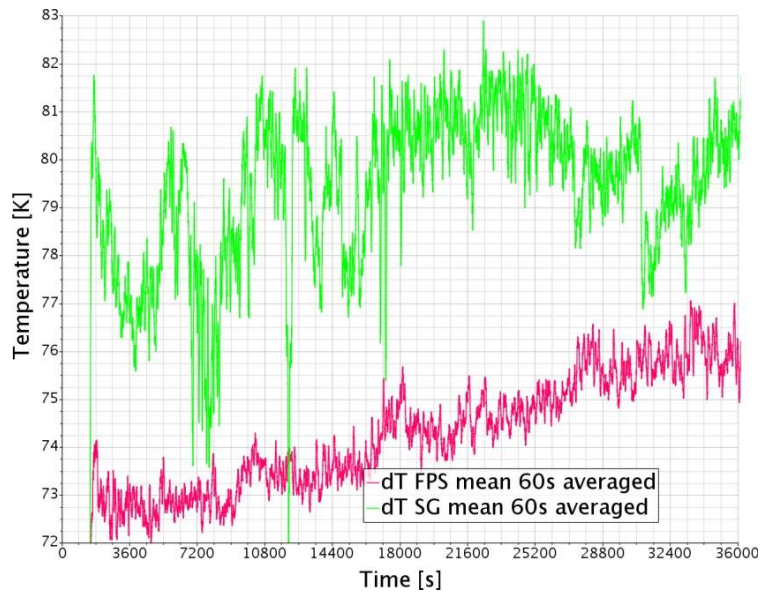


Figure 22: Test case1. Temperature variation between the SG and FPS means on the TCs in inlet and in outlet. averaged on 60s.

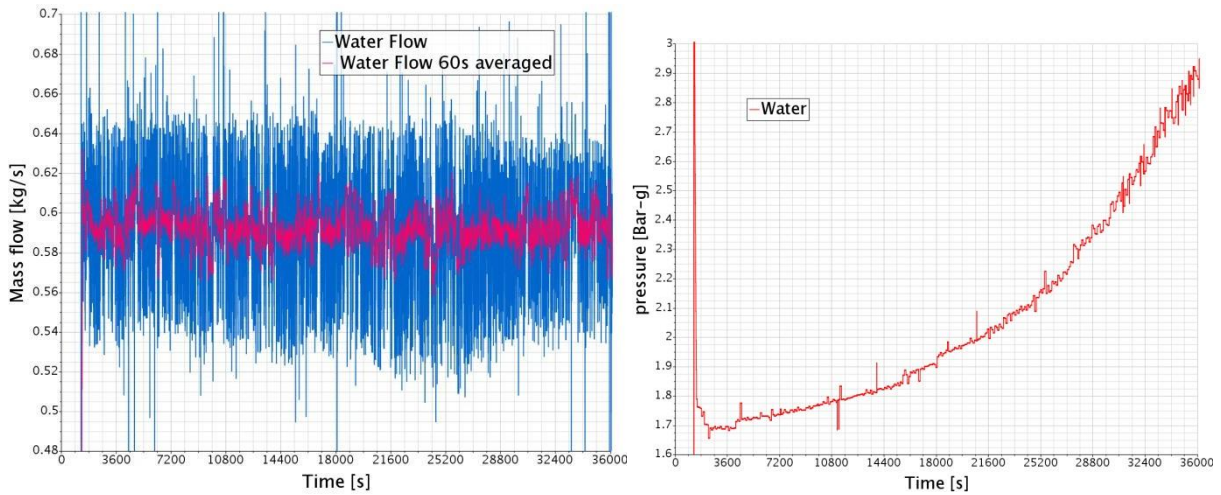


Figure 23: test case 1. Left. water mass flow. Right. Feedwater pressure.

14 More on the FPS heat balance

We now turn our attention to the FPS global thermal balance. Our objective is to get confidence on the experimental pointwise results with regards to their interpretation in terms of mean flux and for sound comparison with numerical results.

The FPS balance comes from the electric power released in the active part as thermal energy by Joule effect and mainly convected out by the LBE flow while a residual part of the heat is lost by conduction through the wrapper wall. The temperature excursion is therefore mainly controlled by the ration of electrical power to LBE mass flow rate.

In Figure 24, we show on the left the first 10h history of the electric power feeding the FPS ; while on the right, we show the pressure drop across the Venturi flow meter. Also 60s averaged values are plotted to filter the high frequency variations. For the Venturi, it has also been necessary to average over 10 minutes to start to capture the curve large scale tendency. We can see that the initial power lies about 795 kW at start and increases up to 815 kW with some occurrence of bi-stable values with 7 kW differences. The 20 kW increase (2.5%) comes from a gradual increase and one main jump at about 5h. Locally, the power remains in a 2kW interval (0.25%). The Venturi pressure drop show large high frequency oscillations, with value essentially maintained in the [315 ; 375] mBar range (~17%). Filtering at 60s still gives a noisy signal, while filtering at 10 minutes gives large scale irregular oscillations of 10 mBar. There is a small mean decrease during the last two hours, representative of a mass flow decrease no more than 1 or 2%.

The history of the temperature in inlet and outlet of the FPS active part, together with the position of the TCs in shown respectively in Figure 26 and Figure 27. The inlet temperatures are very homogeneous. This is not surprising considering that the LBE comes from the lower bulk region which is also at a very homogeneous temperature. The mean over the 3 TCs is therefore very significant and its 60s averaging almost completely covers the mean value.

The FPS inlet temperature is an excellent fixed point for a confront with numerical simulations. However for the 2K of FPS33 over the two other TCs, we can state a confidence interval of at least 1 or 2K.

The situation is quite different for the FPS active zone outlet. The dispersion between the hotter and colder value is about 35K, that is, more than 40% of the expected temperature rise.

There is now way to infer what could be reasonable weights to give to the TC values to generate a sound mean. And these 3 TCs are useless to define a sound mean flow temperature. However it should be noted that they all evolve in time at about the same path as the inlet TCs.

Fortunately, upward in the FPS, close to its outlet, we have three other TCs. The LBE from the active part has had time to mix and regularize its temperature. This is what we show on Figure 28. The local temperature excursion is contained in a 6k interval (4.5%), which can be related to the high frequency pulsation of the flow rate. There is no apparent difference in short time average between the TCs. Their mean has a reduced oscillation and the 60s average of the mean remains inside a 1K interval.

The temperature of the 60s average of the 3 TCs mean seems an excellent reference data for global balance consideration and for confront with numerical simulation. The only issue is that the exact position of the TCs is unknown.

Having at hand a sound extracted temperature history in inlet and outlet of the FPS, we can extract the difference and confront it with the electric power and the mass flow rate. This is shown on Figure 29, left. We can see that during the 10h interval (or restricting to the interval [1 ; 9]h), the temperature difference increases by 3K (4%) from 73 to 76C. As already said, in the meantime the electric power as increased by 20 kW (2.5%) from 795 to 815 kW. The temperature as increased by about 22K and thus the Cp has decreased by about 0.3%. The remnant 1.2% can be mainly inferred to a small drop of mass flow rate, consistently with the previous discussion.

Now, we can confront the heating in the FPS with the apparent cooling in the SG. As shown in Figure 29 right, cooling seems always larger than heating, which is inconsistent with the general heating trend of the bulk during the last 5h or so. On the other hand, the temperature increase in the FPS, about 75K, with a mass flow rate about 6kg/s, as shown in Figure 25, corresponds to 718 kW. If we suppose only 750 of the

795 to 815 kW are released in the FPS, it means that the heat loss in the FPS are about 32 kW with a quite large uncertainty.

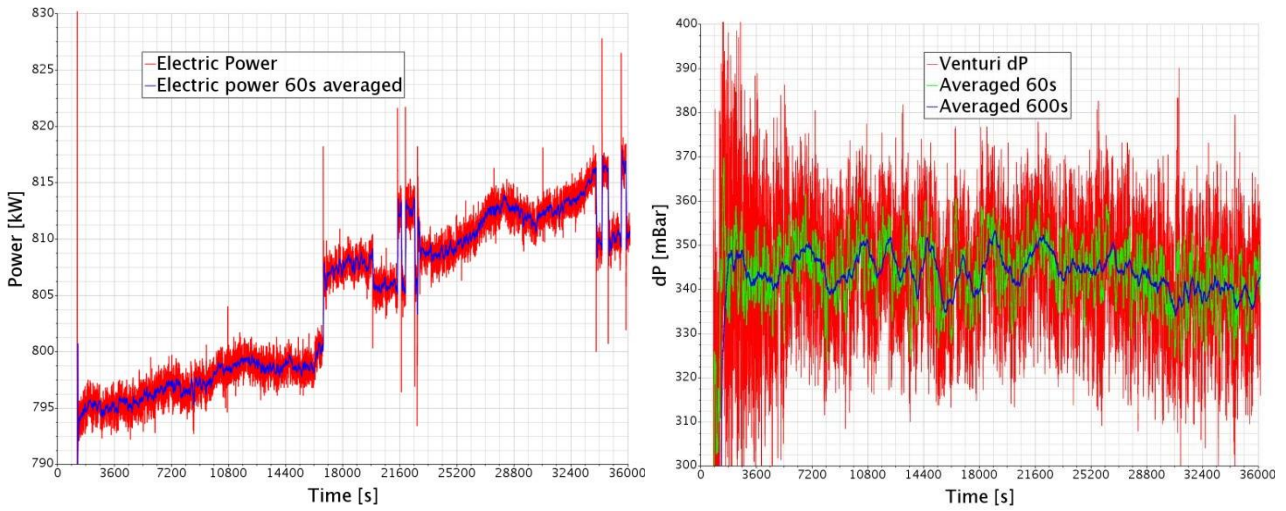


Figure 24: test case 1. Left, electric power. Right, Venturi pressure drop.

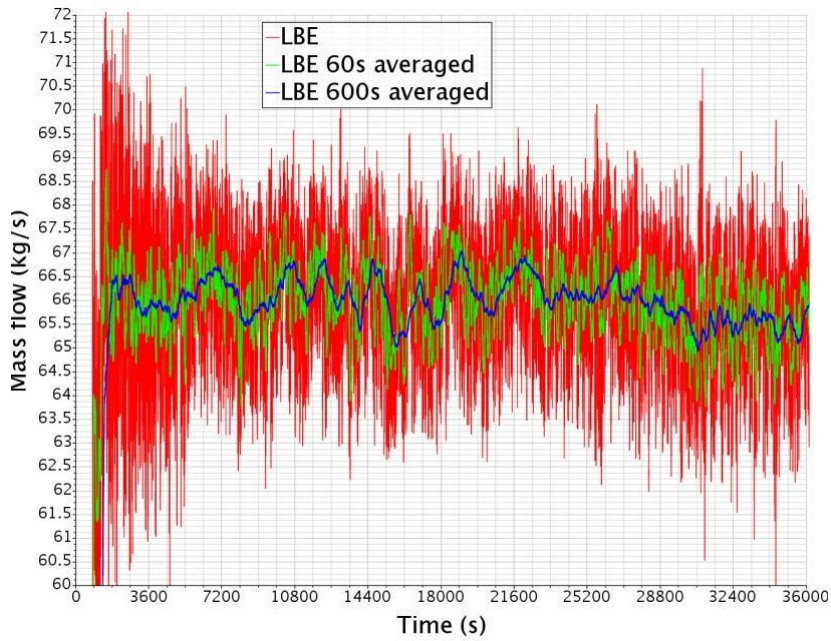


Figure 25: Test case 1. Mass flow rate at the Venturi flow meter from pressure data.

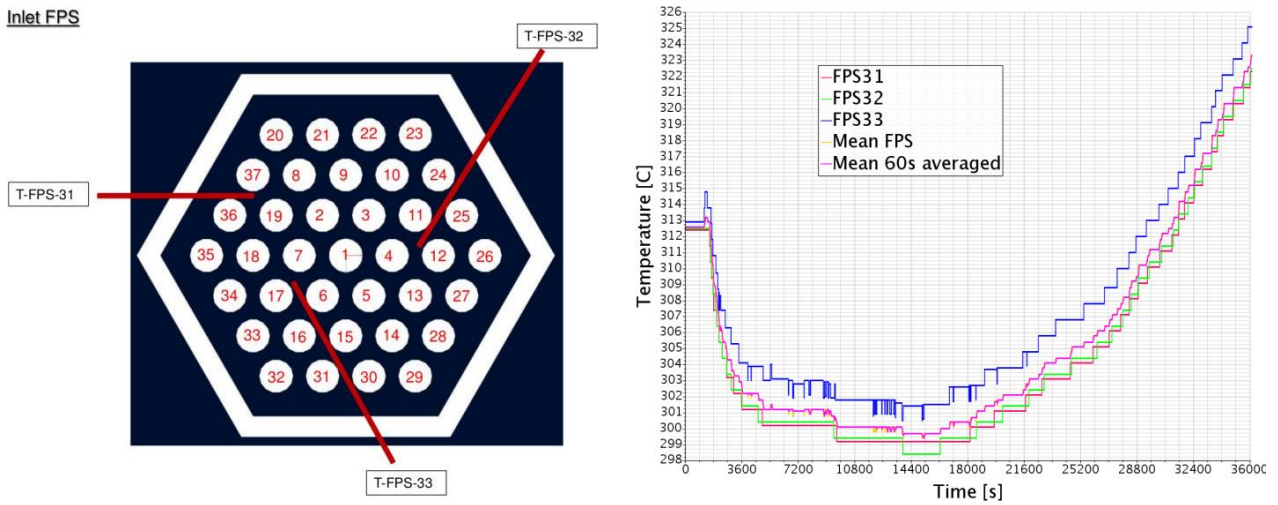


Figure 26: Test case 1. Left. horizontal position on the 3 TCs in inlet of the FPS active section. Right. corresponding 10 hours temperature history.

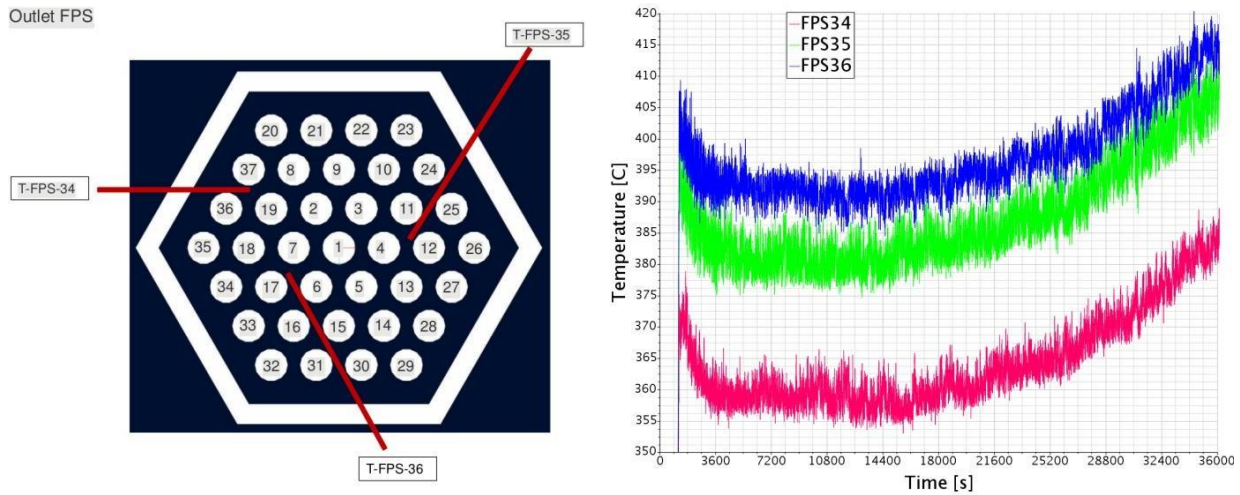


Figure 27: Test case 1. Left. horizontal position on the 3 TCs in outlet of the FPS active section. Right. corresponding 10 hours temperature history.

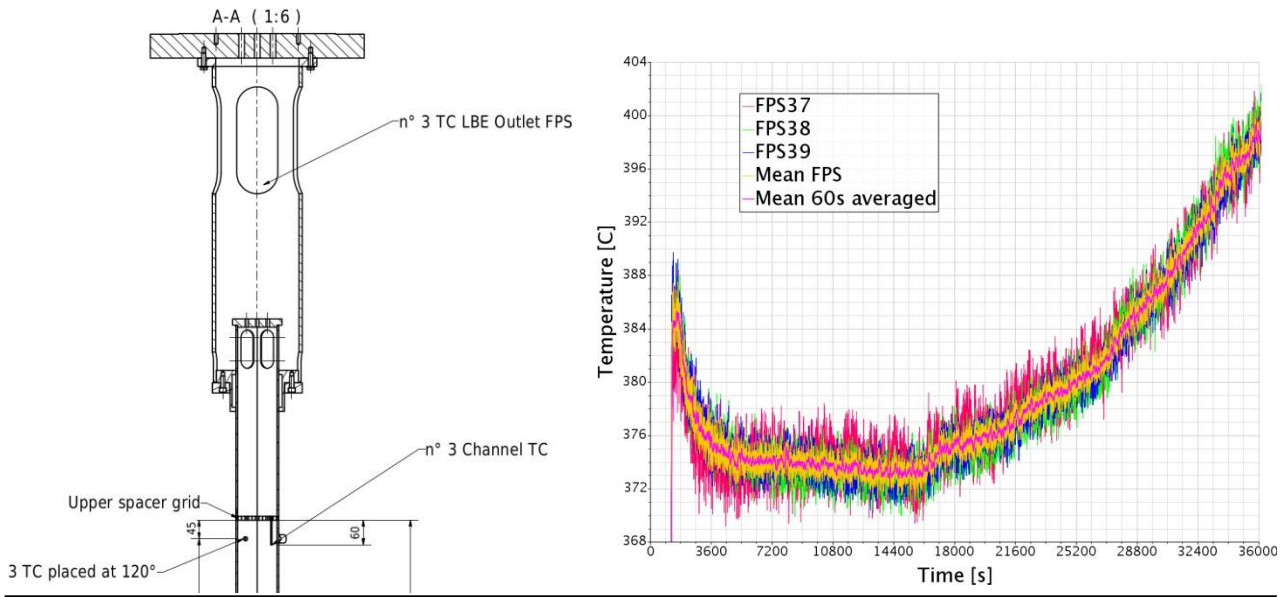


Figure 28: Test case 1. Left, vertical position of the TCs above the active part and near the outlet of the FPS. Right, 10h temperature history of the TCs located near the FPS outlet, of their mean and of a 60s average of their mean.

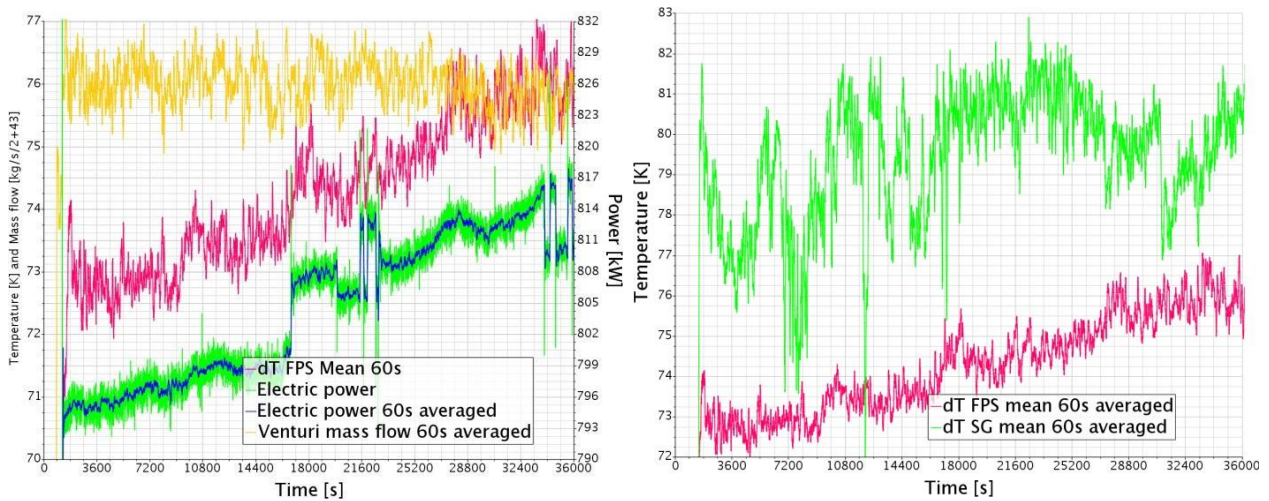


Figure 29: Left, 10h history of the temperature increase through the whole FPS, rescaled mass flow rate and electrical power. Right, confront with the temperature changes through the FPS and the SG after mean on the TCs and averaging over 60s.

15 Flow conveyor and riser

The temperature at the TCs located at the riser inlet, together with their position is shown on Figure 30. The three temperatures are almost identical during all the 10h, without oscillation. This should be an indication that the riser inlet flow is homogeneous in temperature and thus pointwise and mean flow value should coincide rather well. However, when looking at the TCs at the riser outlet, as in Figure 31, we see a much larger small time scale dispersion of the temperatures. This could be explained by the bubbly flow, but the bubbly flow is expected to improve mixing and temperature homogeneity. The registered temperature could also be influenced by the bubbles temperature, but we expect the bubbles to be rather cooler than the LBE for their initial temperature and their rapid expansion due to the drop of pressure with height. Instead, while once time averaged, two of the TCs give substantially the same temperature as in inlet, TTS04 remains a few degrees above. See Figure 32.

This can be explained by a coherent flow entering the riser at a higher temperature without getting close to the TCs. This hotter coherent flow would be somewhat dispersed by the argon injection, but not completely, thus letting occurrences of hotter plumes as registered by the riser outlet TCs. It is however not possible to quantify how much the LBE flow in the riser is hotter than the temperature registered in inlet, how much the Argon bubbles perturb the riser outlet reading and how they should be weighted. It is quite possible that the mean temperature registered at the riser outlet is still an underestimation of the outlet flow temperature. If the cover gas temperature results a good approximation of the riser outlet bubble temperature, then its value can be appreciated in Figure 34. To complicate things, the riser inlet TCs are very close to the Argon nozzle and only slightly above. The LBE flow here is strongly influenced by the argon injection, but we absolutely do not know how at the local level and comparison with the numerical temperature and velocity profile would be at best useless and at worse misleading.

We can also notice that the temperature at TCS04 is initially below the other ones and also more instable. It is only after more than two hours that it both becomes higher and more stable. Reason is unknown.

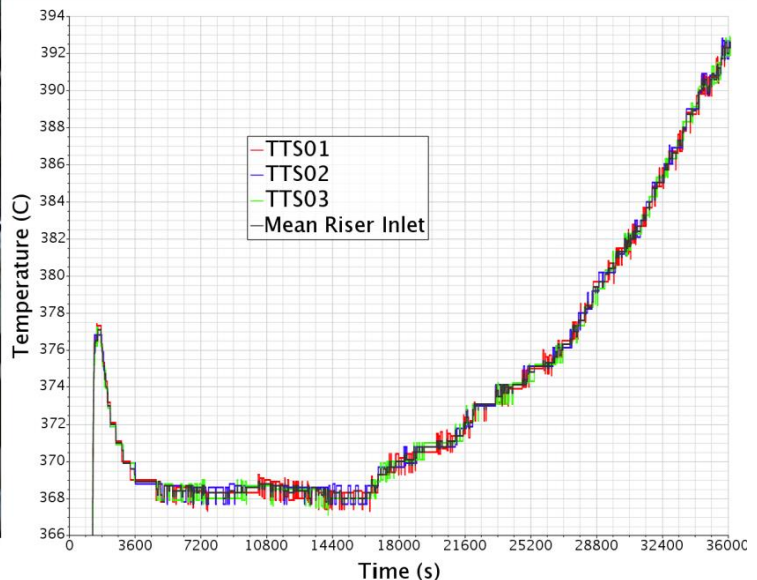
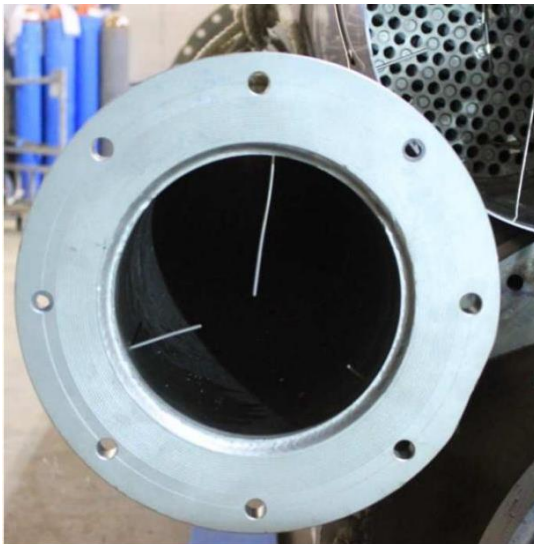


Figure 13: TCs installed at the riser entrance

Figure 30: Test case1. Riser inlet. Left. position of the TCs. Right. temperature history.



Figure 14: TCs installed at the riser exit

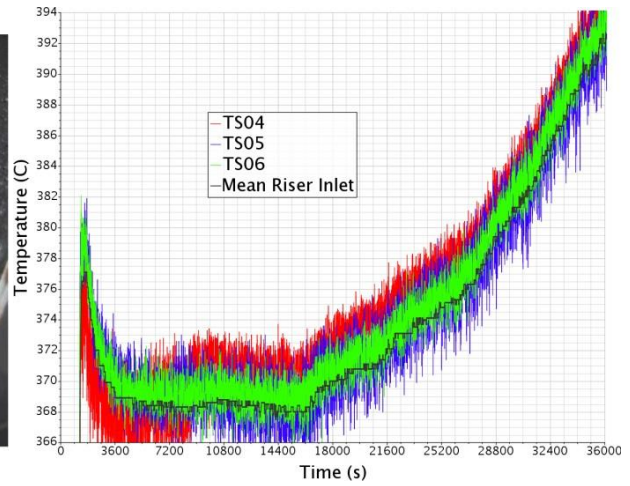


Figure 31: Test case 1. Riser outlet. Left, position of the TCs. Right, temperature history.

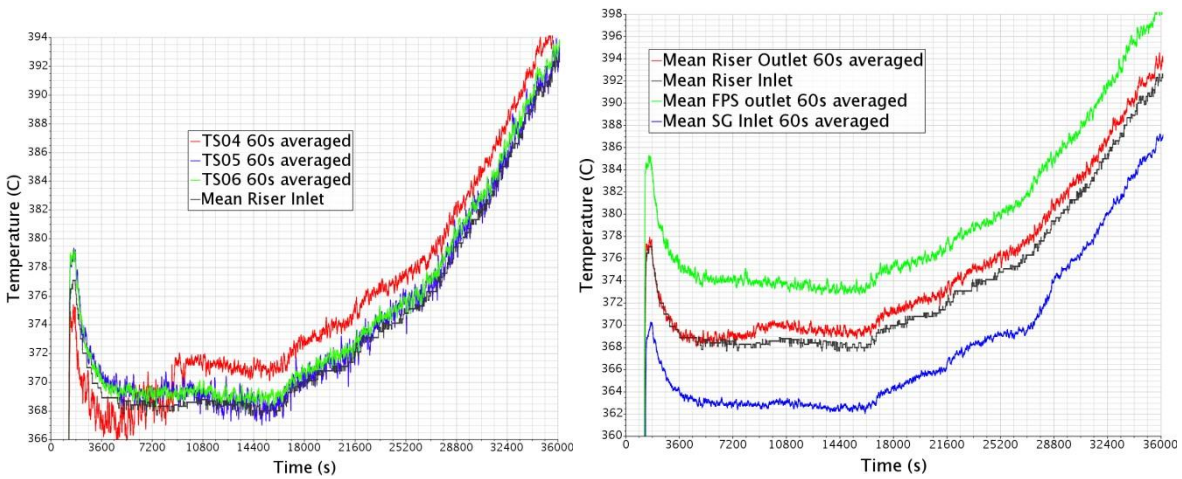


Figure 32: Test case1. Left, riser outlet TCs averaged temperature 60s vs. riser inlet mean TC temperature. Right, mean averaged 60s temperatures on TCs in FPS outlet, riser inlet, riser outlet and SG inlet.

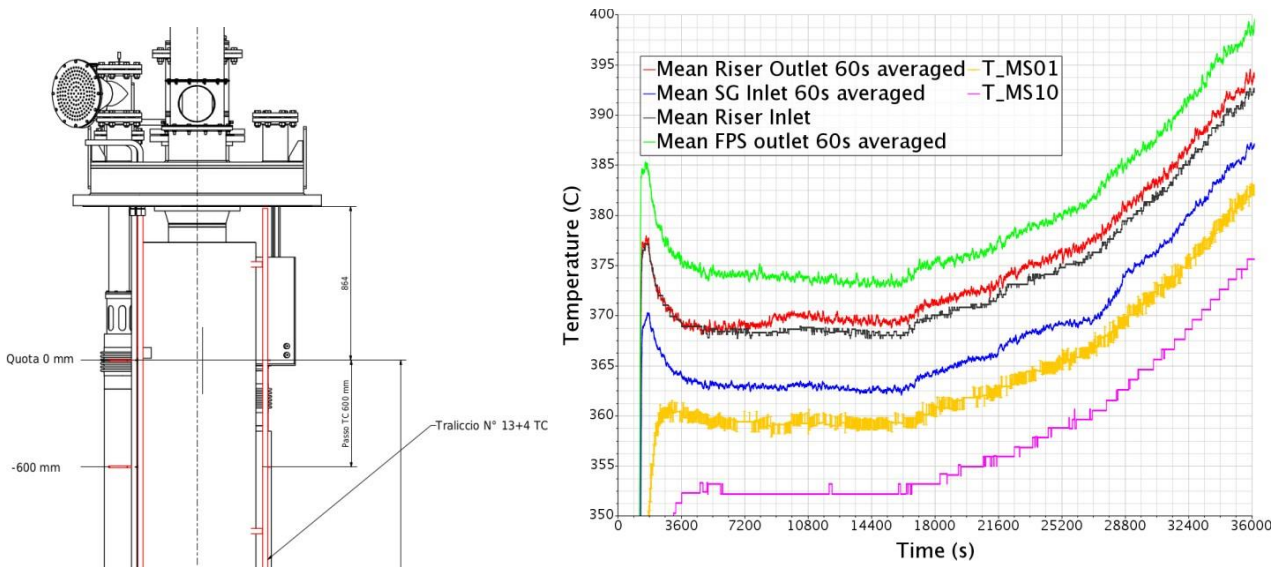


Figure 33: Test case 1. Left, sketch of CIRCE upper part. Right, temperature history as in Figure 32 and bulk temperature of the 2 upper TCs of the A-line.

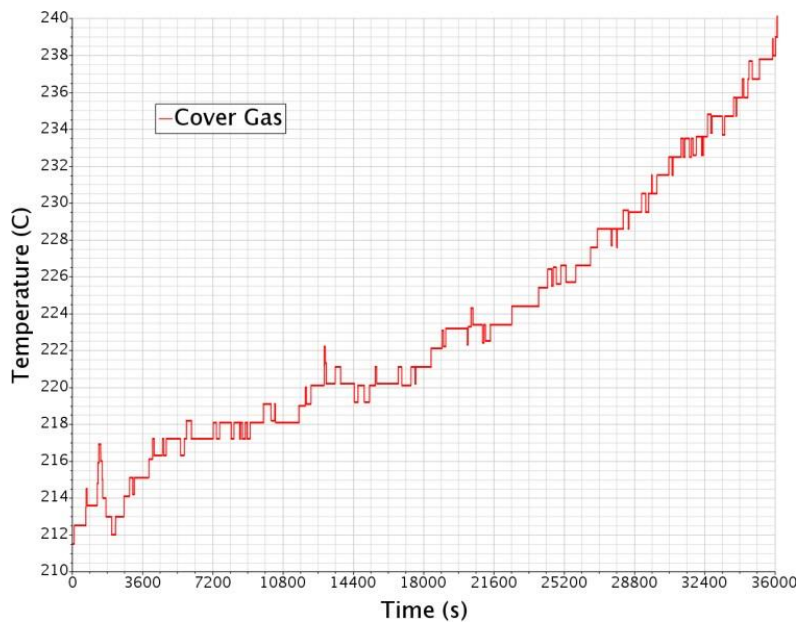


Figure 34: Test case 1. Cover gas temperature.

16 Updated numerical model

The analysis of the ENEA data on CIRCE-ICE has given some insight on some undue shortcoming that have been used in the pre-test elaboration of the numerical model. Moreover, some apparent inconsistency of the data has brought us to be more cautious with their interpretation.

Several possibilities have been elaborated to explain the observed discrepancy between the experimental and numerical results.

With regards to the numerical model, many variants or improvement can be implemented which do not depend on the current geometrical representation and its discretization. On the other hand, the characteristic times of the experimental facility together with VoF formulation forbidding a steady-state approach make is so that a simulation requires a huge amount both of time and of computational power. This forbids a generalized parametric approach with variation of several parameters. The attempts of possible improvements of the numerical model have thus been combined together to perform a new simulation.

1.4 Main changes

The main changes in the numerical model are now shortly listed:

1. FPS: radial restriction of the heat source.
2. Conveyor/Riser: increase of the wall thermal resistance (fouling hypothesis)
3. Bypass Gas separator/Plenum by use of source/ink terms
4. Change of the SGE cooling parameters: radial restriction and lower cold reference temperature.
5. Slightly pulsed force in the riser

1.5 FPS heat source radial restriction

The heat source was formerly modelled as a constant heat source density localised inside a numerical hexagonal region surrounding and overlapping the active part of the pin bundle. However, the measures at the top of the FPS active part, see Figure 27, indicate a strong decrease of the temperature from the centre to the periphery of the bundle. Extrapolating roughly from these incomplete data, it is quite probable that the external wall temperature remains essentially close to the FPS inlet temperature and the conjugate heat transfer towards the plenum is quite limited.

To reproduce qualitatively this effect, we limit the heat source such as to stay a little away from the external wall, as shown in Figure 35. Anticipating on the results, the lateral heat transfer is reduced by one order of magnitude from 10 to about 1 kW.

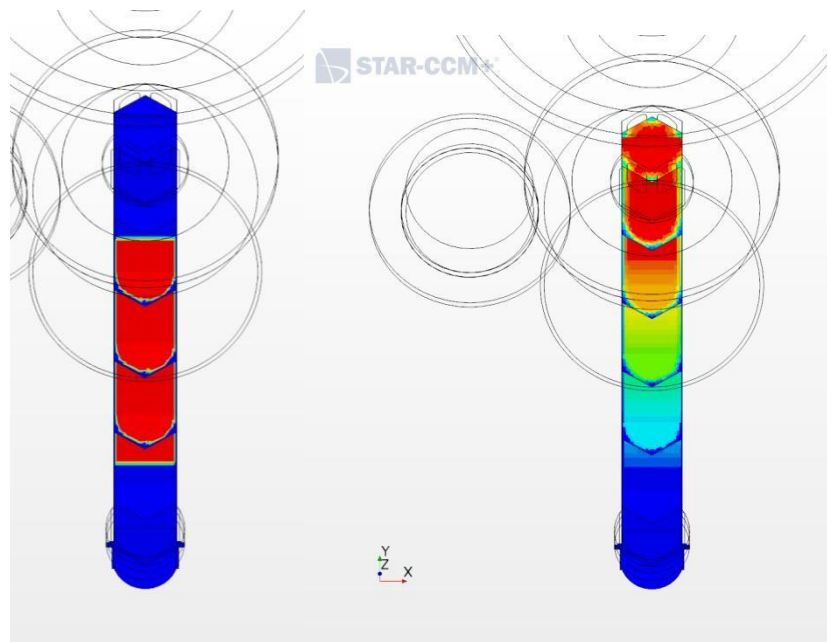


Figure 35: shape of the heat source in the model FPS region and corresponding temperature profile

1.6 Conveyor/Riser thermal resistance

In the former numerical model, the conjugate heat flux from the conveyor and riser bottom seemed greatly overestimated and led to an excessively cold temperature at the riser top. The reason is unclear and can be both numerical and physical. A possible cause is the presence on the walls of a layer of low conductivity LBE oxide. This can be simulated by giving a thermal resistance to the corresponding fluid-solid interface. The value of the resistance has been set so as to reduce the heat transfer from 110 kW to 60 kW and therefore to increase the LBE temperature at the riser outlet by about 5K. This is illustrated in Figure 36.

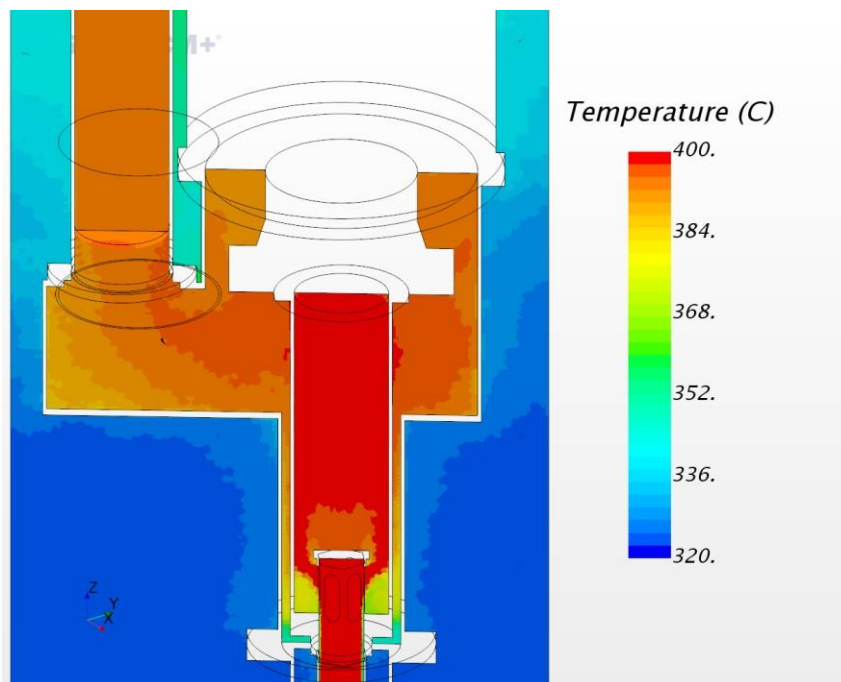


Figure 36: LBE temperature field inside and outside the conveyor/riser bottom.

1.7 Gas separator bypass

It is very likely that some LBE pass directly from the gas separator to the plenum. The amount is however totally unknown. The first mechanism is certain and is by droplet ejection cause by the two-phase LBE-Argon flow with a high volume fraction of Gas(3NI/s of Argon at 220 C, in front of 6.3 l-s of LBE). The second mechanism is uncertain and would be through a leaking connection between the gas separator bottom plate and the riser pipe. Both mechanism would contribute to an higher temperature at the top of the plenum.

The numerical model is unable to simulate directly the droplet ejection. Besides, modelling directly the leakage requires a predisposition at the geometrical level that was not thought after.

To obtain a similar effect, we make some LBE disappear from the gas separator and directly reappear at the plenum top. Numerically, this is done by (i) setting a sink term of LBE volume fraction together with the corresponding sink term of energy localized on top of the riser and (ii) setting source term of LBE volume fraction and energy with the same integral amount but localized at the top of the plenum. For commodity due to the complex shape of the top plenum horizontal section, the source terms covers all the LBE region over an horizontal slab, as shown in Figure 37, so that only a part of the subtracted LBE reappear in the plenum.

Initially 0.7 kg/s then about 1.3 kg/s (2%) of the flowing LBE is transferred in this way. The effect is difficult to quantify because it depends on the temperature difference between the riser and the plenum top and should contribute to reduce this difference, but very slowly in time.

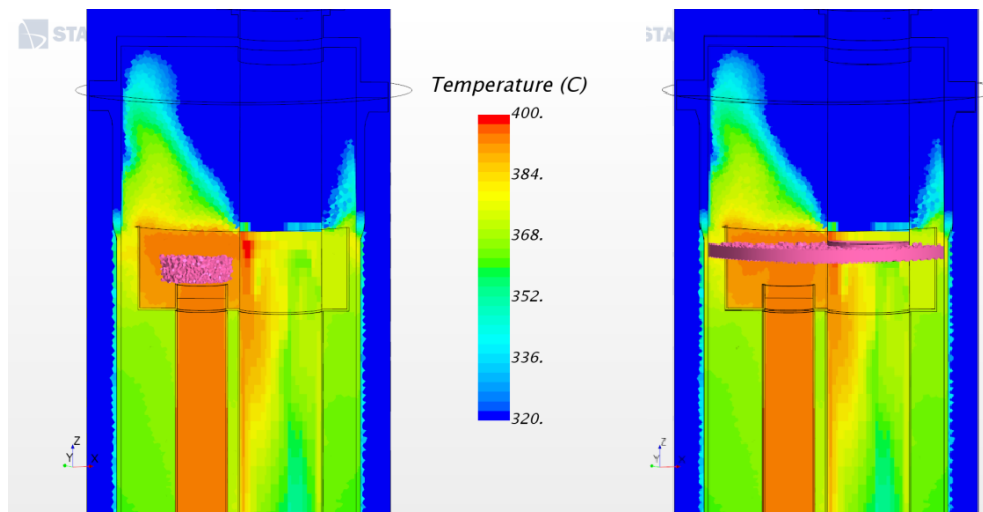


Figure 37: Vertical section passing through the top of the riser, the gas separator and the SGE, colored with temperature. In pink, the localization of the sink (left) and source (right) terms.

1.8 SGE cooling parameter change

Cooling in the SGE is obtain by setting there a sink term in the energy equation. The sink term has been constructed to be easily and understandably tuned for the purpose of the moment. The formula is the following:

$$\chi * V_{LBE} * \rho_0 * C_{p0} * (T_0 - T) / \tau$$

where χ is the support (localization) function, V_{LBE} is the LBE volume fraction, ρ_0 and C_{p0} are reference LBE density and specific heat, T_0 is a reference (or target) temperature, T the local LBE temperature and τ a characteristic time.

Its effect is to bring the LBE temperature close to T_0 in a characteristic time τ . Setting a characteristic time small in confront with the residence time forces the LBE outflow temperature to be very close to T_0 and can be very convenient during the initial phase of a simulation. Later on, the T_0 can be related to the secondary coolant (water) temperature and needs not necessarily be constant in time or space.

With regards to the formulation presented in D3.2, the main difference is the introduction of the support function. Formerly, it was only implicitly represent through the application of the sink term only on the dedicated numerical region. In the present case, we want to restrict the application of the sink term only to a part of this numerical region. In fact, it is applied only to a cylinder slightly smaller than the SGE, in an attempt to reproduce qualitatively what has been found out at chapter 13, the LBE near the SGE wall is quite hotter than the mean on the level. The distribution of the SGE energy sink at the end of the simulation is illustrated on Figure 38.

Contemporaneously, we have reduced the reference temperature T_0 to 120 C, more in line with the water steam temperature. Then the characteristic time has been adjusted (to 112s, much more than the residence time) to maintain the continuity of the overall (integrated) sink. The combined effect of lowering the reference temperature while keeping the total heat sink is to delay the cooling, that is, to have less cooling at the top and more cooling at the bottom. This results in an higher mean temperature along the vertical of the SGE. All in all, the changes operated are expected to give an higher SGE wall temperature at preserved power. In turn, this should lead through conjugate heat transfer to an higher temperature in the plenum at the level of the SGE.

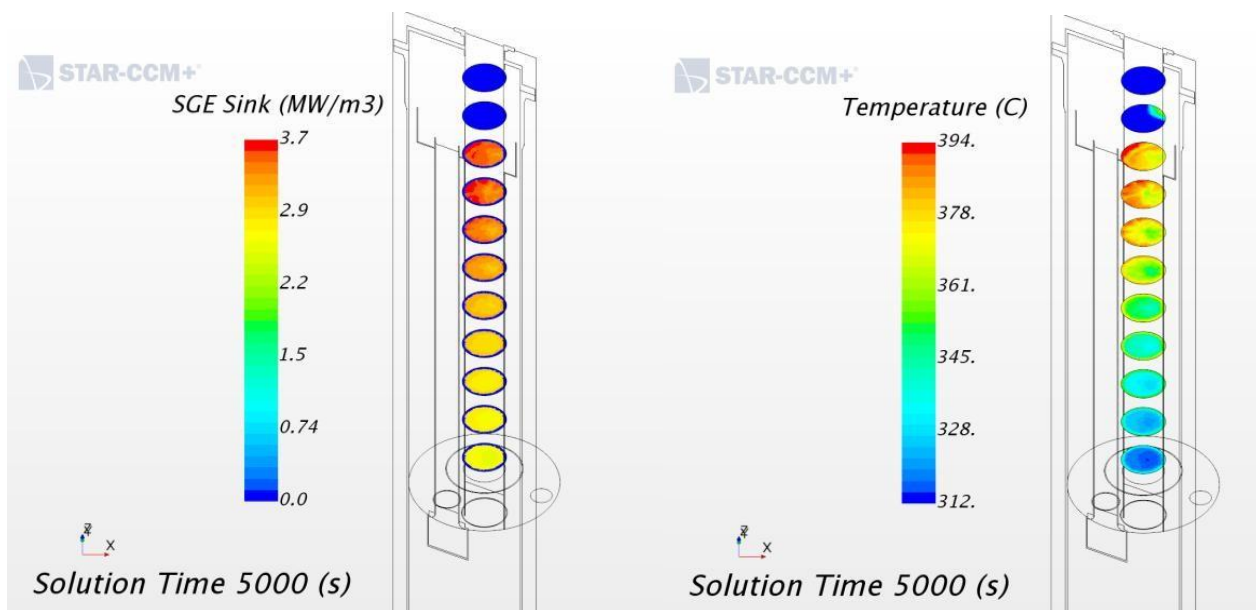


Figure 38: distribution of the SGE energy sink at the end of the simulation and corresponding temperature.

1.9 Pulsed body force

In the experiment, the mass flow rate in the FPS is not constant, it varies quite chaotically, see Figure 25, as the result of the forcing given by the gas lift system. We want to qualitatively reproduce this variability, to see (i) how it is propagated, (ii) if it changes the conjugate heat transfer and (iii) if it triggers instability below the SGE lower grid and in the plenum intermediary region of instability.

The original lifting force in the riser has been modulated by a 10% amplitude sinusoidal signal with period about 12s. This change has been operated during the course of the simulation and contemporaneously with the change of top mass transfer from 0.7 to 1.3 kg/s and maintained for 3600s (1 hour) of physical time.

The effect of the pulsed lifting force is illustrated in Figure 39 and Figure 40. In Figure 39, the initial difference of mass flow between the Riser and the SGE is due to the bypass flow which is doubled during the transition. It is interesting to see that the flow oscillation in the riser is already strongly damped in the SGE. This is an effect of the VoF treatment of the free surface and is perfectly (at least qualitatively) physical. On the RHS, the effect of the pulsation on the temperature is felt as is obvious on top of the PFS active part (in red), already slightly less at the FPS outlet (in dark blue), negligible or absent everywhere else, including the SGE outlet.

In Figure 40 left, we can see that the effect on the main conjugate heat flux is negligible. The evolution of the TC temperature of the A-line in the unstable intermediary region is shown on the right. The change of slope is most probably related to the increase of bypass flow. Numerically, the flow is absolutely not destabilized. All in all, the only real effect of the pulsation is to blur the numerical results, that is, there is no reason to repeat the numerical experiment, letting some level of relevance to future steady-state simulation.

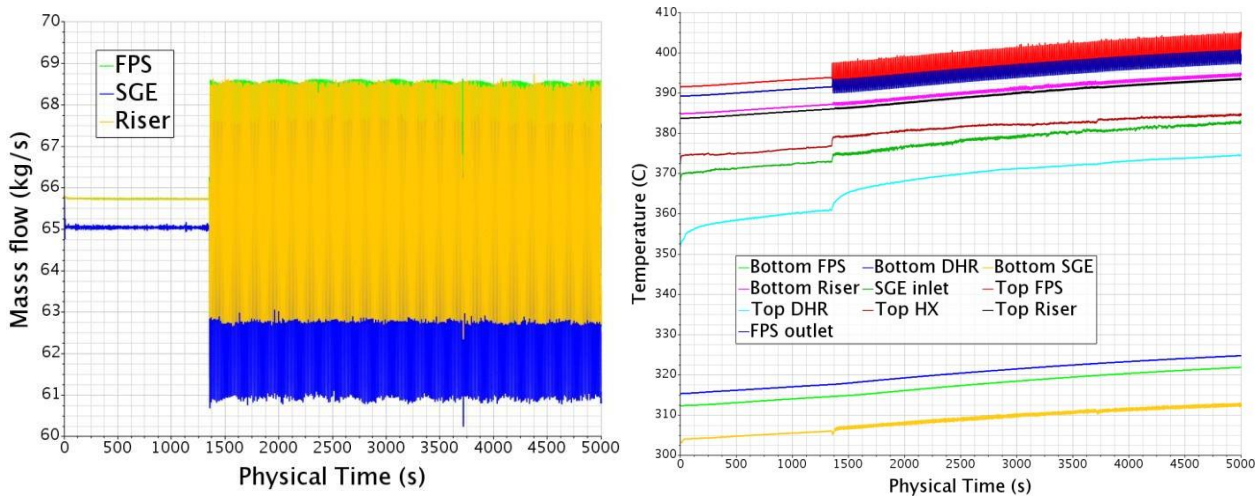


Figure 39: effect of the pulsed lifting force. Left: mass flows. right: flow averaged temperatures.

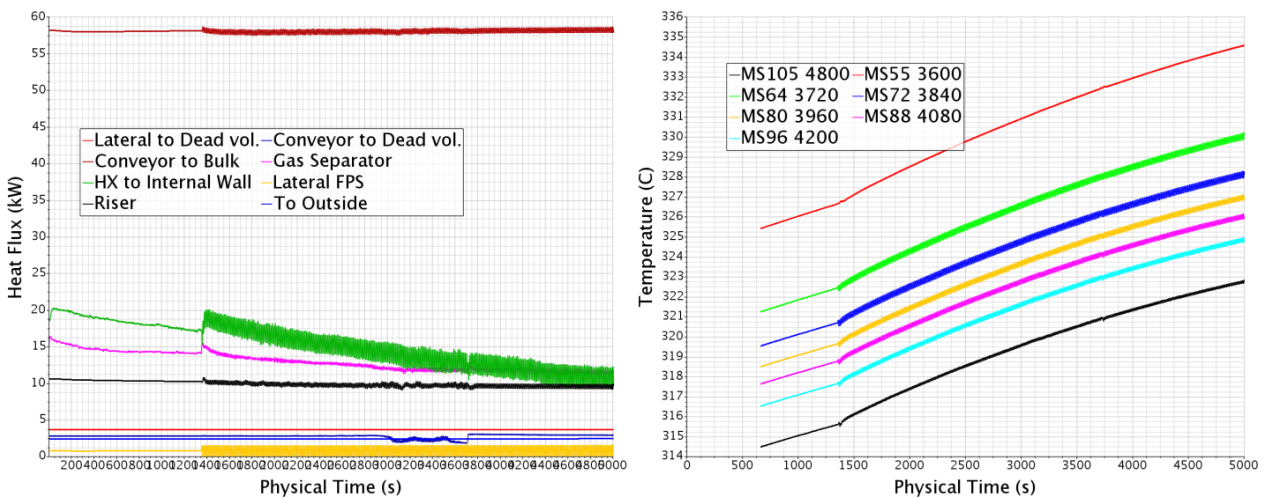


Figure 40: effect of the pulsed lifting force. Left. main conjugate heat fluxes. Right: temperature history at the Line A TCs located around the intermediary region of instability.

1.10 Main result, discussion

The simulation has been pursued for about 2 weeks of man-time on 200 CPUs and about 3h of physical time (only the last 5000s are illustrated) progressively including the new features, lasting with the pulsation. At the end of the simulation, the temperature at the FPS inlet was almost equal to the temperature in the experiment at time 10h. So, it makes sense to confront the temperature profile at this time. Similarly to the experiment, the model is not yet in thermal equilibrium as already shown on several figures.

In Figure 41, we plot the temperature of the plenum TC lines according to their depth. The numerical probes are grouped on a line by line basis while the experimental temperatures have been agglomerated in a single curve following the database order. It is interesting to note that at this precise instant, there are some thermal inversions in the chaotic intermediary region (around depth 4m), illustrating the variability of the thermal field in this region.

With regards to the previous simulation, the temperature excursion between the top and the bottom of the plenum has increased from 30K to about 48K. It still lacks more than 10K to match the experiment. Besides, the intermediary plateau region that was formerly more present in the simulation than in the experiment, is now completely absent of the new simulation results. Similarly with the former simulation, the numerical TCs at a given depth give about 5K dispersion from the top up to 4m, while the experimental values above 3.6m depth are much less dispersed. It looks like the thermal buoyancy effect is loosely captured by the simulation. This may be a numerical issue related to the strongly vertically confined volume and the VoF approach in which the phase-induced buoyancy is about 3 orders more than the thermal one. This feeling is reinforced while looking at Figure 43, showing the vertical velocity field on different planes of the domain. This field is spotted with neighbouring cells at different values. The picture shown is extremely stable in time which can be interpreted as a problem of pseudo-convergence. Reducing the time step, stiffening the convergence parameters and/or increasing the number of iteration per time step has no effect on the velocity field on this illustrated region.

The temperature field is illustrated in Figure 42 where we can observe several interesting features:

- the conveyor is heating the nearby plenum creating a rising hot plume very close to the cold down-coming flow from the SGE bottom.
- The temperature is highly discontinuous between the riser and the plenum, indicating a good insulation.
- The temperature is almost continuous through the SGE walls, indicating a strong control of the plenum temperature by the SGE wall temperature.
- A similar effect is observed at the gas separator level. Note that the temperature scale of the figure on the right is quite reduced.
- Still at the gas separator level, the LBE behind is already cooled by more than 20K indicating that it has passed through the SGE bulk, while by looking at Figure 11 it should have passed through the free SGE border. This dissymmetry of the temperature field is propagated several meters below and may have an important role in reducing the plenum top temperature. This is caused by the planar high porous resistance extending radially all over the SGE numerical region while it should be restricted to the real region of influence of the SGE bundle.

While the changes brought to the model do not lead to a better capture of the plenum temperature profile, it has led to a better understanding of the reason of the discrepancies and to possible workarounds.

Here is the current interpretation:

- In the upper 2.5 m, the flow is almost stagnant. The plenum temperature profile is strongly controlled by the gas separator and the SGE wall temperature. This temperature is in turn controlled in large part by the SGE modelling. The SGE modelling considering an homogeneous cylindrical porous media is insufficient to capture the right wall temperature profile. The horizontal hydraulic resistance should be restrained to the effective zone (roughly of hexagonal shape) of influence of the SGE tubes. This is also valid for the cooling sink term. Moreover, a better attention should be given to the law governing the cooling sink term. As a first level of improvement, the reference temperature should vary with height according to a consistent profile of temperature on the water side. The global effect should be both an higher wall and bulk temperature, at parity of power.
- In the temperature plateau region, roughly between depth 2.4 and 3.6m, the flow is almost stagnant in a large part of the plenum. The upper bound of the plateau is probably located where the SGE walls become (slightly) colder than the plenum, that is where the heat flux between the SGE and the plenum changes direction. The reason why the plenum does not any more strictly follow the SGE wall temperature is because of the hot plume rising from the conveyor and the riser bottom. This plume is rising quite far away from the TC lines and its heating power dissipates locally against the cooling of the SGE walls. By strongly and artificially damping the conveyor conjugate heat transfer, the hot plume has much less strength and the SGE wall temperature continues to control alone the plenum temperature down to the next region.
- In the lower strong vertical mean temperature gradient region, roughly between depth 3.6 and 4.2m, the flow is quite chaotic. The cold LBE from the SGE bottom grid falls down accelerated by buoyancy inside the guide tube below the SGE bottom grid. Conservation of mass makes that the accelerated cold plumes are compensated by the entering of hotter LBE from below in the SGE bottom channel. The cold plumes also strongly interact with part of the hot plume from the conveyor. This

configuration is rather unstable but creates a fast and rather good mixing limiting the penetration of the cold plume not too far below.

- In the bottom region, roughly below depth 4.2m, the temperature is quite homogeneous. It is difficult to guess whether the flow is essentially stagnant, slowly going down homogeneously to the FPS inlet or if there is some kind of residual kinetic energy from the cold plumes that induces some large scale but anyway slow flow pattern. In any case, numerical prediction fits well the experimental results here.
- It could be wiser to let the VoF framework down. This is for several reason. First, there is no particular influence of relevance of the free surface effect on the flow. Having already renounced to model the Argon injection with a distinct phase, the VoF becomes useless. It would have an effect to damp oscillations of the driving force in the riser but we also intent to avoid this type of forcing. Second, the VoF setting is incompatible with the steady-state setting which is a potentially very powerful tools to accelerate convergence to a nominal condition. Third, it is also incompatible with the coupled flow setting that we expect to be more suited to capture small buoyancy effects.

Because, the current geometrical model is not suited to satisfactorily implement the necessary modification, a new geometrical model has to be build and meshed. This is a long and heavy work that would bring us beyond the permitted deadline and man-power. Hopefully it will be performed in a successive or different framework.

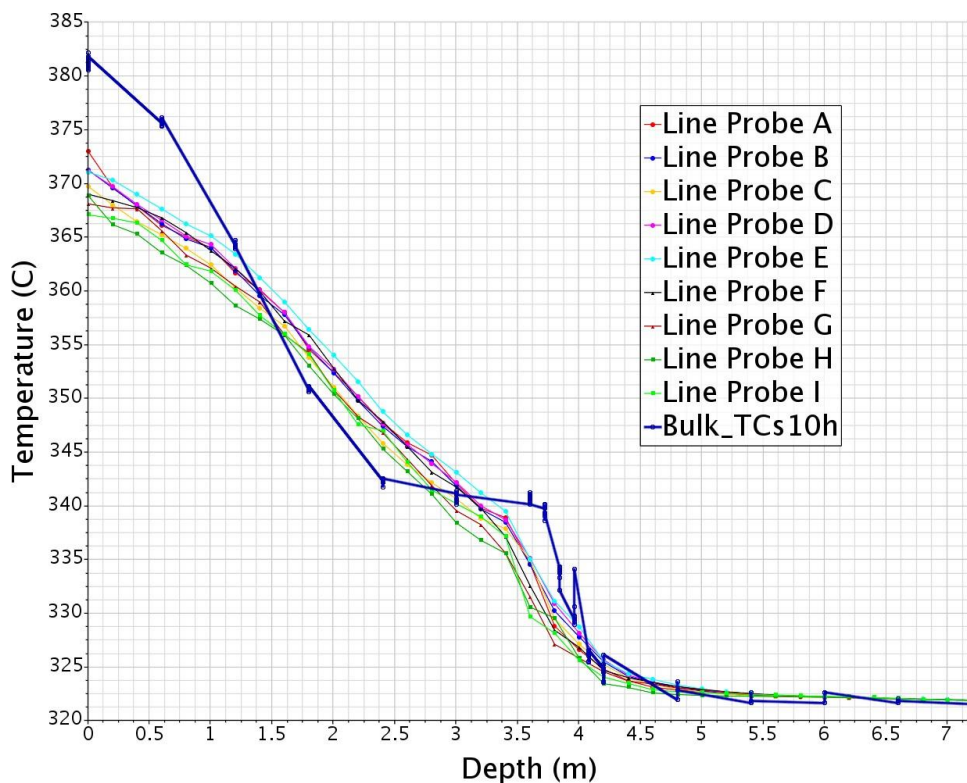


Figure 41: confront of the numerical Line Probe temperatures and the experimental temperature at time 10h. aggregated in the dark blue line.

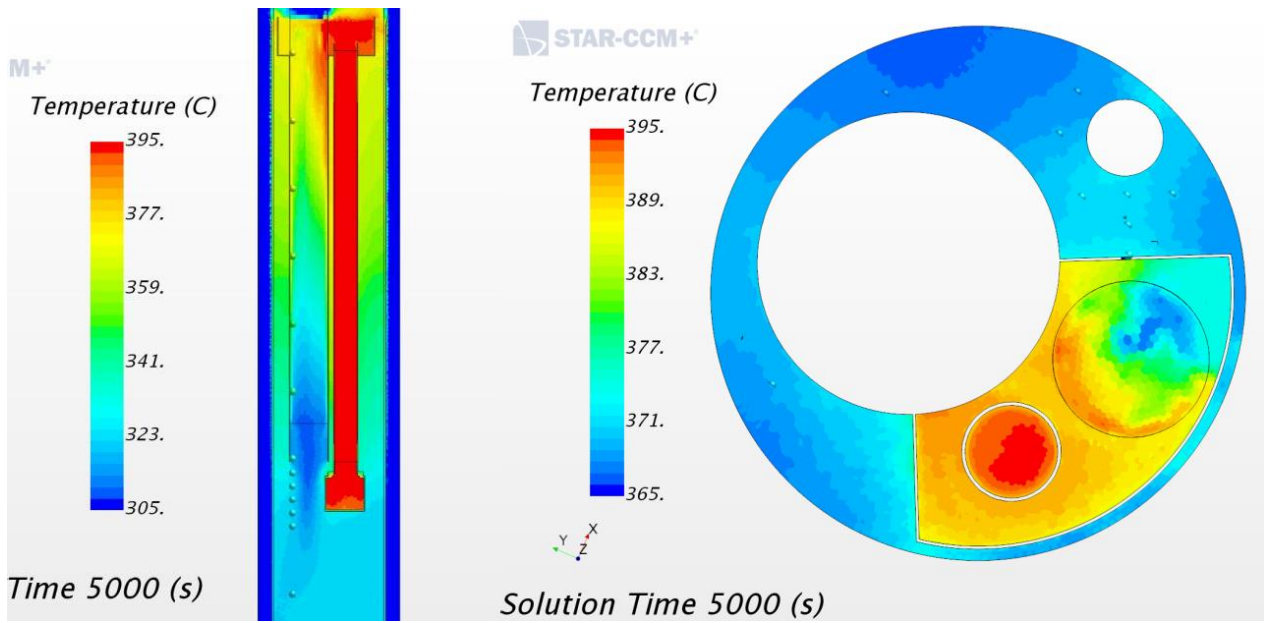


Figure 42: temperature field. Left, vertical plane passing through the riser and the SGE and position of the Line A TCs. Right, horizontal plane just above the gas separator bottom plate.

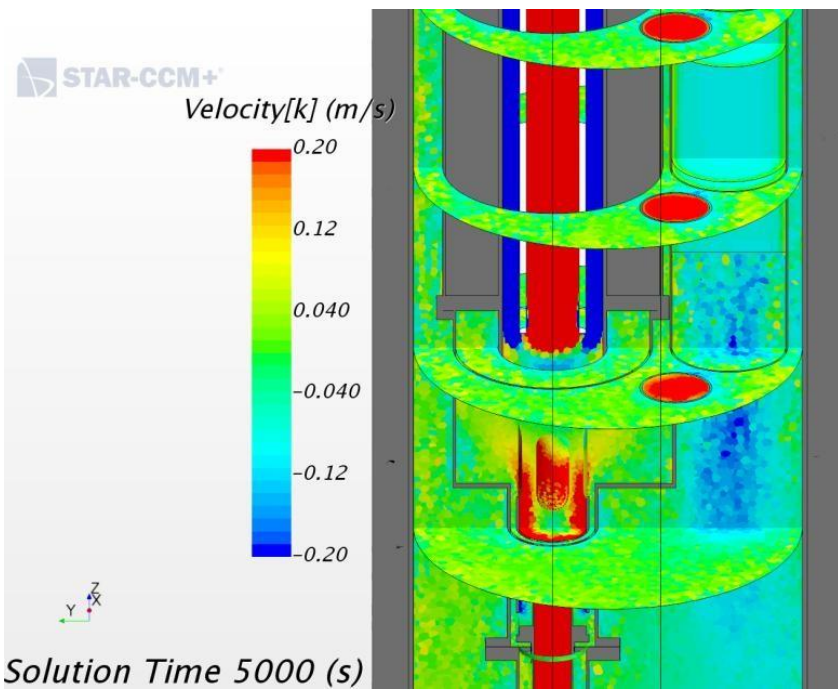


Figure 43: vertical velocity field around the FPS outlet and the SGE outlet, on different planes.

17 Steady-State model

A new geometrical model has been constructed from scratch, taking into account all the possible requisites encountered until now. Most important is the possibility to operate the model using the steady-state framework. This means that the VoF framework is no more used and the cover gas region is separated in a specific numerical region.

The SG modelling has been improved, taking into account the information gained in chapter 13. The hydraulic resistance and the heat sink have been restricted to an hexagonal shape inside the SG cylindrical casing. Details are given in annex 1.12. Moreover, the reference temperature for the heat sink depends on the vertical position according to Figure 12 left.

The coupled flow solver has been used as probably more suited for buoyancy or partially buoyancy driven flows.

The steady-state suffers the same problem as the transient simulation in the sense that the complete thermal equilibrium is extremely long and in practice impossible to reach. Moreover, the numerical model was extremely sensitive to small variations of the main parameters such as the resistance coefficients in the porous media and the riser body force. Any change led to tens of hours of computational time (usually on about 200 CPUs) to recover we had to limit the number of adjustments. The main parameters of the current model are:

- FPS power: 800 kW
- Riser pressure load: 21 kPa
- Mass flow rate riser: 62 kg/s (Experimental ~65.5 kgs, i.e. 6% more).

At the end of the steady-state simulation, in front of 800kW heat power, we have “only” 790kW of total heat loss with 776kW from the HX. The simulation has been restarted with success for 10s in transient mode and is therefore suitable for a future transient test.

The main result is shown on Figure 44, where we confront the numerical and experimental results in the plenum temperature vertical profile. The experimental results are those already given are shifted down by a 15 K offset to allow an easier confront. The numerical profile now captures very well most of the characteristics of the numerical one. Up to the discretization given by the experimental quotes, all changes of temperature gradient are qualitatively and quantitatively captured. Only the total temperature drop between the intermediary and the bottom plateau is clearly overestimated numerically by about 11 K. The temperature drop from the top to the bottom of CIRCE is 61K experimentally and 72K numerically (18% more). The main causes are:

- 6% mass flow difference
- ~7% electric power difference (estimated loss in the dead volume)
- Experiment ~28 kW away from thermal equilibrium (3.5% of total heat source), and simulation only 10 kW away,

the remaining part coming from the numerical approximation and modeling approach.

The temperature profile can be appreciated in Figure 45 with emphasis on the SG. The temperature is lower on the SG axis and higher on the border, with the hexagonal shape clearly recognizable.

From the numerical point of view, the flow in the plenum has become mostly coherent with two main coherent large structures below the SG outlet, as can be seen in Figure 46 and in Figure 47. This justifies a posteriori our strong concern with the spotted velocity field observed before and shown in Figure 43. Most of the modelling is equal or very similar in both cases. This is a strong indication that our VoF setting fails to capture the correct flow pattern characterized by a large region dominated by buoyancy.

Below the SG bottom grid, the cold flow forms a down-coming plume pushed away from the hot plume rising along the conveyor. Some flow from the plenum enters the SG flow guide up to the lower grid. This feature is most probably unsteady and is the numerical counterpart of the high experimental variability. However, the strong coherence of the cold plume allowing it to better progress downward is probably the reason why

mixing is limited below the SG in confront with the experiment. In effect, from the experimental temperature measure below the SG, we expect a much more complex and dispersive configuration.

The main flow averaged temperatures are given below:

- Inlet FPS: 295.6C
- Top FPS active: 384.4C
- Outlet FPS (lateral): 383.0C
- Inlet Riser: 370.6C
- Outlet Riser: 370.3C
- Inlet SG: 369.5C
- Outlet SG: 284.0C

These temperatures indicate a drop of about 14 K corresponding to 125 kW of heat losses through the walls between the top of the FPS active part and the bottom of the riser. On the other hand, the LBE flow is heated by 11.6 K of turbulent and large scale mixing, equivalent to ~105 kW between the SG outlet and the FPS inlet.

The 14K drop is about double what could be directly extrapolated from TC data.

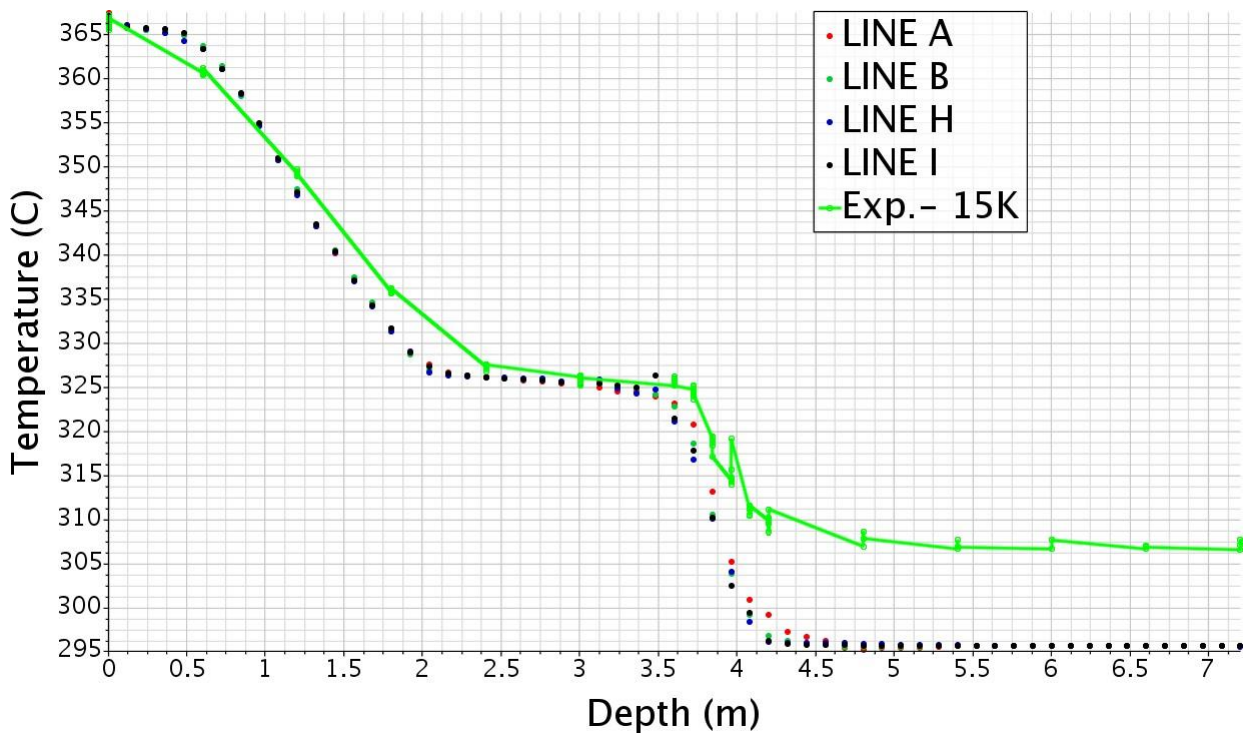


Figure 44: temperatures along the plenum TC lines: curve experimental, dots numerical.

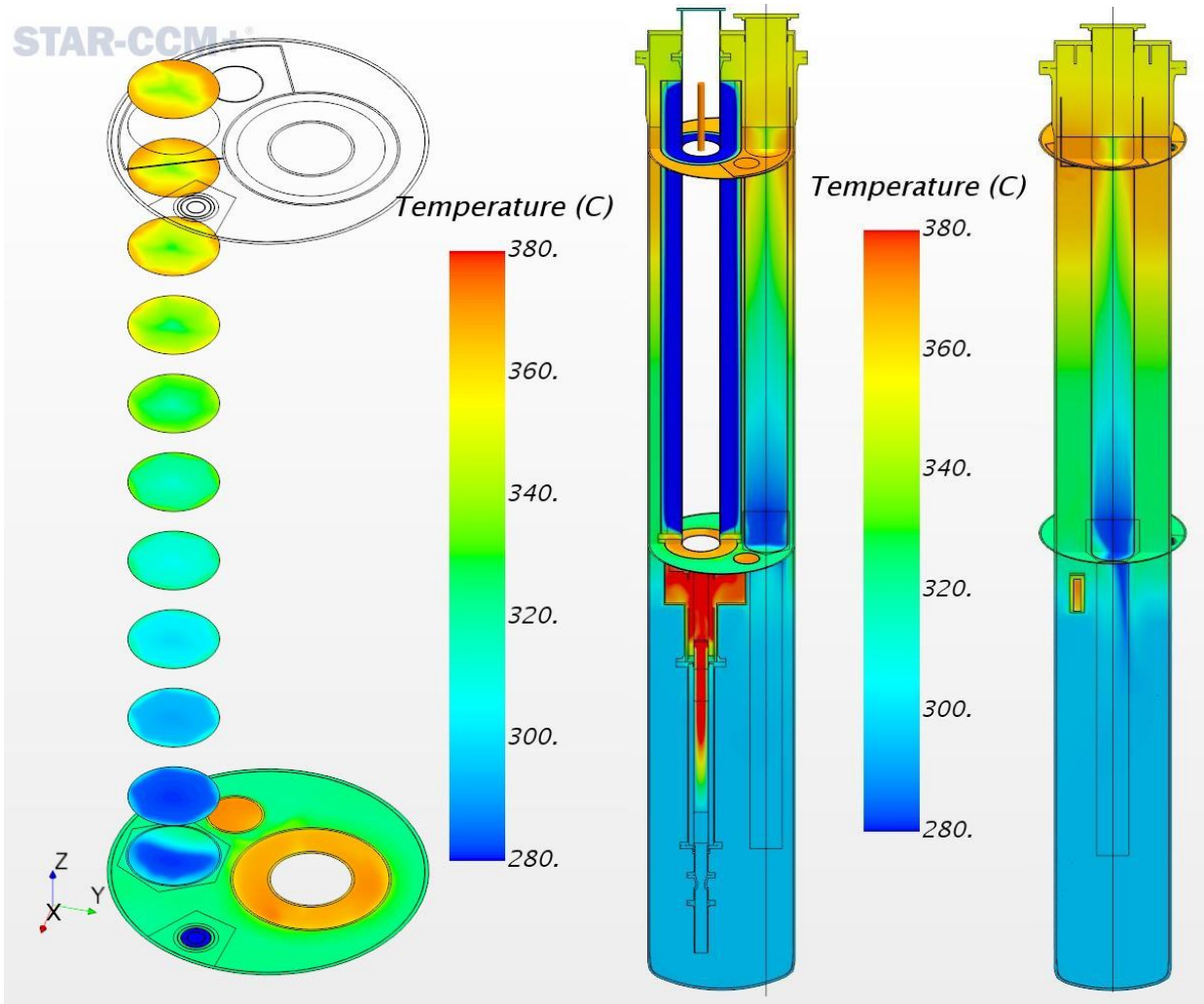


Figure 45: temperature field on planes crossing the SG.

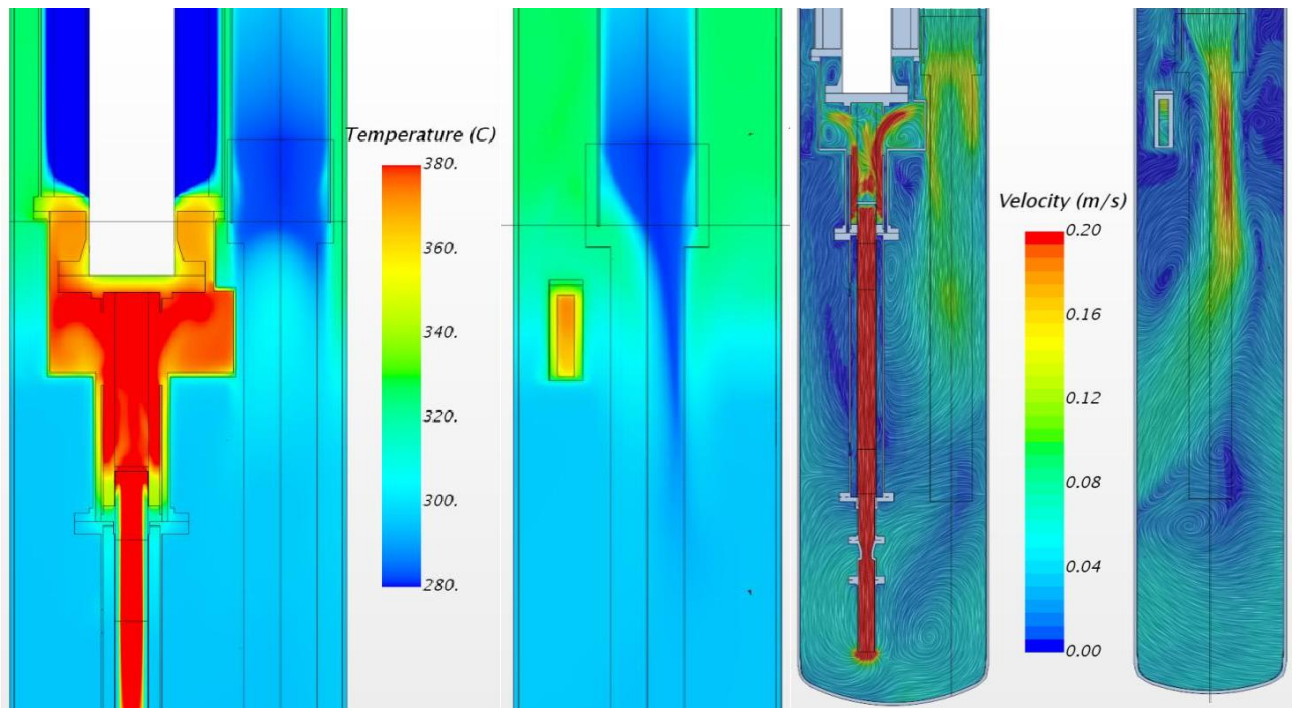


Figure 46: vertical planes crossing the SG. Left, temperature. Right, velocity.

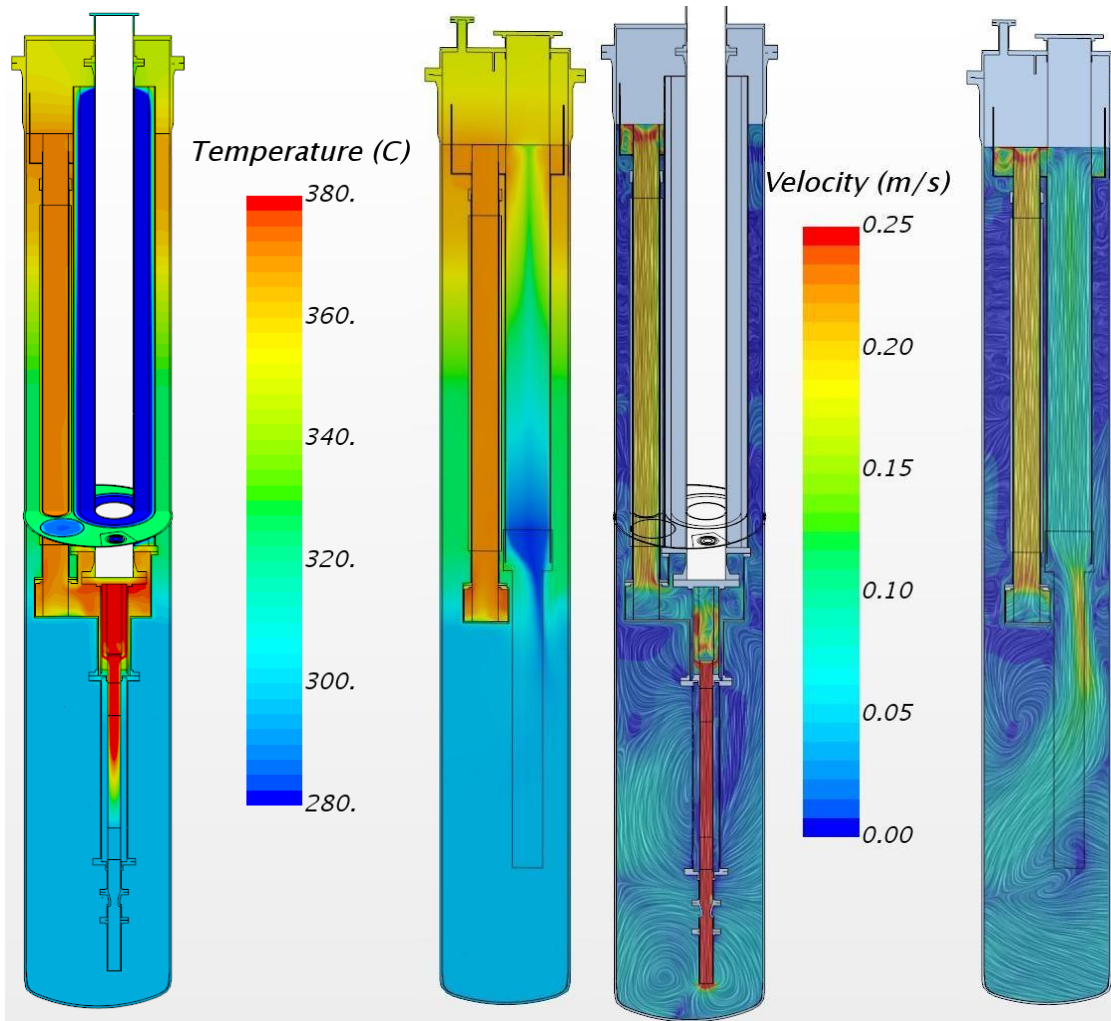


Figure 47: vertical planes crossing either FPS and riser or riser and SG. Left. temperature. Right. velocity.

18 Conclusion

In this work, we have constructed and operated numerical models of CIRCE in ICE configuration. Our initial aim was to reproduce at least the initial quasi steady-state experimentally reached before the loss of flow transients during the SESAME experimental campaign by ENEA.

This work builds on a model constructed in a pre-test phase that was not judged satisfying. We have thus entered a phase of deeper analysis of the experimental results and of the shortcomings of the numerical modelling.

The first 10 hours of test were supposed to let the system reach the nominal condition and in particular to reach a global thermal equilibrium. With regards to the analysis of the database, we can observe that the flow is far less steady than anticipated and never really reaches thermal equilibrium. The mass flow rate in the FPS oscillate chaotically essentially between 63 and 69 kg/s and still varies between 65 and 67 kg/s when averaged over 60s. From the thermal point of view, the thermal imbalance is about 28kW during more than the last 3 hours of the initial transient stage. Moreover, the temperature probes at the SG bottom grid indicate a very uneven flow and cooling distribution and a complex time flow behaviour composed of a mix of slow variations, and some fast variations, these later appearing as jumps on the 10 hour time-scale. The flow below the SG bottom grid and around is also particularly unsteady, even at scales far beyond the turbulence ones.

These features bring intrinsic limitations on the validity of a steady-state numerical CFD representation. Besides, the numerical modelling makes use of unresolved regions: (i) the FPS and the SG because the pin and tube bundles are not geometrically represented and (ii) the gas lift system in the riser and the flow separator is not represented by a bubbly flow but only through a lifting force density. In these regions, only integral or semi-integral values make sense. In particular, a confront with the pointwise values given by the TCs is of particular difficulty and must be considered as merely indicative.

In the end, only the plenum temperature data on the vertical TC lines can be used for an experimental/numerical confront, once the adjustment based on the FPS inlet temperature has been performed. That is, the profile of the temperature along the vertical of the plenum is the more relevant criteria for a numerical/experimental confront. By using the usual numerical modelling, this profile has been essentially captured correctly but only in the framework of the single flow coupled solver. Instead, in the VoF framework (allowing only the segregated flow), the temperature profile is essentially not captured and moreover, the velocity field in large portions of the plenum looks unrealistic.

At a lesser extent, we have observed that in the CIRCE configuration investigated, the thermal profile in the upper part of the plenum is mainly controlled by the temperature profile of the SG envelop. In HERO configuration, this envelop is quite hotter than the SG bulk flow due to important border effects that have been neglected in a first approach. The semi-integral modelling of the SG has been improved and is now able to represent this border effect together with a more realistic LBE temperature distribution.

19 Acronyms and definitions

Acronym	Definition
CIRCE	CIRColazione Eutettico
CFD	Computational Fluid Dynamics
DHR	Decay Heat Removal
EC DG RTD	European Commission – Directorate General for Research and Technological Development
FPS	Fuel Pin Simulator
HERO	Heavy liquid mEtal pRessurized water cOoled tubes
HX	Heat eXchanger
ICE	Integral Circulation Experiment
LBE	Lead Bismuth Eutectic
LOF	Loss Of Flow
PLOF	Protected Loss Of Flow
PLOH	Protected Loss Of Heat sink
SG	Steam Generator
SGE	Steam GEnerator
TC	Thermo-Couple
VoF	Volume of Fluid

20 Annexes

1.11 Annex 1 – Mass transfer

It is quite likely that some LBE went directly from the gas separator region to the top of the bulk region. There are two possible means:

- Droplets ejected from the gas separator ends at the surface of the bulk LBE.
- The connection between the top of the riser and the gas separator was not tight and there was some leakage.

This is possibly true only for the CIRCE-ICE experimental campaigns as for the later CIRCE-HERO campaign the lateral wall of the gas separator has been raised up and the connection to the riser has been tightened.

Numerically, the second means can be simulated by setting a tiny part of the separator around the riser as a porous media region and control the possible leakage with the setting of the porous resistance coefficients. This is what is being done with the upgraded numerical model but was not available initially. Instead, the droplet simulation is far to be truly simulated, first of all because the droplets are a consequence of a bubbly flow with a high volume fraction of gas and we do not simulate the bubbly flow.

A numeral option for the simulation is to make some LBE disappear from the gas separator region and reappear at the top of the bulk region. Obviously, care must be taken than, beyond the mass conservation, also the enthalpy is globally conserved in the process. In the following, we explain the methodology used together with its effective implementation in the numerical model.

We first start with the localization of the LBE sink and sources as in the numerical model.

The sink is localized on a cylindrical region of radius $R_c=15\text{cm}$ slightly above the riser and centered on its axis of coordinates $C_x=-0.289\text{m}$ and $C_y=-0.325\text{m}$.

The height is comprised in the interval: Z in $[5.55 ; 5.65]\text{m}$.

The sink support function is thus defined like this:

$$X_- = 1, \text{ if } Z \text{ in } [5.55 ; 5.65] \text{ and } R_c < 0.15 \\ = 0 \text{ otherwise.}$$

Similarly, the source support function is defined as an horizontal slab 5cm high:

$$X_+ = 1, \text{ if } Z \text{ in } [5.65 ; 5.70] \text{ and } R_c < 0.15 \\ = 0 \text{ otherwise.}$$

Take also in consideration that the two support functions will be used only in relation to the “Main” LBE numerical region. The source is localized just above the sink but is not constrained laterally. Therefore, a part of the disappearing LBE will reappear just above. Only the part of the source support function out of the gas separator region will effectively induce a “useful” transfer of mass and energy. Reason of this choice is that the gas separator region does not have a simple mathematical characterization.

These support functions will be used to define cell sets where the sink and sources will be applied. The volume of the cell set does not coincide exactly with the mathematical definition because a cell will be considered in the volume if and only if its center fits the conditions. We have thus to integrate numerically these support functions, but only on the Main LBE region to get the corresponding volumes:

- Sink volume $V_- = \int_{\text{Main}} X_- = 6.53965\text{E-}3\text{m}^3$.
- Source volume $V_+ = \int_{\text{Main}} X_+ = 3.044371\text{E-}2\text{m}^3$.

These values will be later used as normalization factors.

We now define M^* (unit kg/s) the total mass transfer that we intend to perform. We keep in mind that the effective mass transfer will be lower because some of the vanishing LBE will still reappear in the gas separator region. The effective mass transfer will be obtained from the difference of mass flow rate between the riser inlet and the SGE outlet.

Numerically, within the VoF framework, we cannot set directly a mass source. The mass source is set indirectly and automatically while setting some volumetric fraction source.

We call VF^* the volumetric sink term in the LBE volume fraction equation (unit m^3/m^3s or s^{-1}). This term must verify the relation:

$$\int_{Main} \rho_{LBE} VF^* = -M^*$$

Which is satisfied by setting:

$$VF^* = -X.M^* / (\rho_{LBE} V_-)$$

where ρ_{LBE} is the specific LBE density (independent of the volume fraction)

Such that the implied mass source m^* is:

$$m^* = -X.M^* / V_-$$

We set the energy sink (i.e. the sink term in the energy equation, in W/m^3) to be:

$$e^* = -X.M^*h / V_-$$

where h is the local massic enthalpy of the fluid.

Note that there is no direct access to the enthalpy of the LBE phase and this expression can modify the fluid temperature if it is not (almost) exclusively composed of LBE.

The total energy E^* withdrawn to the fluid is obtained by numerical integration of e^* and is stored in a report.

Now both the LBE mass and LBE energy extracted from the fluid must be returned to the fluid but at its new position.

The total LBE mass is preserved by setting the volume fraction source $VF+^*$ as:

$$VF+^* = X_+M^* / (\rho_{LBE} V_+)$$

because in this case, we have $\int_{Main} \rho_{LBE} VF+^* = M^*$.

We choose to make a uniform distribution of the local energy source $e+^*$, even if the mass source is not completely uniform, because it is the only practical solution found. This leads to the formula:

$$e+^* = E+^* X_+ / V_+$$

or in term of the volumefraction source (as initially implemented):

$$e+^* = VF+^* E+^* \rho_{LBE} / M^*$$

1.12 Annex 2: SG 2-region model

The SG is modelled as a porous medium. However, it is composed of an hexagonal bundle of cooling pipes inside a cylindrical mantle, so that the mid-scale homogeneity is largely broken near the periphery. We want to take into account the free path left between the hexagonal array and circular perimeter.

The driving idea is to split the domain in two parts, a central hexagonal one representative of the bundle and a co-volume where the flow is not hindered.

1.12.1 Shape, size and porosity

Inside the tube bundle, we can unambiguously determine an hexagonal shaped zone of influence for each pipe, related to the bundle pitch $P=31mm$. The area S_p of influence of one pipe is:

$$S_p = \frac{\sqrt{3}}{2} P^2 = 832mm^2.$$

The area S_b of influence of the $N=91$ pipes of the bundle is:

$$S_b = N S_p = 75700mm^2.$$

The union of the N zones of influence is only approximately hexagonal and not practical to use. Instead, we regularize domain to make it truly hexagonal while keeping its area. The pitch P_b (or internal diameter) of the regularized bundle is:

$$P_b = \sqrt{N} P = 296mm.$$

The hexagon is inscribed in a circle of diameter D_b :

$$D_b = \frac{2}{\sqrt{3}} P_b = 341.5mm.$$

This diameter results to be slightly smaller than the mantle internal diameter $D_m=343\text{mm}$.

The porosity of the hexagonal shape is given by the single pipe diameter $D_p=25.4\text{mm}$ and S_p :

$$\alpha = 1 - \frac{\pi}{4} D_p^2 / S_p = 0.39$$

while the porosity of the co-volume will be 1.

The SG section being

$$S_{SG} = \frac{\pi}{4} D_m^2 = 92400\text{mm}^2,$$

The remaining co-section of free path S_f is:

$$S_f = S_{SG} - S_b = 16700\text{mm}^2.$$

Finally, the hydraulic diameter D_h of the central part is readily available as

$$D_h = 4(S_f - \frac{\pi}{4} D_p^2) / (\frac{\pi}{4} D_p) = 16.32\text{mm}$$

To localize the internal of the hexagon, we use a Cartesian system of coordinate (x,y) centered on the hexagon and with 2 opposite vertices on the x-axis, one of them with coordinate $(R,0)$, with $R>0$. By symmetry, we see that only the absolute value of the coordinates needs to be checked. Only two cases remain, whether the point is above or below 60 degrees. In each case, we check which size we are of the border. That is, In the first case, we check if $|y| < \sqrt{3}/2 R$ and in the second case if $|y|/\sqrt{3} + |x| < R$.

The characteristic function of the hexagon is defined by the easily implementable function given below.

If $(|y| > \sqrt{3}|x| \text{ and } |y| < \sqrt{3}/2 R)$ or $(|y| < \sqrt{3}|x| \text{ and if } |y|/\sqrt{3} + |x| < R)$ then 1 otherwise 0.

1.12.2 Hydraulic resistance

The hydraulic resistance for transversal tube bundles with triangular arrangement (which is the case here) is based on charts of the Euler number Eu , on the number of row per meter N_r :

$$N_r = 2 / (\sqrt{3} P) = 37.2$$

and on a mean velocity u taken at the section of minimum passage.

The expected pressure drop is given by in a distributed way by:

$$\Delta p = 0.5 N_r Eu \rho |u| u.$$

The velocity u used in this equation can be related to the superficial velocity v readily available in the numerical software by:

$$v = (1 - D_p/P) u$$

and

$$\Delta p = 0.5 P^2 / (P - D_p)^2 N_r Eu \rho |v| v.$$

This pressure drop can be implemented by means of an inertial hydraulic resistance coefficient C_2 :

$$C_2 = 0.5 P^2 / (P - D_p)^2 N_r Eu \rho.$$

However, in our specific case, the transversal (horizontal) hydraulic resistance is much higher than the vertical one while the previous form is based on an hypothesis of homogeneous resistance. As a consequence, it is probably more sound to have the quadratic behavior restricted to the horizontal component of the velocity v_h . It is therefore more practical to implement the transversal hydraulic resistance by means of a diagonal tensor with an horizontal linear coefficient C_1 :

$$C_1 = 0.5 P^2 / (P - D_p)^2 N_r Eu \rho |v_h|.$$

In the range of Reynolds number of interest, the Euler number is about 0.35. Thus, we take:

$$C_1 = 200 \rho |v_h|.$$

1.12.3 Bottom grid

Besides the holes to host the pipe bundle, the bottom grid is drilled with 204 circular holes (diameter $d_h=14\text{mm}$) distributed on a regular triangular-based pattern.

As for the SG bulk, the mid-scale homogeneity of the pattern cannot be fully preserved up to the border. We intend to split the porous baffle interface representing the grid in two distinct areas in correspondence with

the previous two bulk volumes and with different hydraulic resistance, inferred from two different mean porosities. Looking at the hole pattern away from the border, we can see that the surface of 2 holes is in correspondence to the area of influence of one pipe. As there are 91 pipes, we assign $N_1=2 \times 91=182$ holes to the central hexagonal area and $N_2=204-182=22$ holes to the border area.

The porosity β_1 of the central part of the grid is:

$$\beta_1 = 2 \frac{\pi}{4} d_h^2 / S_p = 0.370$$

while the porosity β_2 of the outer part is:

$$\beta_2 = N_2 \frac{\pi}{4} d_h^2 / S_f = 0.203.$$

There is a large uncertainty to derive a friction loss factor ϵ in our configuration. As a crude approximation we use a classical formula for sharp-edge orifice:

$$\epsilon = 2.7 (1 - \beta)(1 - \beta^2) / \beta^2$$

such that

$$\epsilon_1 = 10.7$$

$$\epsilon_2 = 50.1.$$

The coefficients effectively implemented in STARCCM+ are $\epsilon_1/2$ and $\epsilon_2/2$.

If instead of the theoretical surfaces, we consider their numerical counterparts which suffer from discretization errors, as only the cells centroid is checked, we come up with slightly different coefficients, as illustrated in Figure 48.

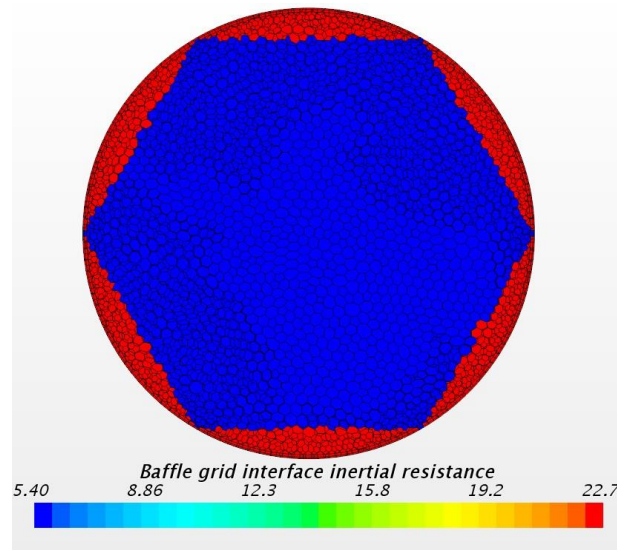


Figure 48: numerical implementation of a differentiated HX bottom grid inertial resistance coefficient.

21 General conclusion

The CIRCE experimental facility in ICE configuration has been numerically reproduced by means of CFD. From the discrepancies initially found between the experimental and numerical results an intense effort of analyze has been performed, some defects of the numerical models have been corrected and the discrepancies have been reduced. The thermal balance has shown to be very sensitive to apparently second order features: (i) the heat losses by Joule effect in the dead volume, (ii) the effective insulation of the vessel, (iii) the radiation heat losses in the gas gaps and at the free surface and (iv) the HX bundle hexagonal pattern in a circular envelop. For the transient simulations, the hydraulic resistance of the system has shown experimentally to be much lower than the one coming from over-conservative engineering correlations. Once taken into account in the CFD model, the transient simulation gives much better results. The gas lift system is also problematic has it induces a quite pulsated flow, even time scales of tens of minutes. Combined with a slow drift of the heat power and a large inertial time scale, CIRCE could never be put in a sufficiently steady-state configuration and comparison with numerical results remains limited.

In the end, the numerical modelling has allowed to better understand the experimental behavior of CIRCE and the complexity and limits of its CFD representation.

22 References

- [1] <http://sesame-h2020.eu/>
- [2] Tarantino, M., Scaddozzo, G. Test specifications of the Integral Circulation Experiments. Report ENEA ET-F-S-001, Deliverable D.4.15, DM4 DEMETRA, IP-EUROTRANS, 2006.
- [3] Tarantino, M. CIRCE Experimental Report. THINS deliverable D2.1.06. July 2013
- [4] Bandini, G., Di Piazza, I., Gaggini, P., Del Nevo., A., and Tarantino, M. CIRCE experimental set-up design and test matrix definition. ENEA UTIS-TIC Technical Report, IT-F-S-001. February 2011.
- [5] Tarantino, M., Martelli., D., Barone., G., Di Piazza, I., and Forgione, N. (2015). Mixed convection and stratification phenomena in a heavy liquid metal pool. Nuclear Engineering and Design, 286. 261-277.
- [6] <http://www.ansys.com/Products/Fluids/ANSYS-Fluent>
- [7] Zwijssen, K. Pool-Thermal Hydraulics Model of CIRCE-ICE: NRG Contribution to SESAME deliverable D3.2, ref: 23774/17.143405 RI/KZ/lr. Internal report
- [8] Todreas, N.E., and Kazimi, M.S., (1993). Nuclear System I, Thermal Hydraulic Fundamentals. Taylor & Francis.
- [9] Tarantino, M. et al. (2011). Integral Circulation Experiment: Thermal-hydraulic simulator of a heavy liquid metal reactor. Journal of Nuclear Materials, 415. 433-444
- [10] <https://www.sharcnet.ca/Software/Gambit/index.htm>
- [11] Bricteux, L., Duponcheel, M., Winckelmans, G., Tiselj, I., and Bartosiewicz, Y. (2012). Direct and large eddy simulation of turbulent heat transfer at very low Prandtl number: Application to lead-bismuth flows. Nuclear Engineering and Design, 246. 91-97.
- [12] Handbook on Lead-bismuth Eutectic Alloy and Lead Properties, Materials Compatibility, Thermal-hydraulics and Technologies, 2015 Edition, NEA.
- [13] Fokkens, J.H., Material Database for HFR Irradiation Experiments. Internal report.
- [14] http://www.engineeringtoolbox.com/air-properties-d_156.html